

**Final Technical Status Report**  
**Advanced Communication for Wireless Sensor Networks**  
**Contract No.: W911NF-10-2-0109**  
**Reporting Period: 29 Sept '10 – 20 June '15**

**Submitted to:**  
**Mitchell Wathen**  
**Cooperative Agreement Manager (CAM)**  
**Army Research Lab**  
**ATTN: RDRL-SEE-E**  
**Adelphi, MD**  
**Phone: 301-394-3802**  
**Email: mitchell.wathen@us.army.mil**

**Submitted by:**  
**Dan Carder**  
**Recipient Program Manager (RPM)**  
**West Virginia University**  
**Morgantown WV 26506**  
**E-mail: Daniel.carder@mail.wvu.edu**

**Professor Brian Woerner**  
**Technical-PI**  
**Lane Department of Computer Science and Electrical Engineering**  
**College of Engineering and Mineral Resources**  
**West Virginia University**  
**PO Box 6109, Morgantown, WV 26506-6109**  
**Email: Brian.Woerner@mail.wvu.edu**

**and**

**Faculty Participants:**  
**Daryl Reynolds, Natalia Schmid, Vinod Kulathumani, Xin Li, Matthew Valenti, Edward**  
**Sabolsky, David Graham, Jignesh Solanki, and Jay Wilhelm**

**Submitted: 22 August 2016**

**Distribution Statement A. Approved for public release; distribution is unlimited.**

## Table of Contents

1	Introduction.....	7
2	Task #1: Design, test, and demonstrate cooperative and multi-antenna communications systems.....	8
2.1	Subtask #1.1 Rapid Prototyping of MIMO Systems.....	8
2.1.1	Initial Steps and Setup .....	8
2.1.2	Installation of Simulink Drivers .....	9
2.1.3	Signal Processing Strategy for Increased Efficiency .....	9
2.1.4	Dataset .....	10
2.1.5	Video Compression .....	11
2.1.6	Initial Proposed Algorithm.....	11
2.1.7	Preliminary Results.....	12
2.2	Subtask #1.2 Cooperative Communication Systems .....	14
2.2.1	Image/Video Processing in Software Radio for Increased Range and/or Improved Energy Efficiency:.....	14
3	Task #2: Design, test, and demonstrate low-power analog and compressive sensing subsystems.....	16
3.1	Subtask 2.1: Nano-Derived Microsensors for Remote Threat Detection.....	16
3.1.1	Nano-Derived Micro-Magnetometer .....	16
3.1.2	Fabrication of Sensors .....	16
3.1.3	Characterization of Magnetostrictive Plates .....	17
3.1.4	Useful Life Characterization of the Magnetic Sensor .....	18
3.1.5	Pb(Zr,Ti)O <sub>3</sub> (PZT) Sol-gel Optimization .....	19
3.1.6	Additional 0-3 Composite Steps.....	20
3.1.7	Preparation of SiO <sub>2</sub> Cantilever Process .....	20
3.1.8	PZT Thin Film Fabrication and Optimization .....	20
3.1.9	Ferroelectric Characterization .....	22
3.1.10	Delamination.....	22
3.1.11	Solvothermal Synthesis of CFO Nano-particles .....	23
3.1.12	Optimization of CFO Nano-particle Dispersion in PZT Sol-gel .....	24
3.1.13	Micro-Chemical Sensor Array .....	27
3.1.14	Multi-step Hydrothermal-Assisted Procedure.....	28
3.1.15	Hydrogen Detection Micro-chemical Sensor .....	29
3.1.16	Fabrication of Micro-chemical Sensors With CuO .....	31
3.1.17	Re-creation of Hydrothermal nano-CuO Sensors .....	32

3.2 Subtask 2.2: Ultra-Low Power Analog Event Detection .....	32
3.2.1 Development of Vehicle Classification System.....	34
3.2.2 Development of Motion Detection Systems .....	34
3.2.3 Reverse Tunneling.....	35
3.2.4 Development of Analog Signal Processor.....	36
3.3 Subtask 2.3: Compressive Sampling and Low-power Collective Sensing.....	39
3.3.1 Error Resilient Image Coding.....	40
3.3.2 Open-source Implementation of SPIHT Image Coding.....	41
3.3.3 Integrate Image Codec at the System Level.....	41
3.3.4 Error Concealment for Multiple-description Coding.....	42
3.3.5 Low-rank Approximation for Simultaneous Sparse coding.....	42
3.3.6 Local Self-examples for Image Resizing and Super-resolution.....	42
3.3.7 Network-centric SPIHT Image Coding.....	42
3.3.8 Joint Source-channel-network Image Coding.....	43
3.3.9 Image Compression for Pattern Recognition.....	43
3.3.10 Low-rank Approximation for Computational Imaging.....	43
3.3.11 Low-rank Methods for Image Restoration. ....	44
3.3.12 Source Coding for Pattern Recognition.....	44
4 Task #3: Design, test, and demonstrate real-time fault-tolerant protocols for data aggregation, inference, location tracking, and connectivity maintenance in a mobile heterogeneous sensor network.....	45
4.1 Subtask 3.1: Distributed Coding and Data Exchange in Heterogeneous Sensor Networks .....	45
4.1.1 Unknown Object Location and the Strength of Physical Field .....	45
4.1.2 Distributed Coding and Estimation .....	46
4.1.3 Facial Encoding and Matching Methods .....	47
4.1.4 Multivariate Adaptive Regression Spline Approach .....	48
4.1.5 Fields Generated by Chemical Substances .....	48
4.1.6 Stochastic Reduction Algorithm.....	48
4.1.7 Maximum Likelihood Solution.....	49
4.2 Subtask 3.2 Middleware services for tracking and recognition applications using wireless sensor networks .....	50
4.2.1 Collaborative Multi-view Face Acquisition.....	50
4.2.2 Co-design Framework for Distributed Tracking Using Sensor Networks .....	51
4.2.3 The Pursuit Application.....	51

4.2.4	Exploitation of Distance Sensitivity.....	52
4.2.5	Exploiting Distance-sensitivity for Spatially Distributed Control Systems.....	52
4.2.6	VCAST Traffic Information Services .....	53
4.2.7	Simultaneous Coverage and Tracking: .....	54
4.2.8	Face Recognition .....	54
4.2.9	Control Serializability .....	55
4.2.10	Fusion Techniques for Networked Biometric Systems .....	55
4.2.11	Demonstration of Real-time Face Recognition at DHS Center of Excellence Meeting	56
4.2.12	EzTrack: Indoor Positioning .....	57
4.3	Subtask 3.3 Decentralized Control Algorithm for Self-Healing/Self Forming Network of Mobile Agents .....	57
4.3.1	Distributed Model Predictive Control.....	58
4.3.2	Autonomous Robots .....	61
4.3.3	Decentralized Model Prediction Control .....	61
4.3.4	Summation of the Functioning of MPC on Any Plant/System .....	63
4.3.5	Extended Kalman Filtering SLAM using MPC with Dynamic Features .....	63
4.3.6	Kalman Filter Derivation .....	64
4.3.7	Research Issues on Mobile Wireless Sensor Networks.....	65
4.3.8	Data Replication Issue.....	66
4.3.9	Model Predictive Control of a SISO .....	66
4.3.10	Multi-rate Fast Output Feedback Sampling Controller.....	67
5	Task 4: Design and demonstrate massively parallel simulation of large-scale sensor networks.....	69
5.1	Ad-hoc Network .....	69
5.1.1	Guard Zones .....	70
5.1.2	The Analytical Approach.....	71
5.1.3	Guard Zones in Sensor Networks .....	72
5.1.4	CSMA Guard Zone .....	73
5.1.5	Improvement of Cyberinfrastructure .....	74
6	Conclusion.....	75
7	References.....	76

## List of Figures

Figure 1. GRC representation of the GMSK transceiver. ....	8
Figure 2. Spectrum of received GMSK signal and the corresponding decoded video signal. ....	9
Figure 3. Camera Rig. ....	10
Figure 4. PIE- Camera 1. ....	10
Figure 5. The chain of command for the initially proposed algorithm. ....	11
Figure 6. Data rate for the first sample video using the proposed method (in total 246KB). ....	12
Figure 7. Data rate for the first sample video using H.264 video compression (Quality=1,4.0MB). ....	12
Figure 8. Data rate for the first sample video using H.264 video compression (Quality=25, 11.9M). ....	13
Figure 9. BER plot comparing the performance of the (1,1) and (1,2) antenna configurations. ....	13
Figure 10. Frame selection. ....	14
Figure 11. Tracking motion with digital zoom functionality. ....	15
Figure 12. Magnetometer accomplishments; a) SEM picture of a PZT plate, b) SEM picture of a spinel plate with his XRD and bulk density analysis, c) Macroscopic picture of booth plates and d) SEM and XRD analysis of spinel nano-particles. ....	17
Figure 13. a) Magnetostrictive properties ( $\alpha_{11}$ ) of the spinel plates and b) Piezoelectric loops (d33) of the PZT plates. ....	17
Figure 14. Left, voltage generated though the thickness of the sensor as a response of an applied magnetic field. Right: Polarization generated in the ME sensor due to application of a magnetic field. ....	18
Figure 15. Polarization as a measurement of cycle numbers. ....	19
Figure 16. XRD characterization of PZT thin films with: left, different Hydrolysis rates and right, different Pyrolysis temperatures. ....	19
Figure 17. SEM picture of Si/SiO <sub>2</sub> /Ti/Pt/PZT thin film (left) and XRD characterization of PZT thin films annealed at different temperatures for 60sec (right). ....	21
Figure 18. CFO particle distribution for different PEI concentrations. ....	22
Figure 19. Ferroelectric characterization of a PZT thin film deposited over Si/SiO <sub>2</sub> /TiO <sub>x</sub> /Pt wafer and annealed at 700°C for 60sec. ....	22
Figure 20. SEM picture of Si/SiO <sub>2</sub> /Ti/Pt thin film showing delamination in the Ti thin film. ....	23
Figure 21. Left, TEM image and right, XRD pattern of CFO nanoparticles. ....	23
Figure 22. XRD patterns of PZT thin films with and without thermal oxidation. ....	24
Figure 23. Left, pictures of PZT sol with CFO nano-particles after; right, 2 days, middle 10 days, left 19 days. Right, particle size average after different periods of time. ....	25
Figure 24. Left, pictures of PZT sol; left without shaking, right with shaking. Right, pictures of PZT; left without dispersants, middle with dimethylformamide and right with diethylenetriamide. ....	25
Figure 25. Modified sol gel thin film deposition. ....	26
Figure 26. SEM characterization of; left PZT thin film and right PZT with 2% CFO loading thin film. ....	26
Figure 27. XRD characterization of; left PZT thin films sintered at 600, 650 and 700 °C and right PZT films with 2% CFO loading sintered at 500, 600 and 700 °C. ....	27

Figure 28. Ferroelectric characterization of PZT films; in red without CFO and in black with CFO nano-particles.....	27
Figure 29. IDEs geometry.....	28
Figure 30. AU IDEs.....	28
Figure 31. Test results for a hydrogen chemical sensor at 340°C.....	29
Figure 32. Picture of a singular micro-sensor with CuO nanomaterial absorbents across the IDE pattern.....	30
Figure 33. Picture of a four element array of nano-CuO micro-sensors (with one sensor connected through contact via).....	31
Figure 34. Sensing performance of a singular micro-sensor exposed to different low levels of H <sub>2</sub> for times ranging from 10 min to 1 sec.....	31
Figure 35. Left, block diagram of our analog event detector, showing how it interfaces with sensing nodes. Right, demonstration of the event detector IC.....	33
Figure 36. Vehicle Classification results and Chip Specifications.....	34
Figure 37. Increased linear range of amplifiers (left) and reduction in the trans-conductance of the amplifier (right). .....	35
Figure 38. Left: block diagram of our analog event detector, showing how it interfaces with sensing nodes. Right: comparison of the power consumption of our ASP approach versus all digital vehicle classification systems.....	36
Figure 39. (a-b) The system is capable of capturing a wide range of amplitudes and frequencies. For these plots, the input is shown in grey, detected max/mins are black dots, and the reconstructed wave is a black dashed line. (c) The speech clip used as input to the system is shown in grey with detected max/mins in black dots. (d) The speech clip approximation from using the modified Bezier formula with the sampled max/mins.....	37
Figure 40. The integrated circuit.....	38
Figure 41. The PCB .....	38
Figure 42. Results of the integrated circuit.....	38
Figure 43. Illustration of multiple-description coding (MDC) for two channels and three receivers (Decoder 0 – central receiver; Decoder 1 or 2 - side receiver). .....	39
Figure 44. Top: decoded image at the side receiver (PSNR1 = 26.42dB, PSNR2 =26.24dB) by SPIHT at the bit rate of 0.1bpp. Bottom: decoded image at the central receiver by different algorithms: left - ad-hoc averaging of two decoded versions (PSNR=27.30dB); right – MAP decoding from two received bit streams (PSNR=28.36dB).....	40
Figure 45. Rate-Distortion performance comparison between conventional (old) and error-resilient (new) SPIHT algorithms on lena image.....	40
Figure 46. Error-concealment performance comparison between morphological component analysis (MCA)-based (left, PSNR=22.17dB) and ours (right, PSNR=24.30dB) on lena512 image [Li2010].....	41
Figure 48. Estimated magnitude (left), x-coordinate of the location parameter (middle) and y-coordinate of the location parameter (right) displayed as functions of the number of iterations, k.....	47
Figure 48.Distribution of initial values as a function of the ring radius the box plot of Square Error as a function of the radius for the case of 20 sensors and SNRo=SNRc=15 dB. ....	50
Figure 49. Epipolar camera comparison. Line AB indicates epipolar line in the other cameras.....	51
Figure 50. Exploiting distance-sensitivity for pursuer-evader tracking.....	52

Figure 51. The figure shows the impact of the communication range on information staleness at different inter-vehicular distances when VCAST is used to disseminate traffic information. The source broadcast rate is 5Hz.....	53
Figure 52. Impact of the locality of reconfiguration on the normalized coverage resolution of a monitored area.....	54
Figure 53. A sample image collected from Trident systems test are. The figure shows the face image and human body silhouette detected by our system on a portable Linux platform.....	55
Figure 54. Tracking error in EzTrack - anchor nodes at 14 feet separation.....	57
Figure 55. Distributed multi agent Model Predictive Control Structure.....	58
Figure 56. Protection zone of the robots and their position.....	59
Figure 57. Left, evolution of the robots position in xy plane over a period of time with collision avoidance. Right, collision avoidance between two mobile robots; robot 1 (blue) and robot 2 (red).....	60
Figure 58. Uncertainty condition in one time stamp: Left, evolution of the robots position in xy plane over a period of time with collision avoidance. Right, collision avoidance between two mobile robots; robot 1 (blue) and robot 2 (red).....	60
Figure 59. Uncertainty condition in multiple time stamp: a) Left, evolution of the robots position in xy plane over a peridod of time with collision avoidance. Right, collision avoidance between two mobile robots; robot 1 (blue) and robot 2 (red).....	61
Figure 60. Demonstration of Faster and Slower Movement; robot 1 (blue) and robot 2 (red).....	62
Figure 61. SLAM with EKF and without MPC (left) and b) SLAM with EKF and MPC (right) .....	64
Figure 62. Graphical model of EKF SLAM algorithm.....	65
Figure 63. Simple SISO system model with plant and MPC control.....	66
Figure 64. Illustration of MPC.....	67
Figure 65. Servo responses.....	67
Figure 66. Outage probability $\mathbb{P}$ as a function of SNR for SINR thresholds $\mathbb{B} = \{-10, 0, 10\}$ dB. Analytical curves are solid, while dots represent simulated values. The network geometry is shown in the inset .....	69
Figure 67. An example ad hoc network.....	71
Figure 68. Influence of guard zone radius $r_{min}$ on network performance.....	72
Figure 69. Example of network realization.....	73

## 1 Introduction

Advanced Communication for Wireless Sensor Networks was proposed to focus on the development of innovative technologies for networked sensing, information processing, and control. This focus was in support of the Army Research Laboratory's (ARL) research and development program in advanced communications for mobile networks. More specifically the primary objective was to develop and demonstrate key sensor-network capabilities, lower-power electronic technology, and flexible, highly reliable communication systems to support small unit military operations. To accomplish this objective, the project was divided in to tasks, which included:

- Task 1: Design, test and demonstrate cooperative and multi-antenna communications systems.
- Task 2: Design, test, and demonstrate low-power analog and compressive sensing subsystems.
- Task 3: Design, test and demonstrate real-time fault-tolerant protocols for data aggregation, inference, location tracking, and connectivity maintenance in a mobile heterogeneous sensor network.
- Task 4: Design and demonstrate massively parralell simulation of elarge-escale sensor networks.

The accomplishments for each of these tasks are documented in the subsequent sections. Furthermore, each task has been subdivided in to subtasks and the activities performed to satisfy these subtasks are also presented.

## 2 Task #1: Design, test, and demonstrate cooperative and multi-antenna communications systems.

### 2.1 Subtask #1.1 Rapid Prototyping of MIMO Systems

#### 2.1.1 Initial Steps and Setup

After acquiring and assembling the USRP-based software radio testbed, the team began developing a series of successively more advanced demonstrations. The most basic demonstration was FM reception. The next demonstration was voice transmission and reception (using analog single-sideband modulation). Next, basic digital transmission and reception of text and video was demonstrated (using GMSK modulation). Finally, a GMSK transceiver was implemented, which was capable of both transmitting and receiving in the same radio. The system was implemented using the Gnu Radio Companion (GRC), which was a graphical layout tool that enabled rapid prototyping. A screenshot of the GMSK transceiver, as represented in GRC, is shown in Figure 1.

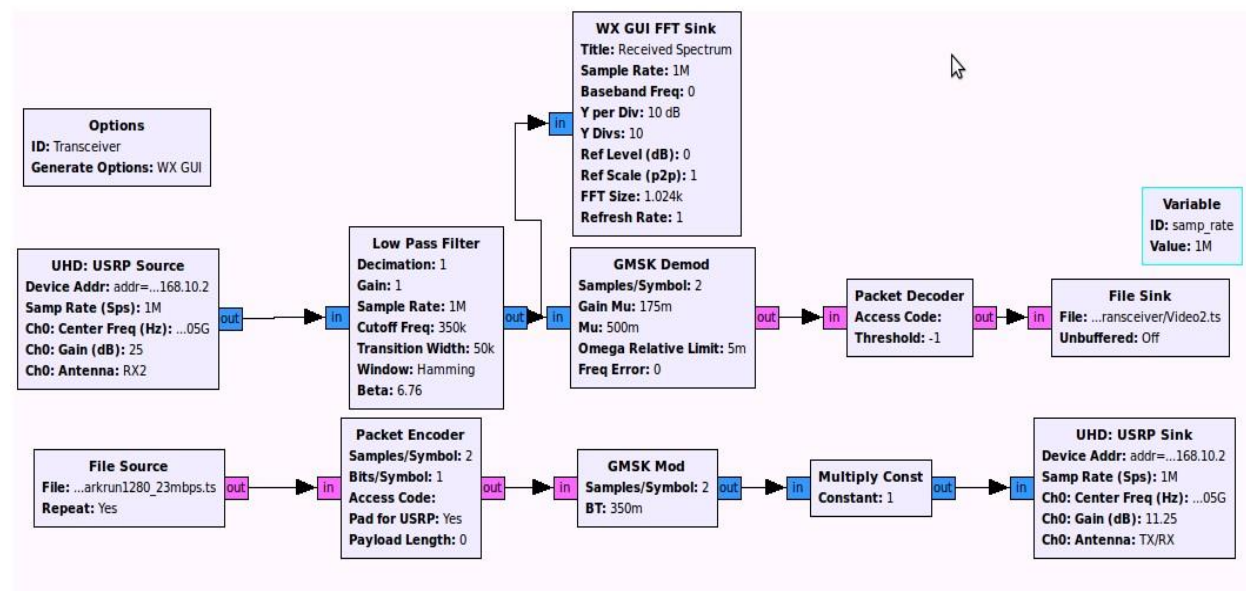


Figure 1. GRC representation of the GMSK transceiver.

The USRP hardware was represented in GRC by either a *USRP Source* (the received chain) or a *USRP Sink* (the transmitter chain). Figure 2 shows the received signal spectrum and decoded video signal.

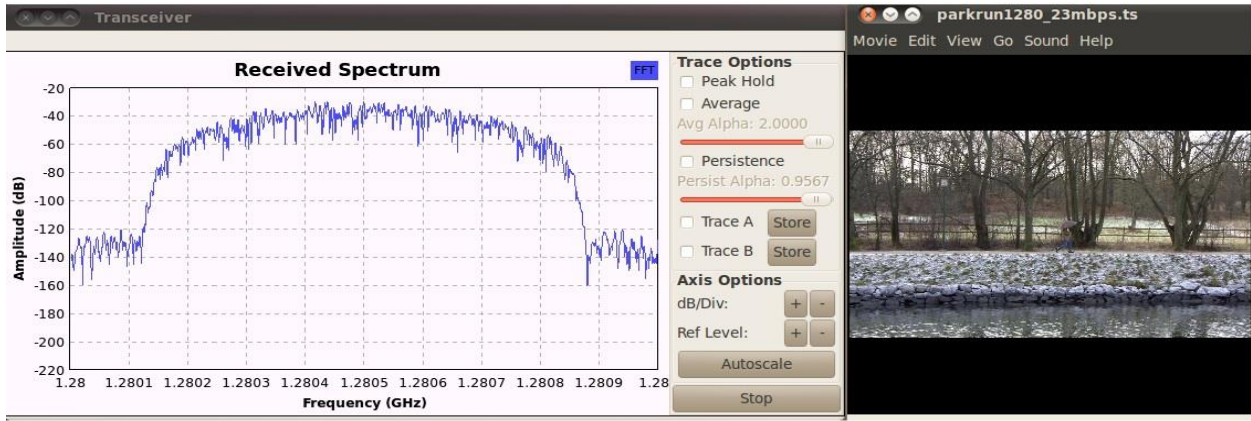


Figure 2. Spectrum of received GMSK signal and the corresponding decoded video signal.

After procuring appropriate software-defined-radio (SDR) hardware, data was successfully transmitted using one transmit antenna and two receive antennas. For the test application, a real-time audio/video chat function was developed (similar to Skype) for the SDR platform.

### 2.1.2 Installation of Simulink Drivers

Simulink drivers were installed and QPSK modulation was tested using Simulink/USRP. With the help of Mathworks, synchronization and frequency/phase compensation issues were resolved for a 1 x 1-antenna configuration and audio/video data were transmitted successfully.

Video and image processing with Simulink/USRP platform was performed. Two options seemed to be the most feasible during this phase, these options were: 1) *adaptive image/channel coding based on image segment priorities* and 2) *the embedding of sensor signal processing results as watermarks in images/video*. Communications using the 1 X 2-antenna configuration and 1 X 2-antenna configurations were optimized for ARL visitors using the GNU/USRP platform.

Reallocation of some of the SDR testbed efforts from the GNU software platform to Matlab/Simulink was performed to take advantage of professional support and built-in functionality. Although multi-antenna communication was not supported by Mathworks, the team able achieve communications with one transmit antenna and two receive antennas after resolving some spatial synchronization issues.

### 2.1.3 Signal Processing Strategy for Increased Efficiency

A general signal processing strategy was developed for increasing energy efficiency in surveillance sensor networks. This included; 1) image/video segmentation, where motion was extracted from a video stream at the sensor node and, 2) priority encoding of the segmented video, where high priority parts of the video (containing motion) were source coded for high quality and channel coded for high reliability, and lower priority video segments (backgrounds) were allocated fewer bits for source and channel coding.

Further, an application was created that demonstrated convolutionally-coded communications between two USRP radios. The demo app allowed the users to select the length of the synchronization preamble and the length of the message, and displayed the resulting error rate.

#### 2.1.4 Dataset

The ChokePoint Dataset developed by NICTA was selected for the experiments, as images in it were very similar to real surveillance videos even though the dataset was collected in a controlled environment [1].



Figure 3. Camera Rig [1].

Figure 3 depicts the camera rig utilized for Chokepoint Dataset experiments. The rig was stabilized to an aluminum tripod for extra support.



Figure 4. PIE- Camera 1 [1].

Figure 4 depicts an individual being photographed by the camera Chokepoint camera rig. As this individual rounded the corner and entered the doorframe, his image was captured.

The famous Open CV Viola-Jones Face Detection algorithm was utilized in Matlab for the purpose of performance evaluation [2]. The code was downloaded from the Matlab exchange.

### 2.1.5 Video Compression

The most popular and advanced video compression method H.264 encoding (provided by MATLAB [3]) was used to compress the video data. Different settings were tested for the most balanced point between power consumption and performance.

### 2.1.6 Initial Proposed Algorithm

Historically, few applications need a “live” video feed. Low latency, however, always will be the key requirement for smart video sensor because of time sensitivity and the small buffer size. Not every frame is important, and not even everything in a single frame is important. When the team tried to remove the redundancy in the video data, the team actually defined what was important (or useful). Criteria were often different for different applications.

In the initially proposed algorithm, a face detector was used to detect the face and then a quality evaluation box was used to find the best “face” candidate for a certain person. Data rate was recorded and analyzed when the proposed algorithm was compared with pure video compression based algorithms. Figure 5 depicts the chain of command for this algorithm.

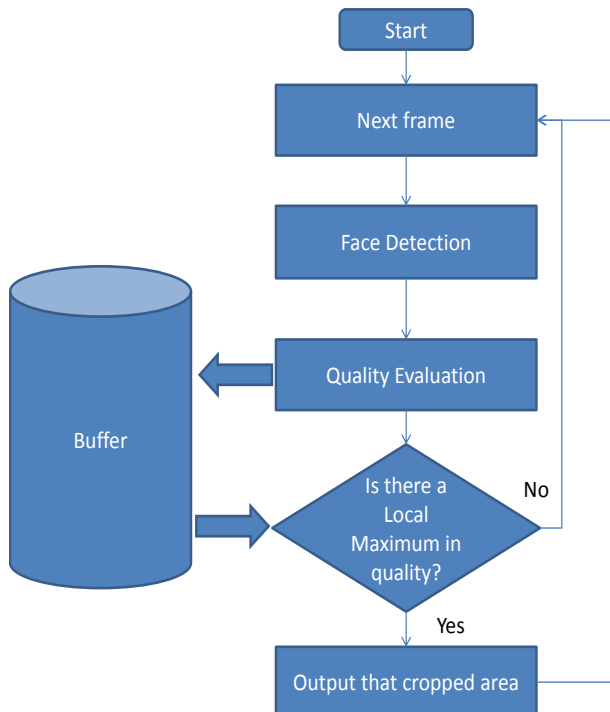


Figure 5. The chain of command for the initially proposed algorithm.

### 2.1.7 Preliminary Results

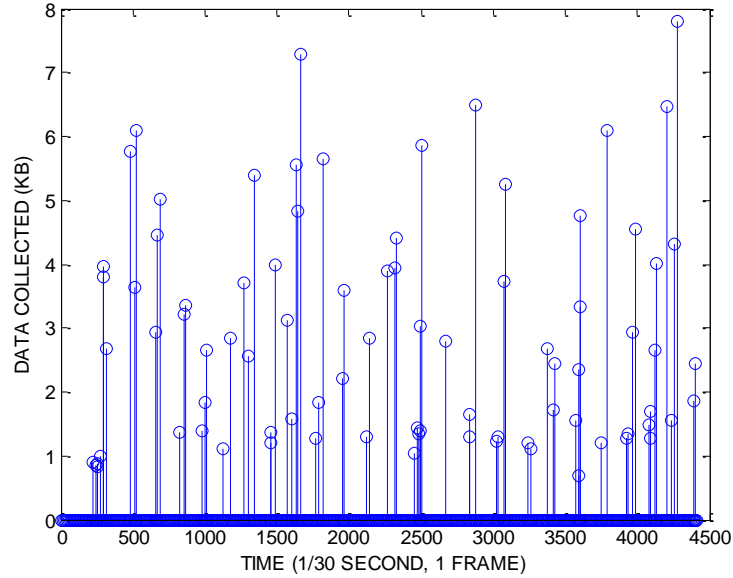


Figure 6. Data rate for the first sample video using the proposed method (in total 246KB).

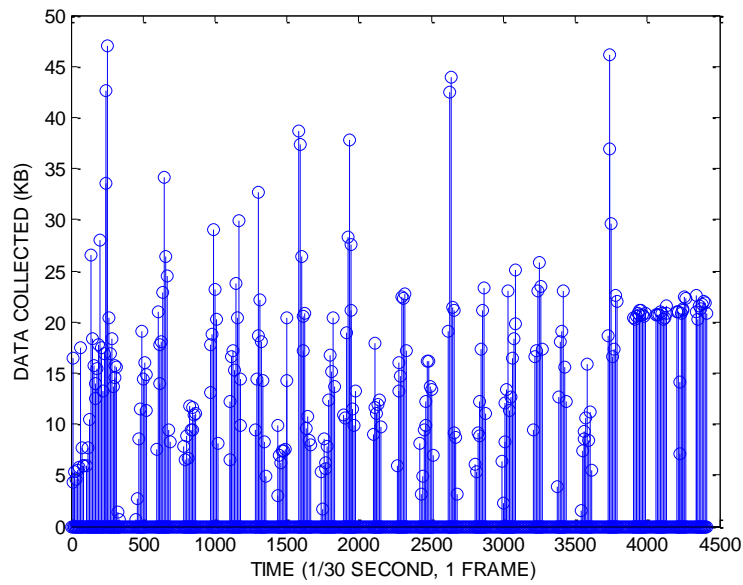


Figure 7. Data rate for the first sample video using H.264 video compression (Quality=1, 4.0MB).

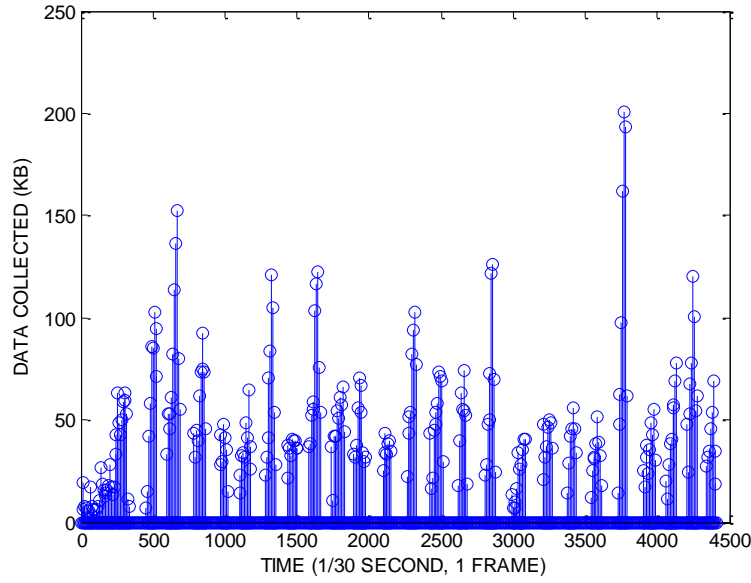


Figure 8. Data rate for the first sample video using H.264 video compression (Quality=25, 11.9M).

Figure 9 is a sample BER plot comparing the performance of the (1,1) and (1,2) antenna configurations using the SDR testbed. The array gain that was expected using two receive antennas is clearly visible, though there is a BER increase at large gain that was not expected.

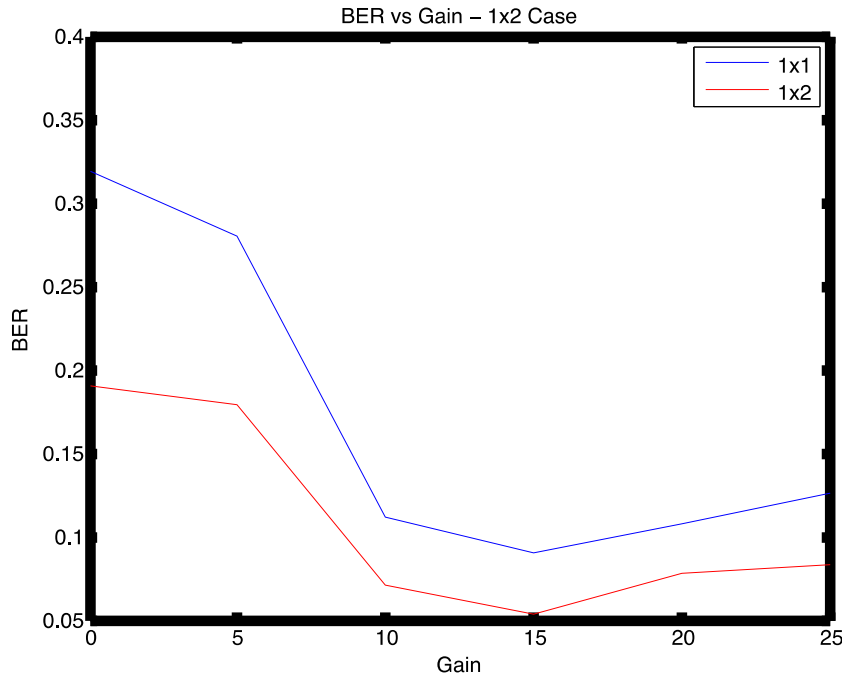


Figure 9. BER plot comparing the performance of the (1,1) and (1,2) antenna configurations.

Testing was completed of SIMO communications (with one transmit antenna and two receive antennas) using the software-defined-radio (SDR) testbed, and a conference paper was submitted on this topic to the IEEE Consumer Communications and Networking Conference (CCNC 2013).

Results were produced using MISO communications (using two transmit antennas and one receive antenna) with the Alamouti space-time block code.

## 2.2 Subtask #1.2 Cooperative Communication Systems

### 2.2.1 Image/Video Processing in Software Radio for Increased Range and/or Improved Energy Efficiency:

With respect to image/video processing for this project, the goal was to develop signal processing strategies that could be used to increase the single-hop transmission range of a wireless sensor network, increase energy efficiency (improve battery life), or both (each to a lesser extent). Ultimately, two such strategies were developed along with a roadmap for incorporating additional technologies.

For a video stream, there were several methods available to reduce the size of the final data package that would be delivered to the receiver, which, using appropriate power control, allowed the range of the network to be extended or provided an increase in its battery life. Based on the complexity level (from low to high), some of them were:

1. Lossless data compression, e.g., “zip” coding
2. Lossy data compression, e.g., MPEG, MJPEG
3. Sleep after a certain length of “quite” time and be waked up by other sensors when something happens
4. Frame selection and digital zoom based on the simple motion detection
5. Frame selection and digital zoom based on the complex event detection
6. High level feature extraction, such as coordinates within a video frame

While data processing also consumed some power, it was expected that this would be more than offset by improved energy efficiency. The team chose to implement some of these strategies using our GNU SDR testbed. In order to do so, several existing code blocks were modified and re-designed for the project:

1. *Image Source*: In this block, a color or a gray scale image was read into memory and passed to the next block, pixel by pixel. The original code could not handle large color images. This bug was fixed by carefully checking the buffer size.
2. *Frame Selection*: See Figure 10. This is a new signal-processing block created by the team. Similar to the image source block, instead of an image filename, a video device index was specified in this video source block. To save the power, only when there is clear motion detected in the scene will the sensor capture and

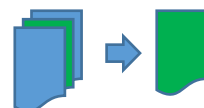


Figure 10. Frame selection.

transmit the video at full resolution and rate. Otherwise, the sensor operated at a very low frame rate, e.g., 0.2 FPS (frames per second). This was called video frame selection.

3. *Digital Zoom*: This was another new signal processing block created by the team. In many cases of interest, only a small portion of a video frame contained useful information. If nothing occurred in the scene, this block sends a down-sampled frame (1/4 of the original size). If there was clear motion in the scene, this block locates the motion and crops the image around the motion location, i.e., a digital zoom function. Figure 11 illustrates digital zoom.

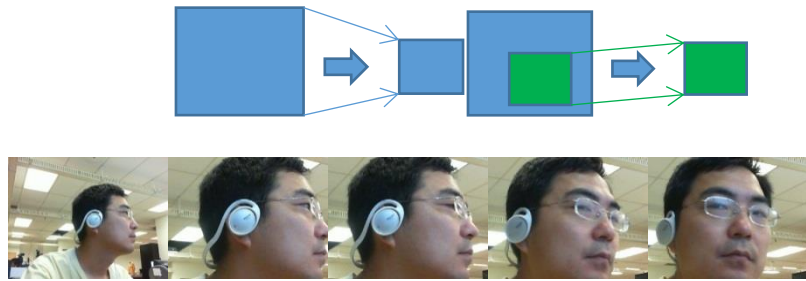


Figure 11. Tracking motion with digital zoom functionality.

As alluded to earlier, a general signal processing strategy was developed for increasing energy efficiency in surveillance sensor networks. This included; 1) image/video segmentation, where motion is extracted from a video stream at the sensor node, and 2) priority encoding of the segmented video, where high priority parts of the video (containing motion) were source coded for high quality and channel coded for high reliability, and lower priority video segments (backgrounds) were allocated fewer bits for source and channel coding.

### **3 Task #2: Design, test, and demonstrate low-power analog and compressive sensing subsystems.**

#### **3.1 Subtask 2.1: Nano-Derived Microsensors for Remote Threat Detection**

##### **3.1.1 Nano-Derived Micro-Magnetometer**

The fabrication of the first magnetometer was successful. This magnetometer was made of a PZT-spinel composite. PZT plates were successfully fabricated by a tape-casting process using commercially available PZT. These plates showed good bulk density (low internal porosity) and microstructure (see Figure 12a). In the case of the spinel plates the precursor powders were not commercially available; therefore, a coprecipitation synthesis was developed to fabricate powder with the proper composition, particle morphology and crystal structure. A calcination study was completed in order to obtain a powder with good surface area and crystallinity. The x-ray diffraction spectra of the material produced is displayed in Figure 12b. With the powders, preparation of the spinel plates was achieved. Different thermal processing treatments were investigated in order to obtain a high bulk density of the plates. The morphology of the plates and the bulk density for different calcinations temperatures can be seen in Figure 12b. Finally, a macroscopic view of both plates can be seen in Figure 12c.

##### **3.1.2 Fabrication of Sensors**

To fabricate the different micro scale sensors proposed, the desired ceramic materials needed to be fabricated by micro-scale techniques. In the case of the magnetoelectric laminate, the most appropriate technique was through alternate spin coatings of sol gel solutions of the two compositions. For the 0-3 composite, a particulate dispersion of magnetostrictive nanomaterials within the piezoelectric sol gel solution was required to produce the hybrid system. In the case of the PZT composition, a sol gel was successfully synthesized. This solution was spin coated showing good viscosity and homogeneity. The obtained thin films were characterized by XRD and the results showed the characteristic peaks of the PZT crystallography and the presence of non-desired secondary phases. Regarding the spinel thin film, a new sol gel process was developed. The obtained solutions presented non-desired particulates precipitation. To solve this problem, different precursors and solvents were purchased in order to suppress this precipitation. Regarding the spinel nano-particles, they were successfully fabricated by a hydrothermal process. The morphology of the obtained particles and the XRD characterization can be seen in Figure 12d.

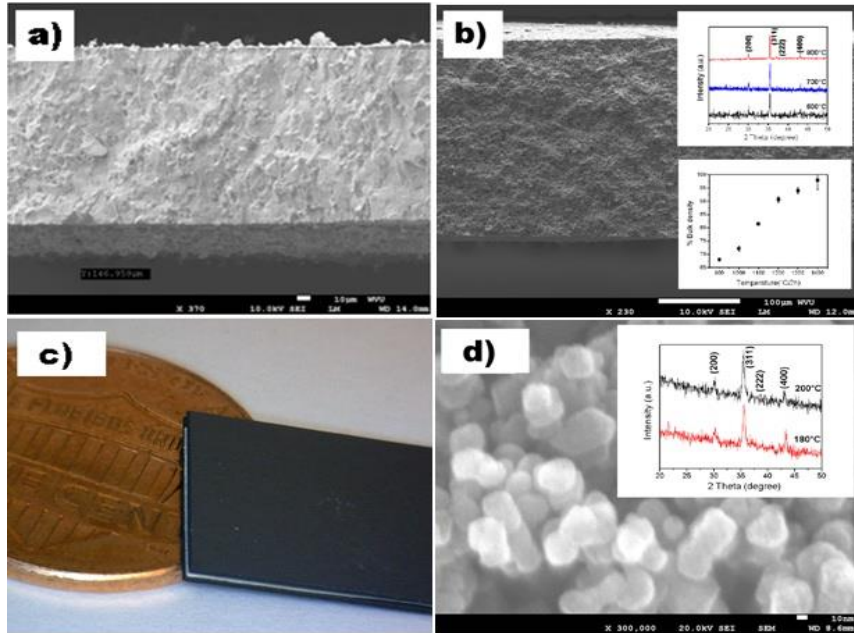


Figure 12. Magnetometer accomplishments; a) SEM picture of a PZT plate, b) SEM picture of a spinel plate with his XRD and bulk density analysis, c) Macroscopic picture of booth plates and d) SEM and XRD analysis of spinel nano-particles.

### 3.1.3 Characterization of Magnetostrictive Plates

First, the magnetostrictive plates were characterized using a vibrating sample magnetometer to produce a magnetostriction in the sample and the deformation was measured with a strain gage. A representative curve of the parallel magnetostriction can be seen in Figure 13(a). The characterized material shows a comparable behavior as the one reported by Sheikh et al [4]. Here, an increase in the magnetostriction with magnetic fields up to 0.4 kOe can be seen. This represents the saturation magnetic field of the material. For higher magnetic fields, the magnetostriction remained constant. In the case of the PZT, the piezoelectric properties were measured using a high voltage power supply to pole the sample and a linear variable differential transformer to measure the deformation. These measurements were made in the installations of TU Darmstadt, Germany. The obtained results are shown in Figure 13(b). A linear response of the piezoelectric response with the applied electric field is shown. The obtained results are comparable to the ones reported in literature for similar piezoelectric compositions.

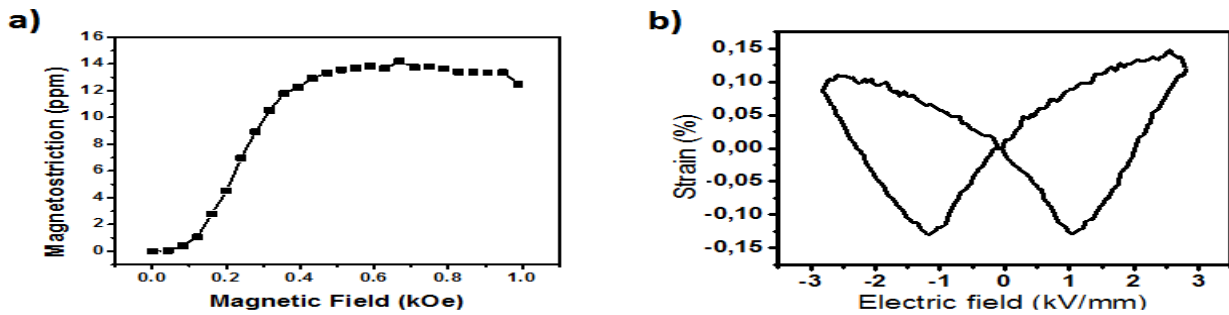


Figure 13. a) Magnetostrictive properties ( $\alpha_{11}$ ) of the spinel plates and b) Piezoelectric loops ( $d_{33}$ ) of the PZT plates.

The macro magnetoelectric sensors were fabricated by the addition of spinel and PZT plates in a laminate composite. To bond the plates, three different gluing conductive materials were

performed. The glues used were conductive paint, fired silver paint and conductive epoxy. The selected glue was conductive epoxy since the other presented additional problems. The magnetoelectric response of the sensors was characterized with two different circuits. First, the magnetoelectric response was measured by an open circuit and measuring the voltage with a high impedance voltmeter. The obtained results can be seen in the Figure 3. The voltage dropped due to leakage currents through the PZT plate. This was disadvantageous since the acquisition rate needed be higher, and this generated problems with calibration. An alternative circuit was to measure the current generated for the sensor and integrate it to obtain the polarization. The results obtained with this circuit can be seen in the Figure 14 (right). Here, the leakage currents were avoided since the PZT plate is short circuited. For both circuits, a high noise to signal ratio was detected. The noise mainly arose from the electrical network, because of its characteristic frequency of 50Hz. The noise filtering needed improvement in order to improve the sensitivity of the device.

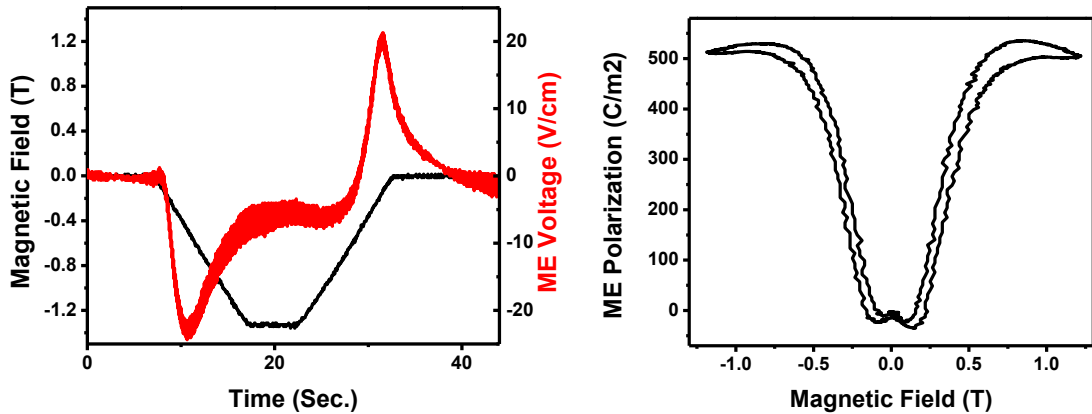


Figure 14. Left, voltage generated though the thickness of the sensor as a response of an applied magnetic field. Right: Polarization generated in the ME sensor due to application of a magnetic field.

### 3.1.4 Useful Life Characterization of the Magnetic Sensor

The useful life of the magnetic sensor was characterized through fatigue studies. This was made through the exposure of the sensor to an oscillating magnetic field with an intensity of 0.5T. The polarization was measured as a function of the cycle number. The obtained results can be seen in Figure 15. A drop of 17% in the polarization can be seen when the sensor is exposed to 100 cycles. After this drop, the polarization remained constant until 14000 cycles. This pointed to the necessity of calibration of the device after a use period if a high sensitivity was required. At the same time, the sensor remained stable for a long exposure to high cycling magnetic fields, which allowed the application in a long useful life sensor.

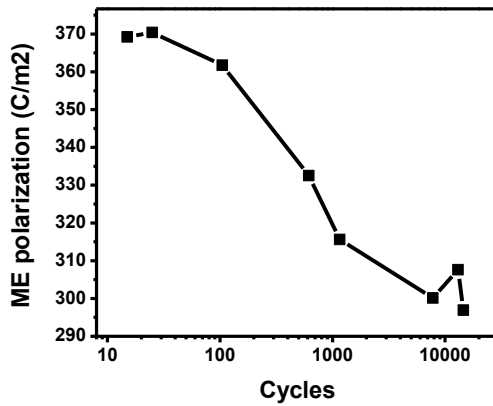


Figure 15. Polarization as a measurement of cycle numbers.

### 3.1.5 Pb(Zr,Ti)O<sub>3</sub> (PZT) Sol-gel Optimization

The Pb(Zr,Ti)O<sub>3</sub> (PZT) sol-gel process was optimized to decrease the crystallization temperature. This was needed to decrease the lead evaporation and crack formation. The main problem in the PZT crystallization was the formation of pyrochlore phase; this phase decreased the piezoelectric properties substantially. The first approach was to add small amounts of water to produce internal hydrolyzation of the sol-gel. This work observed that the pyrochlore phase increased with the addition of water (this can be seen in the Figure 16). A second approach was to modify the hydrolysis temperature; here, temperatures ranging from 300°C to 450°C were evaluated. The optimum temperature was 400°C. As can be seen in the x-ray diffraction (XRD) spectrum in Figure 16 (left), the influence of the pyrolysis temperature with the pyrochlore phase formation was observed through the decrease in the 100% peak for this phase at  $2\theta \approx 29.75^\circ$ . As expected, the amount of pyrochlore decreased substantially as the temperature of pyrolysis was increased. Finally, the time was modified for the crystallization temperature at 600°C. It was found that the optimum time for the pyrolysis was 120 sec with the large increase in the desired perovskite 100% peak at  $2\theta \approx 31.2^\circ$ . Unfortunately, a small portion of pyrochlore was generated, and the composition needed to be modified in order to completely eliminate this phase before work could continue on the composite.

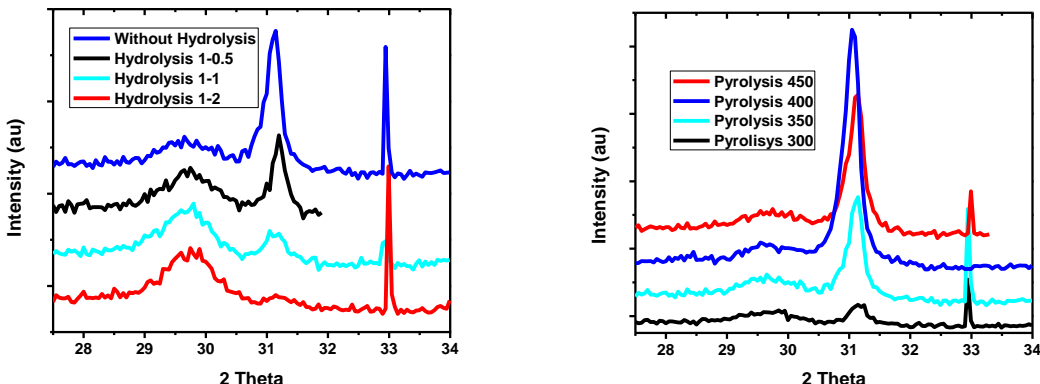


Figure 16. XRD characterization of PZT thin films with: left, different Hydrolysis rates and right, different Pyrolysis temperatures.

### 3.1.6 Additional 0-3 Composite Steps

Regarding the 0-3 composite,  $\text{CoFe}_2\text{O}_4$  (CFO) nano-particles were dispersed in 2-methoxyethanol. The nano-particles were synthesized using a hydrothermal process in an aqueous medium. Since the resulting nano-particles synthesized in the hydrothermal process were suspended in the aqueous solution, the nano-particle suspension could not be directly added to the PZT sol gel due the incompatibility of these two solvent systems. To replace the water from the suspension, a solvent exchange process was completed using 2-methoxyethanol. After three exchange reactions, the suspension was finally centrifuged and distilled. The obtained stable particles were added to the PZT sol-gel and spin coated. The spin coated film was characterized with XRD. In the XRD patterns, the PZT peaks could be seen, but there was presence of CFO peaks. This was due to the low concentration of CFO (10%) in the film. During processing of these films, it was found that the CFO nanoparticles began to agglomerate and fall out of suspension. Further work on the selection and control of the dispersants was needed to stabilize the particles.

The first ferroelectric characterization was successfully completed for a PZT thin film. In order to complete these measurements, the optimal PZT films discussed above were deposited over a conductive wafer. The conductive wafer consisted of a Si wafer with several thin films, such as 500nm  $\text{SiO}_2$ , 50nm of Ti and 300nm of Pt. Over the PZT thin films, electrodes were deposited and patterned in order to have a precise upper electric contact. Finally, the film was characterized with a Radiant thin film ferroelectric tester; the obtained results did not show the characteristic piezoelectric loops; this was initially thought to be due to the presence of the pyrochlore phase.

### 3.1.7 Preparation of $\text{SiO}_2$ Cantilever Process

The  $\text{SiO}_2$  cantilever process was established. A thermally grown  $\text{SiO}_2$  wafer was patterned by photolithography with the cantilever pattern. After this process, the  $\text{SiO}_2$  was dry etched with a mix of  $\text{O}_2$  and  $\text{CF}_4$  using the photoresist as a protective layer. Finally, the cantilever was released after a wet etching using tetramethylammonium hydroxide (TMAOH) solution in controlled conditions.

After seeing the first results, it was noticed that the ratio between width and length was too small. The consequence of this was that poor mechanical properties were obtained. New attempts to obtain  $\text{SiO}_2$  cantilevers were performed using smaller patterns with aspect ratios closer to unity, but problems with the release of the photoresist after the dry etching and issues with burned photoresist during the dry etch were encountered. The cantilever was released by a wet-etch using TMAOH in controlled conditions. The concentration of the etching solution was reduced, and this resulted in slower etching rates; but the reduced etchant strength permitted controlled release of the cantilevers with a low degree of structural degradation.

### 3.1.8 PZT Thin Film Fabrication and Optimization

During this period, the PZT thin film fabrication was optimized and a final crack free, perovskite crystal structure PZT thin film was obtained. In order to achieve this, the chemical composition of the precursors was carefully characterized with the loss-on-ignition (LOI) technique. The results of the LOI characterization showed a discrepancy of up to 20%

compared with the reported by the vendors. The films were deposited on Si/SiO<sub>2</sub>/Ti/Pt wafers obtained from a vendor. The results of this study can be seen in Figure 17. Figure 17(left) shows a SEM micrograph of a crack-free PZT thin film over the Si/SiO<sub>2</sub>/Ti/Pt layers. The thickness of the PZT thin film is ~300nm, and this was confirmed with ellipsometry (285nm). Regarding the crystal structure, the results of the optimized PZT thin film can be seen in Figure 17 (right). Here the crystal structure was characterized at different sintering temperatures for 60 sec. It can be seen that for temperatures higher than 650°C, a 100% perovskite phase was obtained; but for the 600°C thermal treatment, the non-desired pirochlore phase was present. With this study, the experimental conditions to obtain a crack free, perovskite phase PZT thin film were determined.

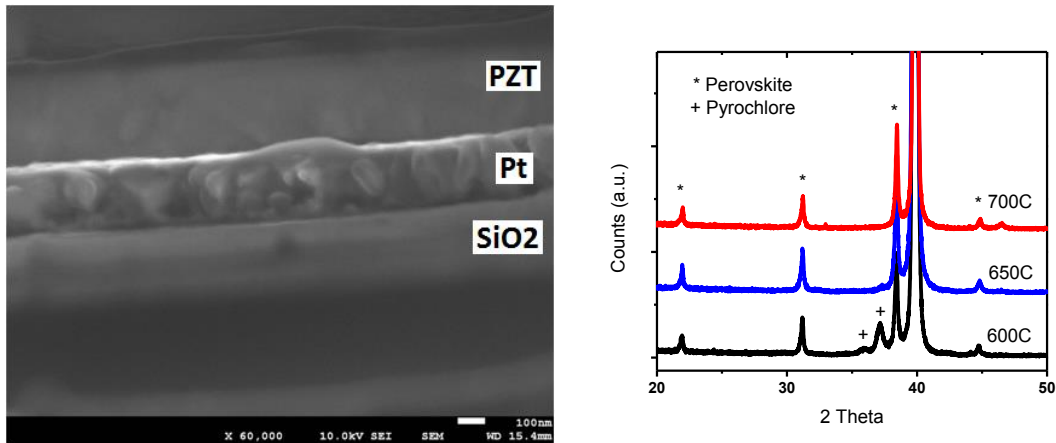


Figure 17. SEM picture of Si/SiO<sub>2</sub>/Ti/Pt/PZT thin film (left) and XRD characterization of PZT thin films annealed at different temperatures for 60sec (right).

For the fabrication of the ME sensors, a process to deposit controlled layers of SiO<sub>2</sub>/Ti/Pt onto the Si wafers was needed. Different approaches were completed to investigate the effect of various processing conditions and thicknesses on the final piezoelectric thin film. The first approach was to deposit Ti and Pt via sputtering onto a thermally oxidized Si/SiO<sub>2</sub> wafer. When the PZT thin film was deposited and annealed, the film suffered from various defect formations, such as delamination. This was due to several factors such as Si surface contaminates, in-plane strain related to Ti and Pt thickness, and strain relaxation processes during later thermal annealing processes. In order to resolve some of these issues, the following approaches were quickly evaluated: SiO<sub>2</sub> was grown on the Si surface by PECVD, intermediate annealing steps were implemented, analysis of cleaning process effects were monitored, and Ti and Pt thickness was modified.

Regarding the 0-3 composite, initial experiments showed a high level of nanoparticle agglomeration. Various methods to re-disperse the obtained particles in 2-methoxyethanol were implemented, such as a short investigation of the use of PEI dispersants. Improvements were achieved, but the resultant dispersion was not optimal. The dispersion study can be seen in Figure 18; the addition of PEI dispersant permitted further dispersion of the agglomerated system, yet the primary particle size of ~20 nm was never achieved.

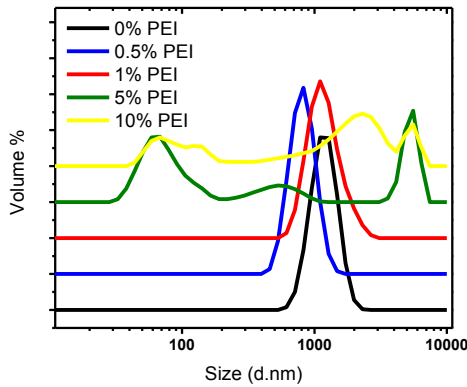


Figure 18. CFO particle distribution for different PEI concentrations.

### 3.1.9 Ferroelectric Characterization

In order to obtain a ME composite, a PZT thin film with good ferroelectric properties was needed. Because of this reason, the ferroelectric properties of the thin film were characterized and optimized. Several films were fabricated and Pt electrodes were deposited over them in order to have an upper contact. The process was optimized to achieve reproducibility and good ferroelectric properties. The results can be seen in figure 19. Here a good ferroelectric response without leakage currents, ferroelectric shape and remnant polarization. This process resulted in a reproducible fabrication of PZT thin films that was used to incorporate CFO nano-particles before the PZT was spin coated.

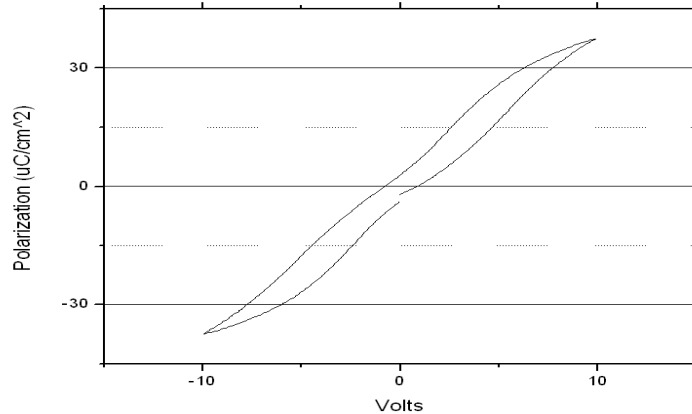


Figure 19. Ferroelectric characterization of a PZT thin film deposited over Si/SiO<sub>2</sub>/TiO<sub>x</sub>/Pt wafer and annealed at 700°C for 60sec.

### 3.1.10 Delamination

The delamination problems previously found in the Si/SiO<sub>2</sub>/Ti/Pt wafers were due to poor adhesion between the Ti and the Pt. This can be seen in Figure 20. In order to improve adhesion, the Ti was exposed to different oxidation processes. First it was oxidized in the RTA with the presence of air. The obtained film didn't show good adhesion properties due to the formation of TiN in the surface. In order to avoid the formation of nitrogen the film was oxidized in an O<sub>2</sub> atmosphere outside the clean room. This showed better results but there were problems with particles contamination. In order to solve this problem a tube furnace

was installed inside the clean room. This made it possible to oxidize the Ti thin films and to facilitate Si/SiO<sub>2</sub> thermal growth inside the clean room. Si/SiO<sub>2</sub> wafers were fabricated, excellent thickness distribution and roughness was obtained, and the obtained thickness was similar to the one predicted by diffusion equations.

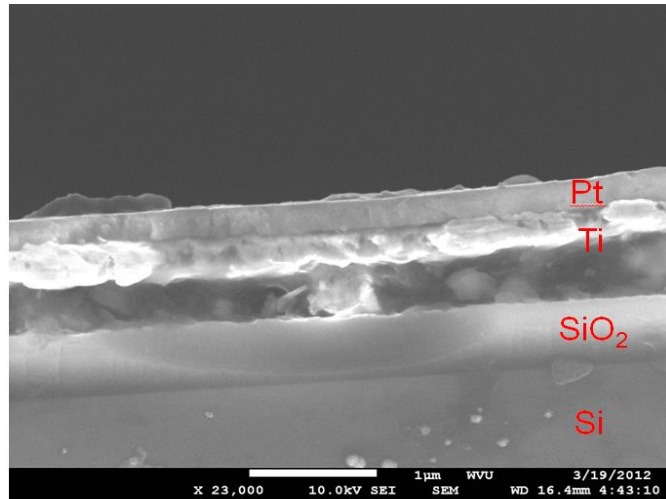


Figure 20. SEM picture of Si/SiO<sub>2</sub>/Ti/Pt thin film showing delamination in the Ti thin film.

After this, different approaches were created. First, a thermal decomposition of Fe and Co acac was made using ethylene glycol as a solvent and oleic acid as dispersant agent. Several thermal decompositions of this system were performed but no particulates were obtained. This was due to the low temperature and low pressure of the synthesis.

### 3.1.11 Solvothermal Synthesis of CFO Nano-particles

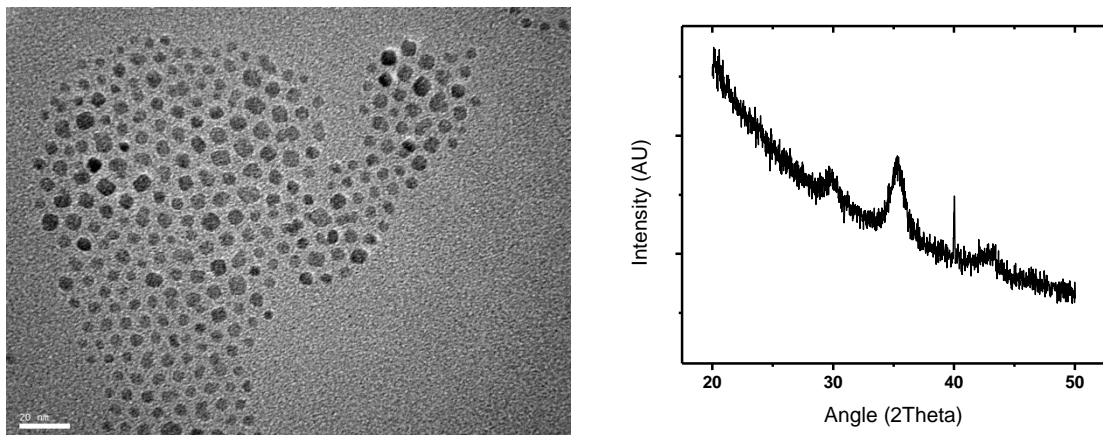


Figure 21. Left, TEM image and right, XRD pattern of CFO nanoparticles.

In order to have a better control of the solvothermal synthesis of CFO nano-particles, several modifications to the process were made in order to achieve good dispersion and retain the nano-size of the particles. As a result of this work, a new synthesis method for producing CFO nano-particles was developed using benzyl ether as a solvent, Co acac<sub>2</sub> and Fe acac<sub>3</sub> as a precursor. The dispersion system used was the 1,12 – dodecanediol, oleic acid and oleylamine system. As a result of this, well-dispersed nano-particles with the desired

crystallography were obtained. As shown in Figure 21 (left), the particle morphology and size can be seen using TEM characterization. The TEM characterization confirmed the narrow size distribution and nano-size of the particles ( $\sim 7\text{nm}$ ). The crystal structure was characterized using XRD diffraction. As shown in Figure 21 (right), the XRD pattern can be seen showing the characteristic spinel structure and the crystallite size was calculated using the Scherrer formula, which confirmed a crystallite size of 6 nm.

After the solvothermal synthesis of the nano-particles, the particles were dispersed in the PZT sol gel and spin-coated in order to obtain a particulate composite. Several approaches and new dispersants were used and finally a process was obtained to disperse the nano-particles in the PZT sol gel. This consisted of the aging of the PZT sol gel and the incorporation of CFO nano-particles in their hexane solution. The resultant solution with the nano-particles remained stable for more than two weeks. After this dispersion study, the thin films were deposited and annealed. These thin films did not show any cracks or delamination problems.

The RCA cleaning procedure was successfully applied to clean the Si wafers from organics, ions and oxides. Various thicknesses for the  $\text{TiO}_2$  were studied and the influence with the adhesion of the Pt and final PZT crystal structure were analyzed. This study showed that more than 2 min ( $\sim 100\text{ nm}$ ) of Ti deposition were needed in order to achieve good adhesion. After this work, the influence of the thermal oxidation of the Ti with the texture of the PZT was studied. As can be seen in Figure below, the oxidation of the Ti layer produces a big (100) texture of the PZT thin film.

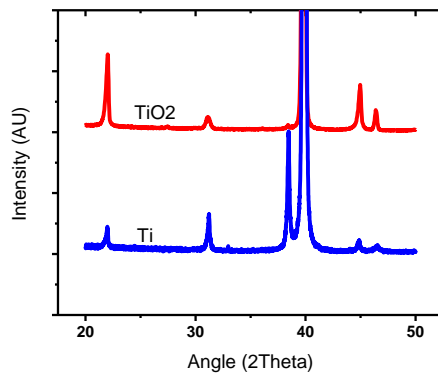


Figure 22. XRD patterns of PZT thin films with and without thermal oxidation.

### 3.1.12 Optimization of CFO Nano-particle Dispersion in PZT Sol-gel

In order to optimize the dispersion of the CFO nano-particles in the PZT sol gel, different studies were completed to control the surface characteristics of the nano-particles, and thus, manipulate the dispersion quality. First, the effect of the hydrolyzation of the PZT in the particle dispersion was studied. Here it was observed that the exposure of the PZT sol to humidity did not have a large influence on the particle dispersion. The effect of aging on the particle dispersion was also evaluated for different time periods. As it can be seen in figure 1, the dispersion improves with aging within the solvent system. The surface peptization kinetics were limited. Here it was found that the particles could be successfully dispersed into the PZT sol but long periods of time to obtain complete dispersion would be needed.

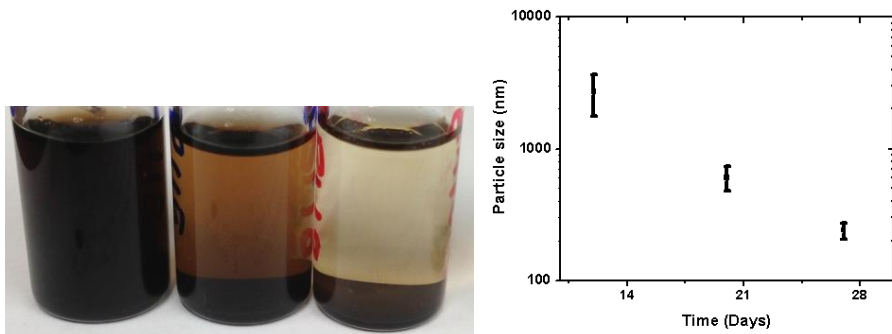


Figure 23. Left, pictures of PZT sol with CFO nano-particles after; right, 2 days, middle 10 days, left 19 days. Right, particle size average after different periods of time.

In order to decrease the required peptization time the sample was agitated for one day in order to investigate the improvement of the dispersion. The results obtained can be seen in Figure 23 (left). This did not improve substantially the peptization rate. As a second approach, different dispersants were used. As previously observed, the particle surface coordinates with  $-\text{NH}_2$  groups and in order to be able to disperse the nanomaterials in 2-methoxyethanol with greater kinetics. With this in mind, dimethylformamide and diethylenetriamide were added to the PZT sol. The results obtained can be seen in Figure 23 (right). The addition of dimethylformamide did not improve the dispersion, but the use of diethylenetriamide improved the dispersion drastically. This is because of the  $-\text{NH}_2$  terminal group and the polarity of the molecule. This gives an efficient way to prepare the PZT sol with CFO nano-particles well dispersed in a short period of time. Having a reproducible process to fabricate PZT sol with CFO nano-particles with different CFO loadings from 1 to 40% was fabricated.



Figure 24. Left, pictures of PZT sol; left without shaking, right with shaking. Right, pictures of PZT; left without dispersants, middle with dimethylformamide and right with diethylenetriamide.

With the above procedure, the first particulate composite was fabricated. In this case, a CFO loading of 2% was selected and the process described in Figure 25 was followed to obtain the composite thin film. This new deposition technique allowed the dispersion to higher concentrations of CFO nano-particles due to the gel coating of the particles. This resulted in films with low leakage current and good quality that were not previously able to fabricate with other processing techniques.

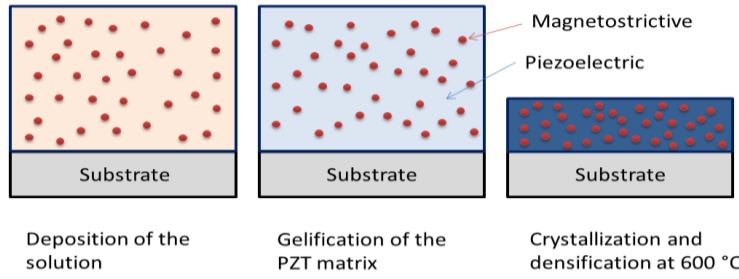


Figure 25. Modified sol gel thin film deposition.

After the films were deposited, the quality was characterized using SEM imaging. The results can be observed in Figure 26. The figure shows that the thickness of the film remained constant after the addition of the CFO nano-particles. The quality of the films was not altered with the addition of CFO particles either.

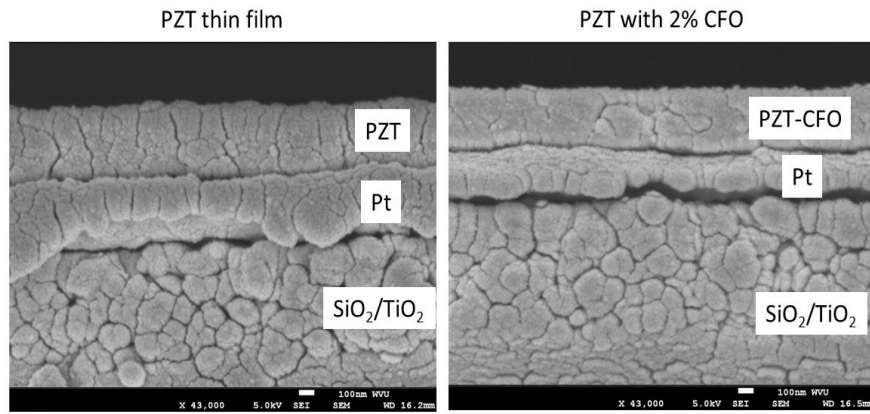


Figure 26. SEM characterization of; left PZT thin film and right PZT with 2% CFO loading thin film.

The crystallography of the films was characterized at different annealing temperatures in order to determine the crystallization kinetics. It was found that with the addition of CFO nano-particles the PZT films crystallize without texture. This is due to the fact that the CFO particles worked as a nucleation sites, and in the case of the pure PZT films, the perovskite structure grows from the Pt wafer, as it can be seen in Figure 27. Another important difference is that the temperature required to obtain 100% perovskite phase is reduced from 650 to 600 °C, without the formation of the non-desired pyrochlore phase.

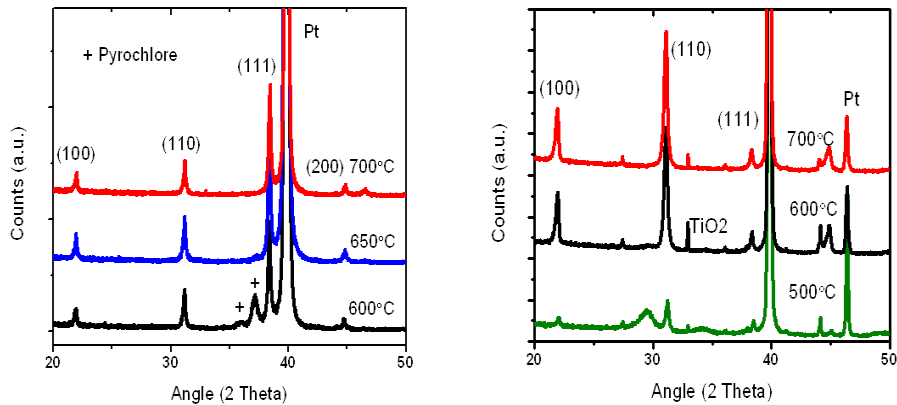


Figure 27. XRD characterization of; left PZT thin films sintered at 600, 650 and 700 °C and right PZT films with 2% CFO loading sintered at 500, 600 and 700 °C.

Finally, the ferroelectric properties of the films were characterized using the Radiant tested whis is depicted by Figure 28. The addition of CFO nano-particles to the films did not generate any leakage currents due to the good dispersion of the particles. In addition, the incorporation of nano-particles increased the remanent polarization and the coercive field, making the films behave more like a hard piezoelectric.

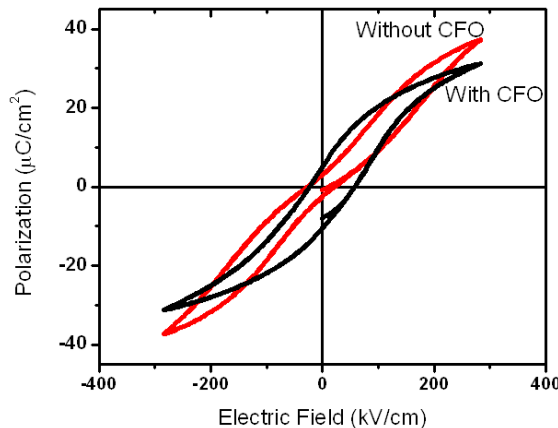


Figure 28. Ferroelectric characterization of PZT films; in red without CFO and in black with CFO nano-particles.

This new technique to fabricate particulate composite thin films provided an effective synthesis to obtain films with high particle concentrations and good dispersion giving as a result a higher ME response. This enabled fabrication of micro-magnetometers with high response in a Si based circuit that could be easily integrated.

### 3.1.13 Micro-Chemical Sensor Array

Photo-lithography and physical vapor deposition processes were developed to produce singular micro-chemical sensors on resistive alumina substrates. Fabrication of the micro-sensors was initiated through the development of processes to pattern gold (Au) interdigitized electrodes (IDE) onto alumina substrates. The initial IDE geometry targeted were four sensors array in a road. The dimensions for the different sizes in the mask are outlined in the following chart. All these dimensions are in microns and correspond to Figure 29.

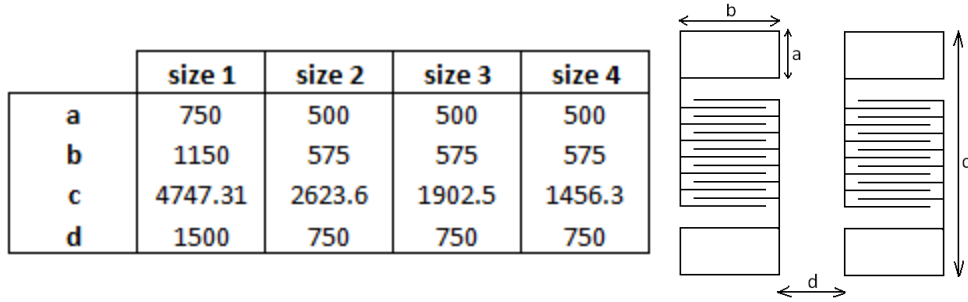


Figure 29. IDEs geometry.

The Au-IDEs were patterned through a basic lift-off process. A Larurell Technologies 400 Series spin-coater was used to deposit AZ5214 photoresist at a thickness of  $\sim 1.5 \mu\text{m}$  onto the alumina substrates. The AZ resist was then baked on the samples for 5 min at  $95^\circ\text{C}$  on a hotplate before being placed in a Suss Microtec MAG mask aligner. The mask aligner then exposed the wafer to UV light through the mask, cross linking the polymer. This model operates at UV wavelength energy of  $100 \text{ MJ/cm}^2$ . The intensity of the light was measured (in  $\text{MW/cm}^2$ ) before each exposure so the exposure time could be determined. After exposure, the wafers were developed using AZ400K developer in a quick immersion. The developer removed the exposed resist and created a void in the shape of the IDE. Following the patterning of the resist, a CVC 610 DC Magnetron sputter station was used next to deposit Au over the entire alumina wafer. First, a titanium coating was deposited onto the wafer to assist with adhesion of the metal to the alumina substrate. A layer of Au was then deposited under an argon plasma flow at 570 volts and 6.0 Torr for 180 seconds. A lift-off process was performed as follows: The substrates were immersed in an acetone bath for 20 minutes and periodically agitated with ultrasonication. This removed the polymer mold and any metal on its surface. The samples were then placed in a methanol bath for 5 minutes, cleaned with de-ionized water, and dried with nitrogen. Two Au IDEs can be seen in Figure 30.

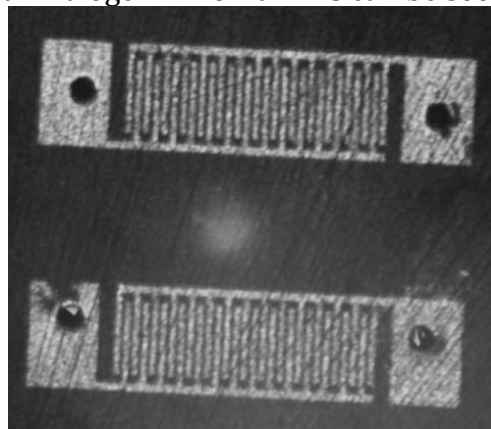


Figure 30. AU IDEs.

### 3.1.14 Multi-step Hydrothermal-Assisted Procedure

The nano-scale CuO pattern was created using a multi-step hydrothermal-assisted procedure. First, alumina substrates with fully developed IDEs were spin coated with AZ 5214 photoresist, using the same spin rates. They were exposed under a negative sodalime photomask from in the Suss Microtec MAG mask aligner. The pads were aligned with the IDE's on the substrate by using a microscope to align the crosshairs on the substrate (made

with the IDEs) with the squares on the mask. Next, the substrates were agitated in the AZ400K developer during a quick immersion. This process created a mold of rectangular pads over the IDE fingers. The dimensions of these pads were proportional to the length of the IDE that they were matching.

The next step in the process was metal deposition via sputtering. The substrates were coated with a layer of Cu using the same sputtering station as in Part 1, with an argon plasma flow at 490 V and 6.0 Torr for 6 seconds to seed the surface. Then a liftoff process was performed again, to reveal Cu micro-pads on top of the micro IDEs.

The alumina/IDE/Cu samples would undergo a templated hydrothermal process to grow Cu<sub>2</sub>O/CuO nanorods on the Cu pad. This was accomplished by forming a highly basic solution (ph of 11.1) of copper nitrate hydrate (Cu(NO<sub>3</sub>)<sub>2</sub>) and de-ionized H<sub>2</sub>O via precipitation with ammonium hydroxide. The solution and alumina/IDE/Cu sample were held in a stainless steel autoclave at 100°C for 1 hour. The powder was characterized using XRD and Cu<sub>2</sub>O/CuO traces were found.

### 3.1.15 Hydrogen Detection Micro-chemical Sensor

A micro-chemical sensor for the detection of hydrogen in humid air was successfully developed. The chemical sensor was constructed on an alumina substrate. The IDEs were made of platinum using a lift-off process. The nano-CuO sensing material was initially patterned onto the alumina substrate and Pt IDEs with a sputtering process. Nano-wire CuO sensing structures were then synthesized through a controlled thermal oxidation process developed over the last month of work.

The micro-sensors were tested in flowing hydrogen for 10 minutes at different concentrations ranging from 500 to 5000 ppm H<sub>2</sub>. The sensors were allowed to recover in air for 20 minutes. During the second third of the test, the sensors were tested in the same concentration conditions, but a faster response was tested by flowing hydrogen gas for only 1 minute and a 20 minute recovery time. In the last part of the test, the fast response of the micro-sensors was tested at a high concentration. Results indicate that the sensors are able to detect high concentrations of hydrogen at times as short as 5 seconds. Test results are shown in Figure 31.

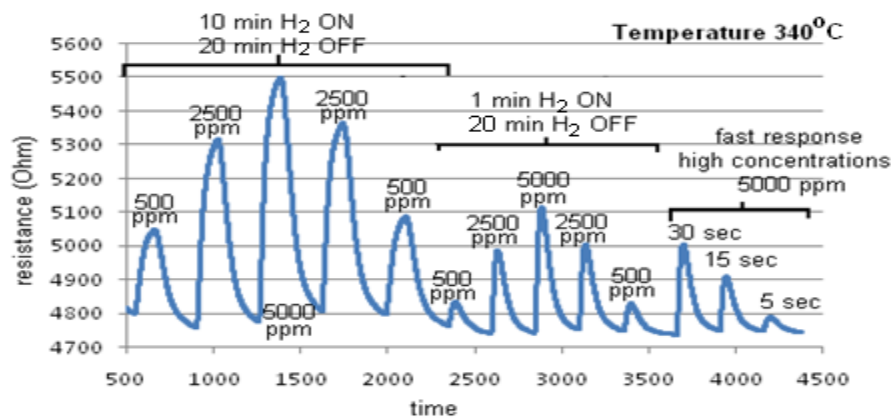


Figure 31. Test results for a hydrogen chemical sensor at 340°C.

A micro-chemical sensor utilizing large grained CuO sensing materials was developed by a sputtering/oxidation process. The IDEs were made of platinum using a lift-off process. The CuO sensing material was patterned onto the alumina substrate by first DC sputtering the Cu across the Pt interdigitized electrodes (IDEs). The Cu metal layer was then oxidized in a controlled environment to produce the continuous CuO layer across all of the electrodes. The resultant microstructure showed CuO grains with little porosity through the microstructure. This indicates that the active surface area for gas reaction was very low resulting in a lower than desired sensing rate. It is well known that by increasing the available surface area for gas interaction with the electrode would result in higher sensitivity and sensing rate.

A hydrothermal process for forming nano-CuO particles was developed. The nano-CuO material was then incorporated into an ink formulation, and this formulation was painted onto the IDEs previously developed. In addition, a micro-casting process for forming distinct shapes over the IDEs was also developed and utilized to micro-print the nano-CuO absorbent material into the desired locations. Figure 32 shows a picture of the final micro-sensor platform after the final processing step. Figure 33 shows a four sensor array built to test H<sub>2</sub>, CO, NO, and NO<sub>2</sub> at the same time. In this case, the lead test wires were attached to the second sensor to test H<sub>2</sub> content within a gas stream.

Figure 34 shows the resultant test data from a representative micro-sensor produced with the above discussed processing methods. This sensor was different from those tested previously, in the case that these contained the desired nanomaterial CuO. The micro-sensors were tested in flowing hydrogen for 10 minute exposures at different concentrations ranging from 1000 to 4000 ppm H<sub>2</sub> (mixed with N<sub>2</sub>). The sensors were allowed to recover in air for 20 minutes. During the second third of the test, the sensors were tested in the same concentration conditions, but a faster response was tested by flowing hydrogen gas for only 1 minute and a 20 minute recovery time. In the last part of the test, the fast response of the micro-sensors was tested at the 4000 ppm level for very short exposure times. The intent of this test was to identify the maximum response rate of the sensor. The figure shows that the sensors were able to detect high concentrations of hydrogen at times as short as 30 to 1 sec. The response shows that a similar diffusion process was required in each case to alter the sensor surface back to the baseline steady state condition.

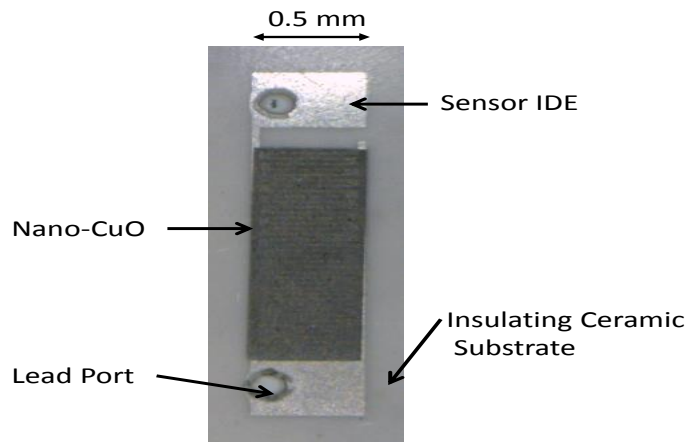


Figure 32. Picture of a singular micro-sensor with CuO nanomaterial absorbents across the IDE pattern.

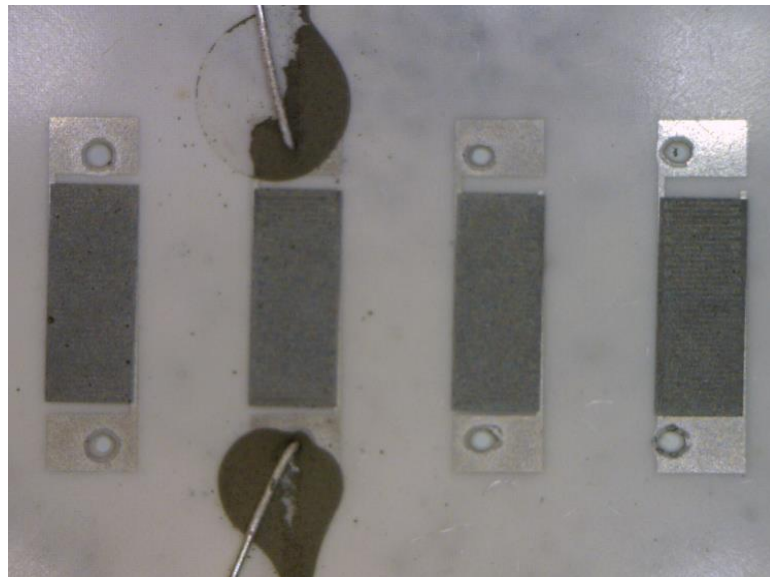


Figure 33. Picture of a four element array of nano-CuO micro-sensors (with one sensor connected through contact via).

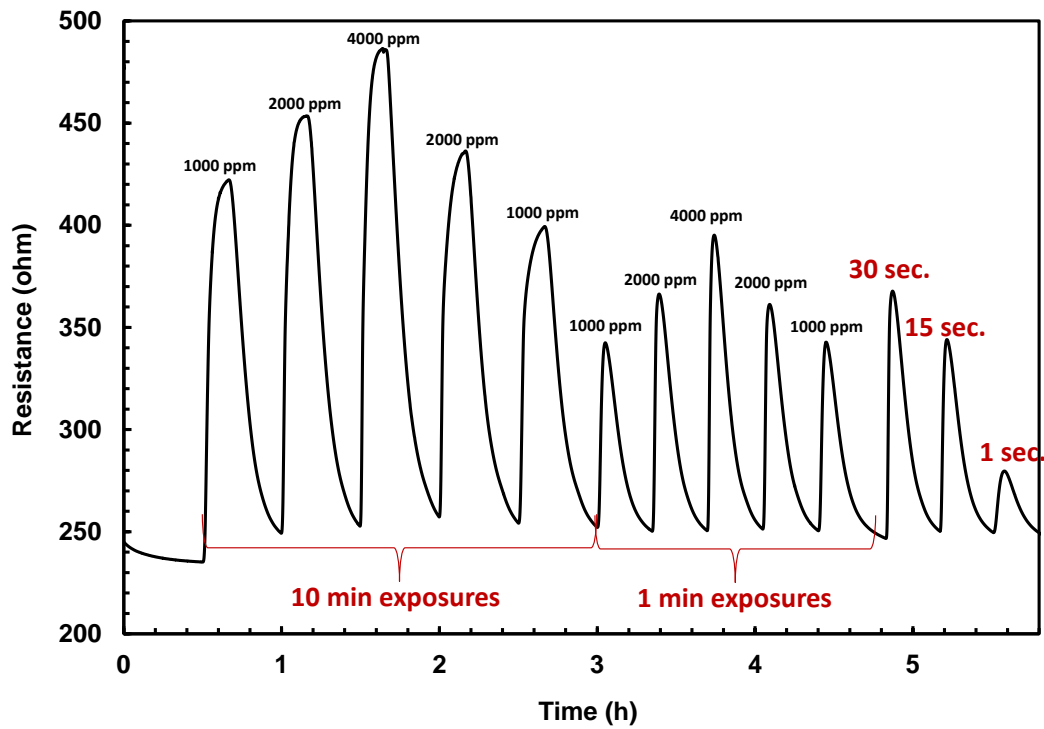


Figure 34. Sensing performance of a singular micro-sensor exposed to different low levels of H<sub>2</sub> for times ranging from 10 min to 1 sec.

### 3.1.16 Fabrication of Micro-chemical Sensors With CuO

Micro-chemical sensors were fabricated utilizing CuO as a sensing material. These sensors may be divided in three groups which differ in the manner that the CuO is deposit over the interdigitized electrodes that all of them share.

These are as follows:

1. Thermally grown CuO
2. Hydrothermally grown CuO nanoparticles
3. Painted with nano-CuO ink

To make the electrodes, the circuits were patterned by photolithography and then an adhesion layer of Zr and a conductive layer of Pt were sputtered over the photoresist. After a typical lift off process, the IDEs of Pt were obtained.

In the first group of sensors, a layer of Cu was sputtered over the IDEs and oxidized to obtain CuO. This method is good because of its simplicity. Previously, the microstructure of the CuO obtained was very dense with grains on the order of micrometer. The direct consequence of this low active surface was on the decrease of sensibility to chemical gases. In order to overcome this problem, nano-needles of CuO were successfully grown on a copper foil. This result encouraged us to recreate the same conditions over a layer of Cu sputtered. Although nano-needles were not obtained the grain size was reduced.

### 3.1.17 Re-creation of Hydrothermal nano-CuO Sensors

Sensors with hydrothermally grown nano-CuO were re-created. In order to do this, the wafers with the IDEs were sputtered with Cu (over a feature patterned by photolithography). The samples were placed in the autoclave horizontally with a basic solution of  $\text{Cu}(\text{NO}_3)_2 \cdot \text{H}_2\text{O}$  and washed in order to obtain the desire pattern. The advantage of this method relies on the possibility to obtain CuO nano-plates that grow on the Cu. The first results showed that the CuO had grown, but not continuously. The CuO was well attached to the Pt electrodes but between them a bridge was not created. In order to overcome this situation, the thickness of the sputtered Pt was reduced to 100nm. The problem of reducing the thickness of Pt is related to the reduction of resistance. A study showed that when Pt film thickness exceeded 100 nm, further Pt deposition had no significant effect on the conductivity improvement. After repeating the hydrothermal growth with the new thickness, the results showed an improvement on the continuity of the CuO. In spite of this encouraging result, the sensor sensitivity was lower than desired.

The third group of sensors was fabricated using the CuO nano-plates created during the autoclave run mentioned before. The idea of this method is very simple. One stencils a CuO over the IDEs by painting them with ink created with the CuO. After the deposition, the sensor is submitted to a temperature cycle in order to eliminate the organics. In the beginning, the created ink did not allow us to obtain a continuous CuO layer. After several attempts, the composition of the ink was changed allowing us to obtain a better control during the deposition (since the viscosity was increased), and also it allowed us to get a continuous layer of CuO over the IDEs.

## 3.2 Subtask 2.2: Ultra-Low Power Analog Event Detection

The objective of this research direction was to develop techniques for building ultra-low-power hardware event-detection systems. The goal was to create dedicated “wake-up” circuits for remotely deployed sensor nodes so that the portions of the sensor node that consume proportionally large amounts of power could be turned off when not needed. As

such, the use of low-power analog circuitry was investigated, that consumes only a few micro-Watts to be used as an energy-management tool to enable the high-power-consuming subsequent digital systems only when action is required. Additionally, this analog circuitry was able to provide initial pre-processing of the sensor information to pre-condition the raw sensor data and provide feature extraction.

Analog systems were specifically investigated for acoustic and vibration sensing systems. For example, Figure 35 illustrates work, which focused on developing a custom integrated circuit that was able to perform spectral decomposition of incoming sensor data, which is analogous to the commonly used digital fast-Fourier, transform in a wide variety of signal-processing systems. This integrated circuit, which was fabricated on a standard  $0.5\mu\text{m}$  CMOS process, consisted of two filter banks and sub-band magnitude detectors that perform spectral decomposition for use by the subsequent classifier. Classification is performed with double-threshold quantization in each band followed by a programmable logic array (PLA) which compares the spectral inputs with stored detection rules. The PLA stored spectral templates which were used to match incoming signals to their respective classes. Once specific classes were observed, the system generated an interrupt signal that wakes up the digital system from a state of hibernation. Figure 35 also includes details on how the custom integrated circuit was interfaced with commercial off-the shelf wireless sensor network nodes, called motes.

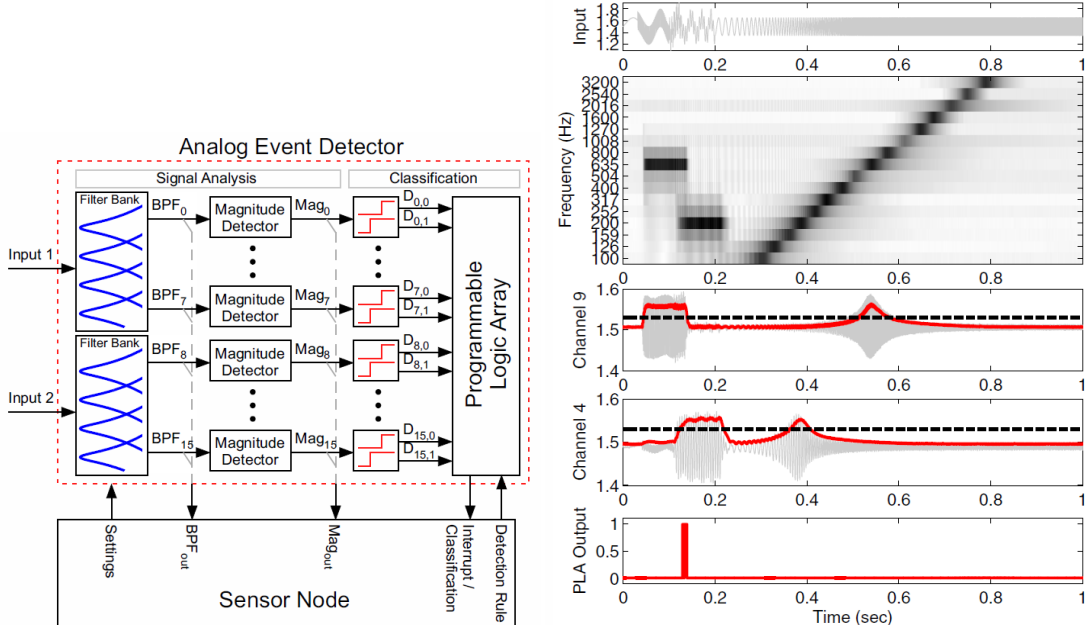


Figure 35. Left, block diagram of the analog event detector, showing how it interfaces with sensing nodes. Right, demonstration of the event detector IC.

Also included Figure 35 is a demonstration of the event detector integrated circuit. In this particular case, the input was a logarithmic chirp with tone bursts at 200Hz and 635Hz, corresponding to channels four and nine (shown in the third and fourth subplots). The second subplot shows the measured magnitude outputs in spectrogram form. The PLA was programmed to perform an AND of those channels, and correctly outputs a "high" (i.e. wake-up signal) when both tones are present.

### 3.2.1 Development of Vehicle Classification System

To evaluate the event detector in the context of a remote sensing application, a vehicle classification system was developed. A dataset consisting of forty 10-second recordings of cars and trucks measured by a microphone was used. The objective was to detect the presence of a vehicle and classify it as a car or truck. Training software was implemented which used half of the recordings to learn the comparator threshold levels and PLA detection rules that best classify an input signal as either a car, truck or no vehicle. The event-detection integrated circuit was tested by streaming the other half of the vehicle recordings from a digital-to-analog converter into the filter bank input. Two PLA output pins were used, including one to indicate vehicle presence and one to indicate car or truck. The mote's microcontroller woke up when the "vehicle presence" pin was asserted. Upon waking, the mote implemented a state machine, monitoring both of the PLA pins and using the sequence of outputs from the PLA to make the final decision. Accuracy and power consumption values are provided in the following Tables, and the power projection plot shows the power consumption of an all-digital implementation, our first system (called "w/ ASP"), and our newer implementation ("Projected Power"). As can be seen in Figure 36, for a low frequency of events, our complete ASP system combined with a digital mote can be expected to continuously operate for approximately 9 years off of two AA batteries.

#### SPECIFICATIONS

VEHICLE CLASSIFICATION RESULTS				Specification	Value	Device	Power
		Ground Truth		Chip Area	2.25mm <sup>2</sup>	Filter bank	1.49μW
		NULL	Car	Channels	16	Comparators & PLA	10.5μW
Missed		20%	0%	Chip Power	27.8μW	Read-out buffering	15.78μW
Car	0 false alarms	70%	10%	Supply Voltage	3V	External biasing	18.9μW
Truck	0 false alarms	10%	90%	Technology	0.5μm	ASP + Biasing	46.7μW
				Frequency Range	20Hz-100kHz	Mote (sleep)	78μW
				Dynamic Range	50dB	Mote (awake)	1.5mW
						Mote (transmitting)	60mW

Figure 36. Vehicle Classification results and Chip Specifications

### 3.2.2 Development of Motion Detection Systems

Research was conducted toward the design of motion detection systems using custom CMOS imagers. We demonstrated a one-dimensional motion detection system based upon the visual system of a housefly that was able to wake up a larger camera network in the presence of motion in a specific direction. This analog motion detector operated in the 10s of microwatts of power. To supplement the operation of this motion detector, we designed a speed-detection circuit that was able to determine how fast an object is moving in a specific direction. The speed estimate can be combined with the biologically inspired motion detection system to provide further information of the object under view when the wakeup signal is generated.

When developing these analog circuits, dynamic range was an important consideration, and ultra-low-power analog circuits typically had extremely small linear ranges that limit the largest signal that can be operated upon. As a result, a technique was developed to increase the linear range of operational transconductance amplifiers, which are a basic building block

of low-power analog circuits. This technique used an effective adaptive biasing by using floating-gate transistors, which are the core element of digital Flash memory). These traditionally digital memory elements were used for analog applications, and were able to increase the linear range of operational transconductance amplifiers by a factor of 16 or more.

Floating-gate transistors were also used to help extend the dynamic range of analog circuits, which was an extremely important consideration for low-power and low-voltage circuits. As a result, a technique was developed to increase the linear range of operational transconductance amplifiers, which are a basic building block of low-power analog circuits. This technique used an effective adaptive biasing by using floating-gate transistors. Figure 37 illustrates the extension of the linear range of operational transconductance amplifiers. By adjusting the programmed charge on the floating gate, the linear range of these amplifiers were increased (as indicated by a straightening of the line in the left-hand plot) which can be seen in Figure 37. Figure 37 also depicts the tradeoff of a reduction in the transconductance of the amplifier (as shown on the right), but the transconductance became more constant over a larger range of voltages, making this circuit easier to use in many situations.

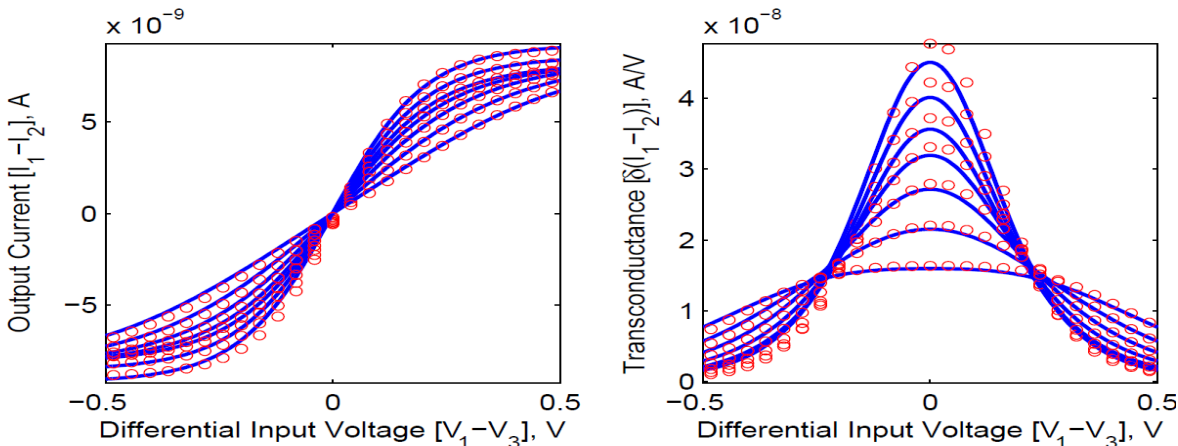


Figure 37. Increased linear range of amplifiers (left) and reduction in the trans-conductance of the amplifier (right).

### 3.2.3 Reverse Tunneling

Considerable progress was made in identifying the causes of certain of the non-idealities (including something called “reverse tunneling” that causes the charge on the floating gates to be less than the desired/programmed amount). Ways to better isolate the floating-gate transistors to remove this unwanted effect were investigated. Performance of two types of “tunneling junctions” in terms of speed of programming and charge retention were also performed.

Investigations into building ultra-low-power short-term memory that did not require going through a high-power analog-to-digital converter and then being stored in some sort of conventional memory system (e.g. RAM or Flash memory) were performed. The theory was that if a wake-up detector was used to find an important event, then all information leading up to that event would be lost (since the higher power system only wakes up once an event

has been seen). This missing information was a problem with any type of wake-up detector. Ways were sought to temporarily store analog information without the cost associated with converting it into the digital domain. A proof-of-concept peak detection system was built that shifts select information of a signal into an array of capacitors to hold the data for a short period of time. This circuit effectively sampled the signal at select times and conveyed that amplitude value and the timing value to the capacitor array (i.e. the short-term memory).

### 3.2.4 Development of Analog Signal Processor

A new *programmable* analog signal processor (ASP) was developed that was capable of performing spectral decomposition, matching spectral content to a “trained” set of templates for classification purposes, and then waking up a subsequent digital system when an event of interest has been identified. To verify the performance of the new ASP architecture, we used our ASP to perform vehicle classification while the digital portions of the sensor node were in sleep mode to save power. When the ASP detected the presence of a vehicle, the ASP woke up the microprocessor and antenna for further processing and communication, respectively. The microprocessor, once awakened, was used to provide further refinements to the classification of the sensed phenomena. The power savings of using the new ASP core were significant. A fully digital implementation performing the same task could only survive on a single battery for only up to a few months. Using the ASP allowed the system to remain on for a projected 7-9 years. Figure 38 illustrates the architecture of our ASP as well as the projected power savings.

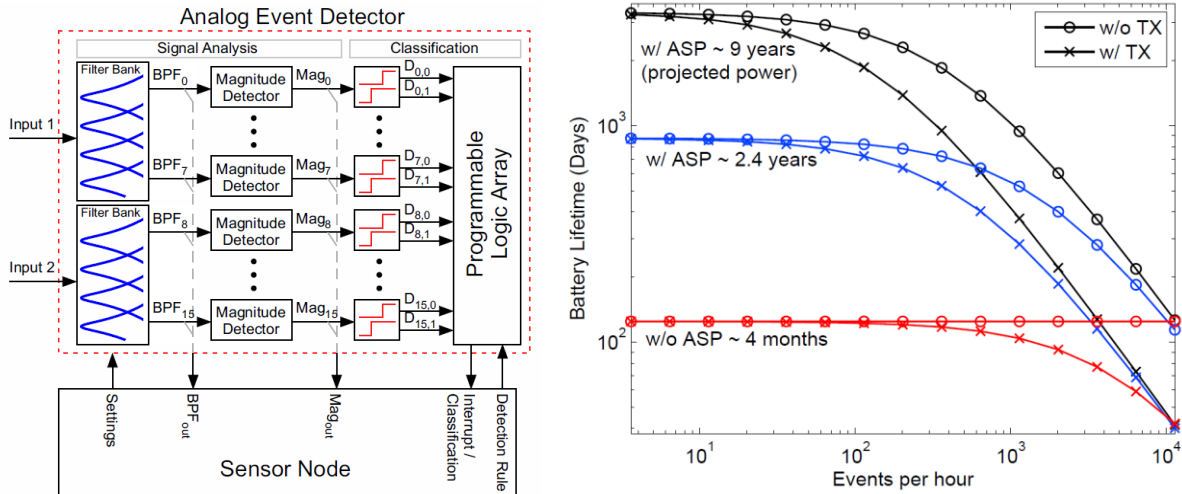


Figure 38. Left: block diagram of our analog event detector, showing how it interfaces with sensing nodes. Right: comparison of the power consumption of our ASP approach versus all digital vehicle classification systems.

This new ASP required significant improvements to the infrastructure to provide for programmability, reconfigurability, accuracy, and precision. The most significant improvements to the infrastructure were made by introducing floating-gate transistors to serve as programmable analog elements. During this course of this project, the following key advances in floating-gate transistor infrastructure were made, including (1) a fine-grain, high-accuracy programming algorithm using Matlab in the loop, (2) the creation of a high-voltage charge-pump to generate the voltages necessary for programming on the chip (to reduce external circuitry requirements), (3) implemented a simulation model for floating-gate transistors within the Cadence simulation environment, and (4) the initial development

of basic “self-programming” floating-gate circuits. In addition to creating this new necessary infrastructure, considerable time was spent characterizing floating-gate transistors across multiple processes in order to better understand the device physics related to long-term retention and the most power-efficient programming techniques.

This circuit effectively sampled the signal at select times and conveyed that amplitude value and the timing value to the capacitor array (i.e., the short-term memory). The result was that the sampling rate was adapted as the frequency content changed so that the signal was constantly sampled at the “instantaneous” Nyquist rate. Since sampling was at irregular time intervals, considerable time was spent determining how to reconstruct the original since the typical Shannon-Whittaker reconstruction method (i.e., scaled and shifted sinc pulses) did not apply to this system. Three completely unique reconstruction methods were developed (asymmetric sinc functions, asymmetric sinc-squared functions, and Bezier polynomials) that perform reasonable reconstruction. Figure 39 shows the reconstruction of a speech waveform. Traditional Nyquist-rate sampling would require  $> 10,000$  samples, and the adaptive sampling system compresses the data into only 652 samples, all while consuming slightly over  $1\mu\text{W}$  of power.

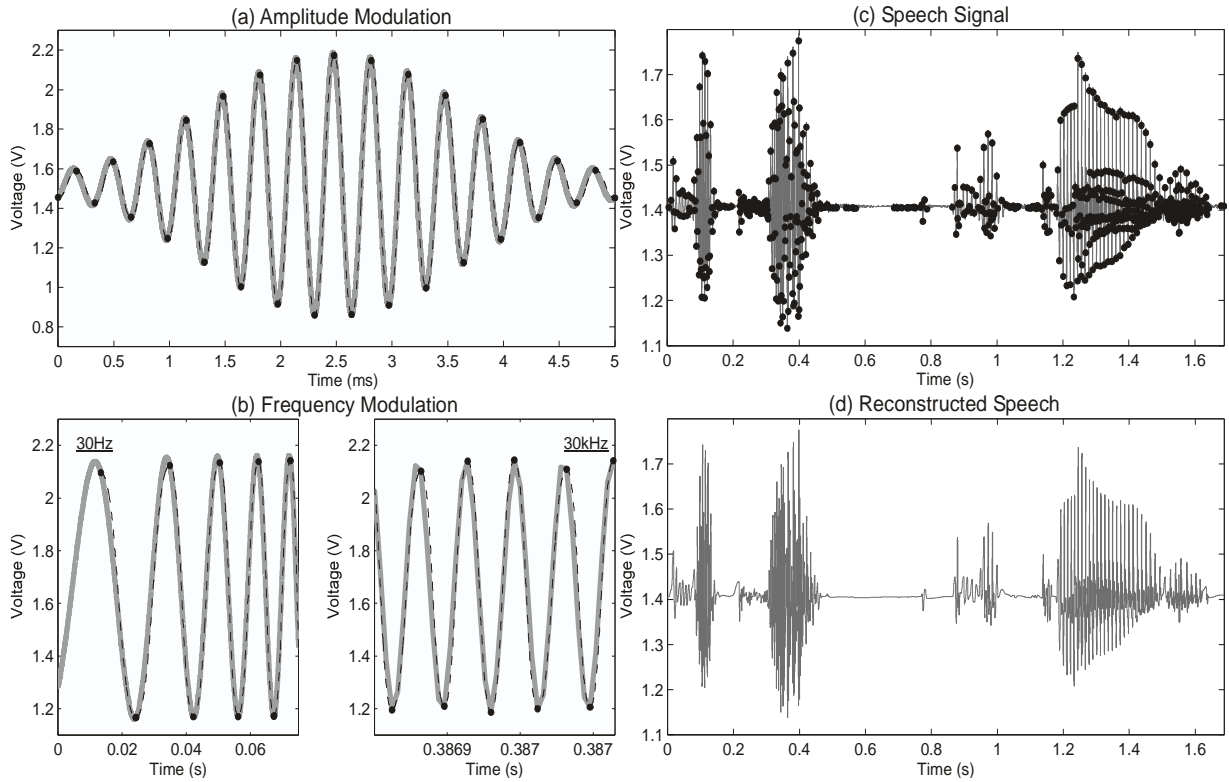


Figure 39. (a-b) The system is capable of capturing a wide range of amplitudes and frequencies. For these plots, the input is shown in grey, detected max/mins are black dots, and the reconstructed wave is a black dashed line. (c) The speech clip used as input to the system is shown in grey with detected max/mins in black dots. (d) The speech clip approximation from using the modified Bezier formula with the sampled max/mins.

This work began with populating the new printed circuit boards (PCBs) that were designed and verified. With those PCBs properly working, the testing of the integrated circuits was initiated. This integrated circuit contained a large number of stand-alone test cells as well

as several integrated systems. The major circuits and systems consisted of (1) floating-gate transistor characterization circuits and infrastructure, (2) reconfigurable analog arrays, and (3) an improved version of the short-term analog memory buffer that was prototyped. All of the test cells and systems have been tested and their operation has been verified; all circuits and systems operate as designed.

Figure 40 depicts a top view of the integrated circuit. Figure 41 depicts the PCB, while Figure 42 displays the results of the integrated circuit (one component of the analog sampler system.)

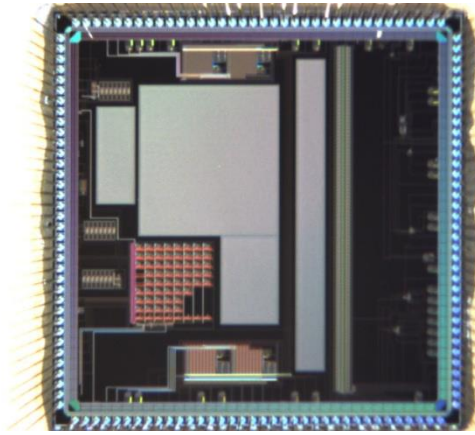


Figure 40. The integrated circuit.

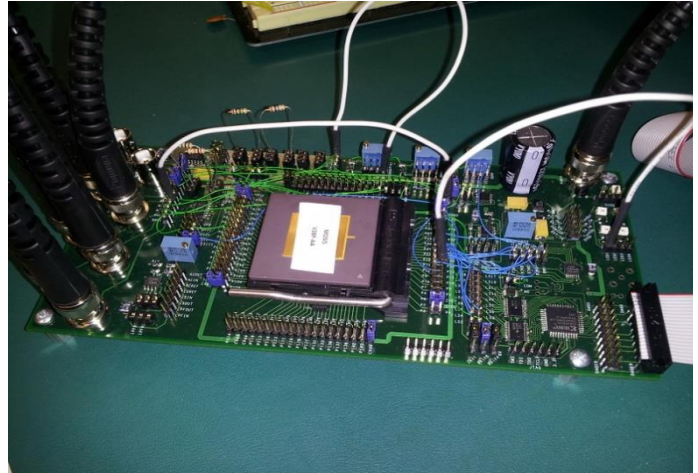


Figure 41. The PCB

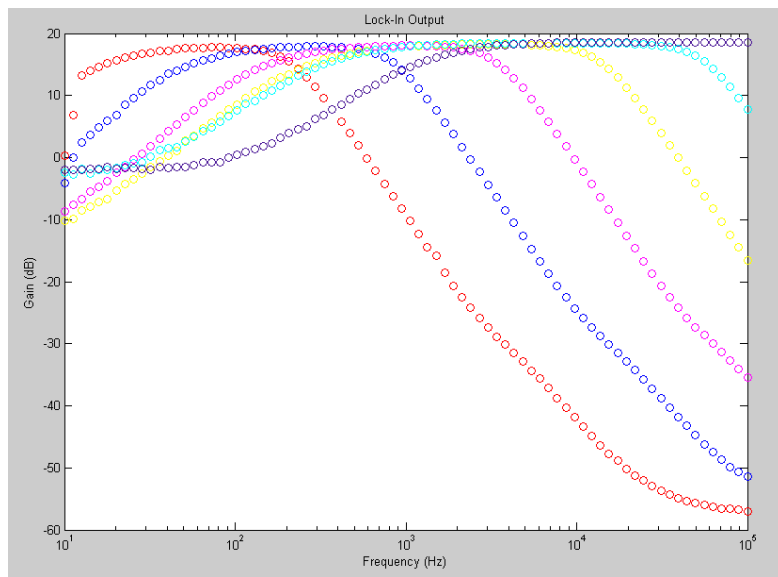


Figure 42. Results of the integrated circuit.

### 3.3 Subtask 2.3: Compressive Sampling and Low-power Collective Sensing

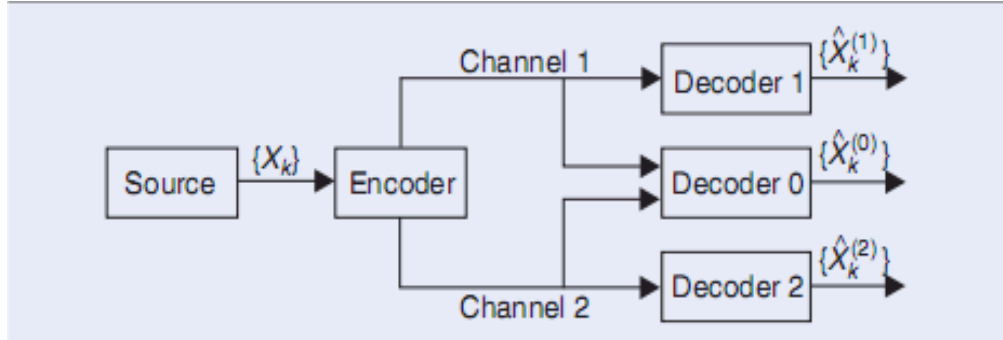


Figure 43. Illustration of multiple-description coding (MDC) for two channels and three receivers (Decoder 0 – central receiver; Decoder 1 or 2 - side receiver).

Two complementary directions were explored for robust image transmission through sensor networks: multiple description coding (MDC) and error-resilience coding (ERC). MDC was originally proposed for error resilient transmission of images in communication networks. It represented an alternative approach toward exploiting diversity to fight against channel errors to forward error correction (FEC). Figure 43 shows a general diagram for transmitting a source (e.g., an image) through two channels (i.e., generate  $M=2$  descriptions). Depending on the network condition, two kinds of decoding conditions at the receiver could be observed: 1) both descriptions are successfully received which is often called central receiver; 2) one description is lost during the transmission, which is often called side receiver.

A key innovation was the nonlocal regularization (which was previously exploited for concealing lost blocks) can be combined with an arbitrary number of observation constraint sets (i.e., successfully received descriptions). This was a natural extension of previous work on maximum a posterior (MAP) decoding from point-to-point communication to network communication. Apparently, if the two-bit streams (descriptions) contain identical information, nothing could be gained. As long as they were complementary to each other – e.g., one was the translated version of the other one, potential gain existed (note that wavelet transform used by SPIHT is NOT translation invariant). A maximum-likelihood (ML) decoding enhances the reconstruction result by taking the average of two (the PSNR gain over single-description is around 1dB). It was found that if the ML was replaced by MAP decoding, another 1dB gain could be achieved and visual quality improvement was noticeable too (see Figure 44).

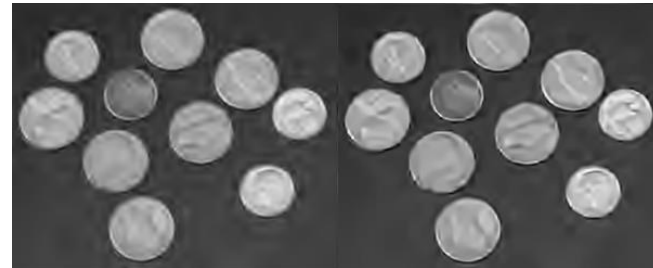


Figure 44. Top: decoded image at the side receiver (PSNR1 = 26.42dB, PSNR2 = 26.24dB) by SPIHT at the bit rate of 0.1bpp. Bottom: decoded image at the central receiver by different algorithms: left - ad-hoc averaging of two decoded versions (PSNR=27.30dB); right - MAP decoding from two received bit streams (PSNR=28.36dB).

### 3.3.1 Error Resilient Image Coding.

A joint TIP paper [5] was written which extended current state-of-the-art image coding SPIHT from error-free to error-prone situations. The basic idea was to replace the conventional significance map by a new data structure named *progressive significance map*. The new data structure was less sensitive to random channel errors because it prevented catastrophic error propagation. The preliminary experimental results (as shown in Figure 45) justified the superiority of error-resilient SPIHT in error-prone environments.

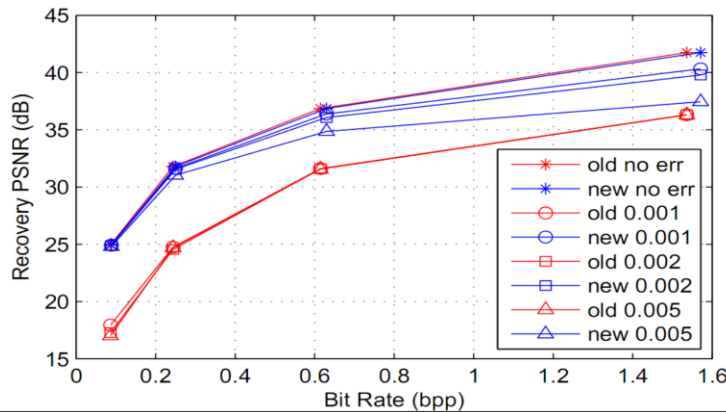


Figure 45. Rate-Distortion performance comparison between conventional (old) and error-resilient (new) SPIHT algorithms on Lena image.

Work was performed on extending our previous work on collective sensing [6] and nonlocal sparsity-based image recovery [7] into error concealment applications. The original work was based on the assumption that some blocks were missing but the remaining are distortion-free. In real-world scenarios, such assumption is seldom satisfied because of the quantization distortion introduced at the encoder. Therefore, the quantization constraint could be handled by borrowing ideas from [6] where it has been shown how nonlocal sparsity helps lossy image decoding. The experimental results (as shown in Figure 46) have shown some promising improvement over previous work.

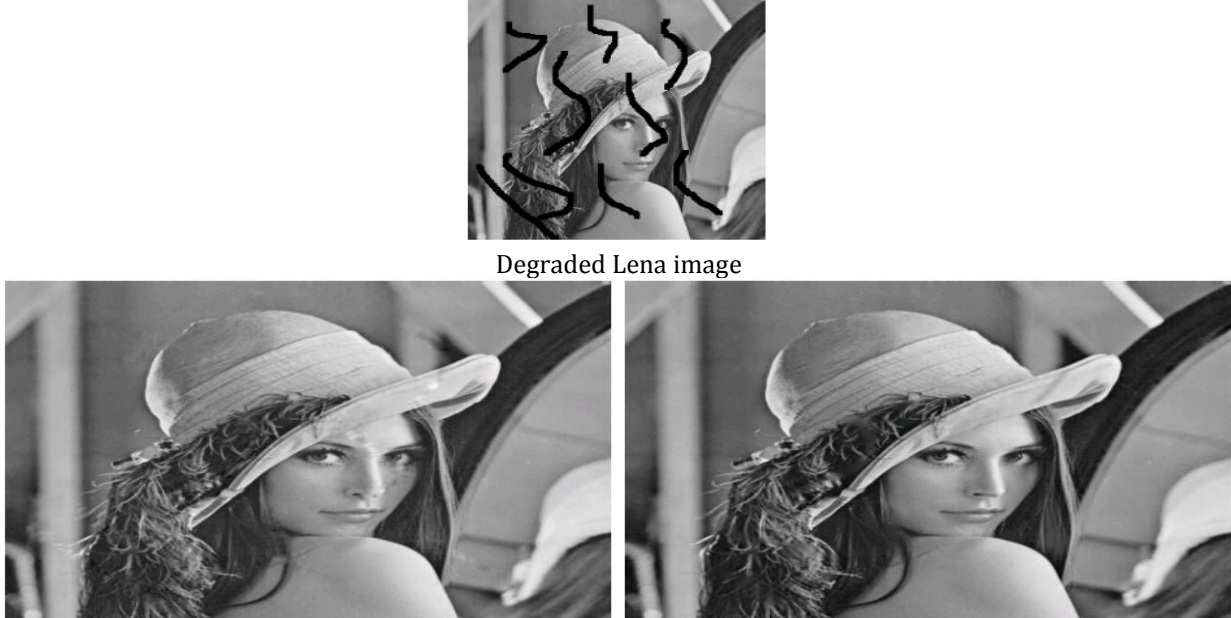


Figure 46. Error-concealment performance comparison between morphological component analysis (MCA)-based (left, PSNR=22.17dB) and ours (right, PSNR=24.30dB) on lena512 image [6].

### 3.3.2 Open-source Implementation of SPIHT Image Coding.

After meeting with Trident personnel and discussing their immediate need, it was agreed that exploration to the feasibility of using wavelet-based SPIHT algorithm to compress images acquired by the sensor node was necessary. The SPIHT algorithm admitted an open-source implementation called Qccpack that was developed and tested on Feroda Linux.

### 3.3.3 Integrate Image Codec at the System Level.

Image compression as located at the application layer needed to work with other applications as well as network and physical layers in practical transmission scenarios. On one hand, the connection of image compression with high-level vision tasks such as object detection and tracking was explored. On the other hand, there was a necessity to understand how the image source matched with the characteristics of channel. In an ad-hoc network environment, optimization of image transmission at the network level seemed an under-investigated topic and worth further research.

### 3.3.4 Error Concealment for Multiple-description Coding.

The idea of multiple description coding (MDC) was to exploit diversity (e.g., multiple antennas at the transmitter or receiver) as a means of fighting against channel impairment (e.g., fading). In fact, many error concealment techniques were also based on exploiting diversity (redundancy) with the image source such as self-repeating patterns of textures.

### 3.3.5 Low-rank Approximation for Simultaneous Sparse coding.

Work was performed on the problem of joint dictionary learning and group sparsity optimization (a.k.a. simultaneous sparse coding). Motivated by the success of low-rank methods in matrix completion and denoising, novel image denoising algorithm was developed called low-rank approximation simultaneous sparse coding (LASSC) [8].

The concept of low-rank approximation has also been generalized to facilitate the compression of multiple images and has also been generalized into image interpolation, inpainting and compressed sensing. A journal article [9] and two conference papers were submitted related to this line of research.

### 3.3.6 Local Self-examples for Image Resizing and Super-resolution.

Inspired by the recent advance in video/image upsampling from local self-examples [10], other potential applications were explored, such as content-aware resizing of satellite images and resolution enhancement of face images. Such local self-similarity could also be exploited by image compression algorithms tailored for a specific class of images (e.g., satellite or face).

### 3.3.7 Network-centric SPIHT Image Coding.

Based on previous work [5], new frontiers of combining error-resilient SPIHT with multiple-description coding (MDC) and network coding were explored. The basic idea was to jointly exploit the diversity at both the source (e.g., multiple and progressive descriptions) and channel (e.g., physical and network layer) sides. How to accommodate the redundancy and discrepancy arising from a heterogeneous network scenario (e.g., images codes by JPEG and SPIHT respectively) was new research topic that has not been well understood. The goal was to demonstrate some initial gain over previous work on networking image coding for multicast [11].

Work was performed on extending current state-of-the-art image coding SPIHT algorithm from error-free to error-prone situations. The error-resilient SPIHT algorithm was based on the idea of introducing progressive significant map and designing fixed-length codes for location-related source information. It was experimentally verified that the new error-resilient SPIHT algorithm outperforms the original in an error-prone environment. This line of research produced one journal publication [5].

Investigations on the idea of combining error-resilient SPIHT with multiple-description coding (MDC) and network coding were performed. In order to jointly exploit the diversity at both the source (e.g., multiple and progressive descriptions) and channel (e.g., physical and network layer), it was proposed to study a biologically inspired representation of data by their associative relationship.

Moreover, the idea of network-aware image coding could be further generalized into combining the strategy of multiscale source representation (redundancy at the source) with the self-similar topology of network (redundancy of the channel). Unlike existing networking coding for P2P streaming, focus was placed on a theoretical understanding of how to transport a single source that is hierarchically organized (e.g., natural images) to multiple destinations, which can be viewed as a multiscale generalization of multiple-description coding (MDC) problem for broadcasting channel. The initial study with toy examples showed that it is possible to reorganize the representation of source to facilitate the information flow through a hierarchically-organized network (e.g., internet whose traffic demonstrates the character of self-similarity).

### 3.3.8 Joint Source-channel-network Image Coding.

The idea of combining error-resilient SPIHT with multiple-description coding (MDC) and network coding was investigated. In order to jointly exploit the diversity at both the source (e.g., multiple and progressive descriptions) and channel (e.g., physical and network layer), it was proposed to study a biologically inspired representation of data by their associative relationship. Such associative data representation admits a metric-space analysis and had the potential of matching the hierarchical structure of communication networks. The next goal was to experimentally demonstrate some initial gain over previous work on networking image coding for multicast [12].

Extending the work on progressive significance map was published in the teams recent work [5]. The basic idea was to combine the strategy of multiscale source representation (redundancy at the source) with the self-similar topology of network (redundancy of the channel). Similar idea was studied in [13] for P2P streaming; while outs focused more hierarchical extension of network coding from a theoretical perspective (e.g., the generalization of original butterfly network to a multi-scale topology).

Unlike [12] for P2P streaming, focus was placed on a theoretic understanding of how to transport a single source that is hierarchically organized (e.g., natural images) to multiple destinations, which could be viewed as a multiscale generalization of multiple-description coding (MDC) problem for broadcasting channel. The initial study with toy examples showed that it was possible to reorganize the representation of source to facilitate the information flow through a hierarchically-organized network (e.g., internet whose traffic demonstrates the character of self-similarity).

### 3.3.9 Image Compression for Pattern Recognition.

Work on the development of recognition-targeted image compression algorithms (e.g., better preserve the feature useful to pattern recognition than intensity values) was performed.

### 3.3.10 Low-rank Approximation for Computational Imaging.

Motivated by the success of low-rank methods in matrix completion and denoising, a novel low-rank solution to the problem of simultaneous sparse coding (LASSC) was developed [9,

12, 14]. On theoretical side, a new bilateral variance estimation interpretation was obtained and on the practical side, its application into multispectral imaging was explored.

### **3.3.11 Low-rank Methods for Image Restoration.**

Motivated by the success of low-rank methods in matrix completion and denoising, a novel image denoising algorithm based on spatially-adaptive iterative singular-value thresholding was developed [12]. On the theoretical side, a new bilateral variance estimation interpretation was obtained and on the practical side, its applications into multispectral and low-illumination imaging was explored.

Motivated by the success of low-rank methods in matrix completion and denoising, the previous work into image restoration, superresolution and compressed sensing was extended [9, 13, 14]. Two new NSF proposals were developed and submitted to NSF CCSS and CIF programs respectively.

### **3.3.12 Source Coding for Pattern Recognition.**

The definition of image quality heavily depended on the application scenario (e.g., image coding vs. pattern recognition). A high-quality JPEG compressed iris image with severe eyelid occlusion could have little merit from the recognition point of view. It was desirable to extend the previous work [14] into a network-aware situation – i.e., to understand the impact of network transmission uncertainty on recognition performance.

Recognition-targeted image compression algorithms were developed (e.g., better preserve the feature useful to pattern recognition than intensity values).

Such line of research was inspired by the success of sparsity in both image compression and pattern recognition – how to obtain a sparse yet redundant representation of images to support both low-level and high-level vision. The long-term objective along this line of research was to gain a deeper understanding of the connection between two seemingly distant fields – source coding vs. pattern recognition. The underlying hypothesis was that a generalization of vector quantization in source coding could shed novel insight to the problem of pattern recognition (e.g., binary classification can be viewed as a 1-bit quantization problem).

## 4 Task #3: Design, test, and demonstrate real-time fault-tolerant protocols for data aggregation, inference, location tracking, and connectivity maintenance in a mobile heterogeneous sensor network.

### 4.1 Subtask 3.1: Distributed Coding and Data Exchange in Heterogeneous Sensor Networks

The problem of physical field estimation produced by an object or subject using sensory data collected by a distributed sensor network was a challenging problem. While the problem was approached by researchers working in the field from a variety of perspectives [15, 16], in its general form it was not been fully solved. Its general statement requires involvement of general models as well as general constraints on power and bandwidth. The teams approach initially involved basic simplified models and constraints and relied on classical estimation theory.

#### 4.1.1 Unknown Object Location and the Strength of Physical Field

It was assumed that distributed network of heterogeneous sensors acquired samples of a physical field. Consider, for example, a distributed network composed of magnetometers, which senses a magnitude of magnetic field generated by some ferromagnetic object positioned in a vicinity of sensors. A ferromagnetic object can be modeled as a simple dipole generating a magnetic field with the field decaying as the inverse cube of the distance to the dipole. In a typical sensor network, the location of the dipole is not known as well as a type and size of the object, which was characterized by the strength of the magnetic field. It was further assumed that the sensor network was calibrated in the sense that the relative locations of the sensors distributed over some area were known. Sensors act independently of one another and take noisy measurements of the physical field. If the bandwidth of the network is constrained, each sensor would have to encode its data and communicate encoded data to the fusion center for a join field reconstruction. In this initial work, it was assumed that both sensory noise and the noise in communication channels was white Gaussian with known statistics, that channels do not interfere and that the encoding is performed through deterministic quantization by using a completely specified  $M$  level quantizer.

Mathematically, this problem can be formulated as follows. Assume that a network of  $K$  sensors covers a known area  $A$ . Let  $\nu_1, \dots, \nu_M$  be known reproduction points of a least-square quantizer with  $M$  levels. Then the join log-likelihood of the observed sensory data at the fusion center,  $z_1, \dots, z_K$ , is

*Equation 1*

$$l(z) = \sum_{k=1}^K \log \left( \sum_{j=1}^M p_{k,j} \exp \left( -\frac{(z_k - \nu_j)^2}{2\eta^2} \right) \right),$$

where  $p_{k,j}$  are the probabilities for the output of the sensor  $K$  to be mapped to the  $j$ -th reproduction point during the encoding process

*Equation 2*

$$p_{k,j} = \int_{\tau_j}^{\tau_{j+1}} \frac{1}{\sqrt{2\pi\sigma^2}} \exp\left(-\frac{(t - G_k)^2}{2\sigma^2}\right) dt,$$

$\sigma^2$  and  $\eta^2$  are the variance of the sensory noisy and the variance of the Gaussian noise in communication channels, respectively, and  $G_k$  is the sample of the physical field at the location of the  $K$ -th sensor. The function  $G(x, y)$  is an implicit function of the three unknown parameters that have to be estimated at the fusion center. The parameters are  $\mu$ , the strength of the field and  $(x_c, y_c)$ , location of the object generating the field.

This problem was formulated and solved using Maximum Likelihood approach, where the solution was the set of the three parameters that maximized  $l(z_1, \dots, z_K)$ . Since the expression for the log-likelihood function was highly nonlinear in unknown parameters, an iterative algorithm was used to find the solution. First, a set of Expectation-Maximization iterations was formulated and then used nonlinear optimization functions from Matlab (nonlinear least squares) to solve for iteratively updated estimates of the parameters.

#### 4.1.2 Distributed Coding and Estimation

A numerical solution to the problem of physical field estimation from noisy sparse measurements acquired by a sensor network was implemented and demonstrated. This estimation problem relied on the following assumption. It was assumed that each object of interest was characterized by a physical field. The physical field was measured by a heterogeneous wireless sensor network. The density of the network, area covered by the network and type of local and channel noise were design parameters and varied. To meet the requirement of minimum bandwidth, sensors recorded independent measurements of a physical field, then locally quantized them and communicated their quantized measurements to the fusion center for joint processing.

Given noisy quantized measurements of an unknown field (shape was known, but parameters were not), the task of the fusion center was to estimate the spatial distribution of the measured field. Due to the probabilistic nature of quantized measurements, a Maximum Likelihood (ML) estimation approach was adopted. A set of iterative equations implementing Expectation Maximization (EM) algorithm was developed. The equations were solved numerically by involving Newton's linearization.

In the example illustrated below, 15 basic sensors were placed at random within an area of size 8-by-8 meters. The sensor locations were assumed to be known to the fusion center. A 2D Gaussian distributed field was generated for our experiments and sampled by the sensors in the sensor network. Recall that the assumption was that the shape of the field is known, but the strength of the field and the location of the object generating the field were unknown.

To generate the noisy quantized realizations of the sensory data, a realization of Gaussian noise was added to every local measurement. Samples were locally quantized by a uniform quantizer with 8 levels and transmitted to the fusion center over parallel white Gaussian channels with the variance of noise 1. The results of estimation by using the iterative approach are shown in Figure 46. With the initial guess of the strength of the field  $\theta_1 = 12$  and the object location  $(\theta_2, \theta_3) = (3,3)$  it took 450 iterations for the algorithm to converge to the final value of the estimates. The true parameters used to simulate the samples of the field generated by an object were magnitude 10 and location (4,4).

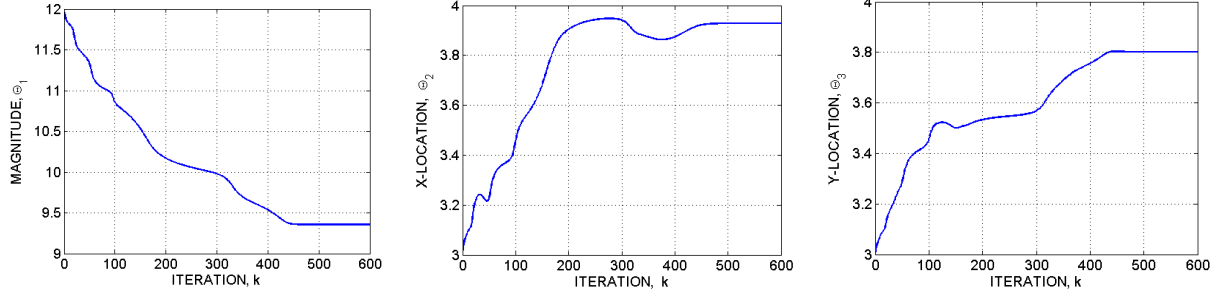


Figure 47. Estimated magnitude (left), x-coordinate of the location parameter (middle) and y-coordinate of the location parameter (right) displayed as functions of the number of iterations, k.

The convergence and the convergence rate of EM algorithm depended on its initialization. The main benefit of this work is in its potential *applications*. The estimate of a field could be a basis for a variety of inference problems such as detection, classification, tracking and object recognition.

#### 4.1.3 Facial Encoding and Matching Methods

New face encoding and matching methods operating in near real time were developed and tested. Frontal face images were first detected by using a combination of Haar wavelets and AdaBoost method, then aligned and rescaled by using software detecting eye location and affine transformation. The detected face images were Gabor filtered and then encoded using multi-scale Weber operators. The encoded images were subsequently matched against a gallery database by involving a symmetric I-divergence measure. Both the scale parameter of the operators and their number are tuned to guarantee near real time classification of subjects. The operators were applied to encode and match images for both single spectrum and cross-spectral (color vs. up to 1650 nm) comparisons. It could also deal with multiple scales (different image resolutions).

New results on the topic of cross spectral face localization and recognition were obtained.

- Three filter banks: Gabor, Median, and Curvelet were used as initial encoding step to encode visible and Short Wave Infrared face images. The secondary operators included Weber, Local Binary Patterns (LBP) and Generalized LBP. All results were fused at the matching score level. The results indicated that (1) without adaptive score normalization (previously developed by our team) fusion of the three methods outperform each of the individual filter banks; (2)

- with involvement of the adaptive score normalization, the Gabor filter bank outperformed any combination of the three filter banks.
- An eye localization algorithm applied to visible and SWIR data was developed. The detection rate (both eyes were detected) was 70%.

A set of dimensionality reduction methods was designed to further boost performance of the face recognition method.

Performance of a previously developed iterative method for distributed estimation of a Gaussian shaped physical field was evaluated. Both analog and digital cases were considered. The performance of the estimator was displayed as a function of the number of quantization levels and the number of sensors in the distributed network. The communication links were assumed to be parallel Gaussian with known statistics of the noise.

#### 4.1.4 Multivariate Adaptive Regression Spline Approach

The problem of composite function (field) estimation in distributed networks was formulated as the problem of evaluating the number and locations of the objects generating the field. This problem was known as estimation of the model order. In this case it was entirely solved by using Multivariate Adaptive Regression Spline (MARS) approach. MARS approximated the unknown smooth function in a 2D space as a linear combination of hockey-stick functions. It assumed a large number of basis functions supporting the problem of the field estimation at first and then pruned uninformative basis functions by using a generalized cross-validation method. The results of performance evaluation were available for the case of the function approximation problem (no noise is present).

#### 4.1.5 Fields Generated by Chemical Substances

The ability of a sparse distributed network of chemical sensors to estimate parameters of a field generated by a chemical substance was further analyzed. The work relied on few assumptions and models. Sensor responses were modeled as samples of an unknown deterministic concentration field generated by a chemical substance placed within the reach of the network. Sensor measurements were quantized to save energy and bandwidth during transmission of the individual measurements to the fusion center. Transmission channels were modeled as parallel Gaussian channels. The fusion center estimated the location and the peak value of the unknown field from sparse noisy distributed measurements. The solution was due to Expectation Maximization algorithm. The performance of the estimator was analyzed as a function of the network SNR, number of sensor nodes and the number of quantization levels.

#### 4.1.6 Stochastic Reduction Algorithm

A stochastic dimensionality reduction algorithm to improve performance of a previously designed algorithm for cross matching visible light and SWIR face images was developed. The stochastic model assumed that the light bounced back from a patch on an object was (cumulatively, by the law of large numbers) complex Gaussian distributed random variable. Pixel intensity, therefore, was the energy of the light reflected from a specific patch on an

object. A processed SWIR image was compared against a processed visible light image and selected segments in both images that were similar in terms of the empirical relative entropy.

The application of new models required design of new optimal processing algorithms. New optimal algorithms estimated unknown parametric fields from distributed noisy sensory data were developed.

- a. For a field modeled as a Gaussian bell function (a field due to chemical processes), an expectation-maximization algorithm was formulated and implemented to solve for unknown parameters. The sensitivity of the algorithm to a number of parameters, such as signal-to-noise ratios, the number of quantization levels, the density of sensors in the network and initial values used by the algorithm to estimate unknown parameters, was analyzed.
- b. For a field modeled as an instance of a Poisson counting process (a field due to a radioactive object), a compound algorithm was developed that combined the best features of a bi-section method and of a secant method. Sensitivity of the algorithm to the network parameters was analyzed.
- c. For a magnetic field with the magnitude decaying inversely proportional to the third power of distance from the location of the field (a field due to a ferromagnetic object), a non-linear regression analysis was applied to estimate locations of multiple objects. The dependence of the variance of estimated parameters on the number of quantization levels and on the level of noise at the estimator end was evaluated.

#### 4.1.7 Maximum Likelihood Solution

The convergence of the maximum likelihood (EM) solution to solve the problem of distributed target localization was analyzed. This solution was previously proposed by the team and applied to estimate Gaussian shaped field from noisy quantized sensory. In the best simulations, the iterative algorithm was assigned different initial values for unknown parameters. The results of this experiment can be displayed as a function of the MSE vs. the radius of the ring within which the initial values are drawn. The two panels in Figure 48 below show: (left) the distribution of initial values as a function of the ring radius and (right) the box plot of square error as a function of the radius for the case of 20 sensors and  $\text{SNR}_0=\text{SNR}_c=15$  dB. In this example, the object is placed at the location (4,4).

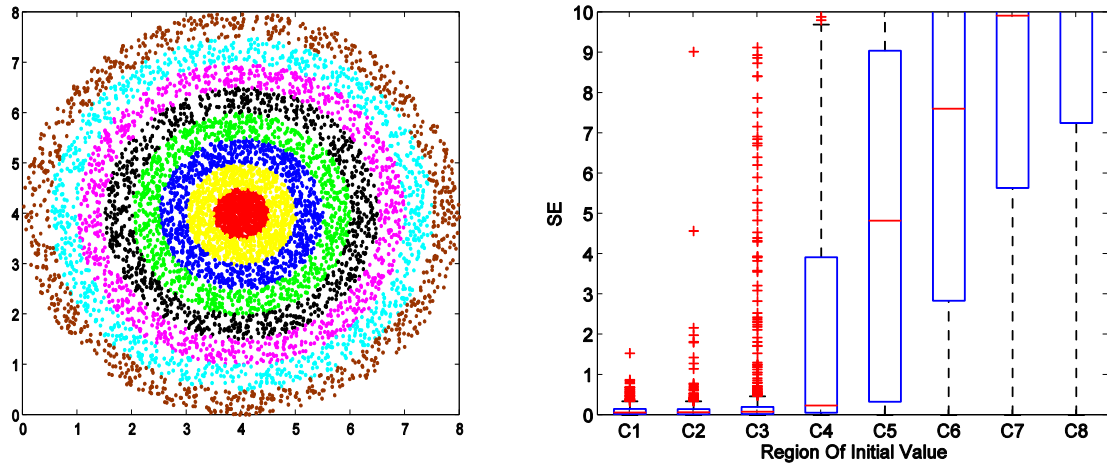


Figure 48. Distribution of initial values as a function of the ring radius the box plot of Square Error as a function of the radius for the case of 20 sensors and  $\text{SNRo}=\text{SNRc}=15$  dB.

## 4.2 Subtask 3.2 Middleware services for tracking and recognition applications using wireless sensor networks

### 4.2.1 Collaborative Multi-view Face Acquisition

In order to support such real-time face recognition systems, a camera network based data acquisition system was designed and implemented that collaboratively acquired multi-view face images of a human subject. A *choke-point* scenario was specifically considered where a network of cameras was deployed over small critical access regions such as entrances, lobbies, walkways etc. in public places for human identification. The service used the geometry of the multi-camera network and inter-camera communication to collaboratively acquire both frontal and non-frontal face images in real-time while maintaining a high sampling rate. Using this, an image could be processed for detecting non-frontal faces at almost the same rate as for frontal faces. At the same time, by narrowing down the potential regions in an image for non-frontal face detection, we significantly improved the reliability of non-frontal face detection. Our system was easy to setup, did not require camera calibration and only depended on fundamental matrices of transformation between camera pairs.

Figure 49 shows the use of camera network geometry for side face detection: When a frontal face was detected on any camera, a notification was broadcasted to other cameras specifying the center of the detected face. Epipolar geometry was used to project this point to a corresponding epipolar line (shown as AB) in the other cameras. The other cameras applied a pose-specific side-face detector in a small region surrounding the segment of the epipolar line that intersects with the background subtracted image.



Figure 49. Epipolar camera comparison. Line AB indicates epipolar line in the other cameras.

The face acquisition system was implemented on a 1.6 GHz Intel Atom Processor based embedded camera network and showed that it can reliably acquire frontal faces at 11 fps and non-frontal faces at \$10\$ fps on images captured at a resolution of 640 x 480 pixels.

#### 4.2.2 Co-design Framework for Distributed Tracking Using Sensor Networks

Designing control and tracking applications using a sensor network was a challenging task because the target track information needed to be acquired and communicated over multiple hops on an unreliable wireless medium prone to collision and fading effects. Therefore, information could be error-prone, could have unpredictable delays or even be lost. To address this challenge, a co-design approach was adopted in which the application strategy for tracking was designed hand-in-hand with the network protocols resulting in guaranteed system performance. Such a co-design was needed because a tension existed between the application requirements and what the network can supply.

#### 4.2.3 The Pursuit Application

An eventual pursuit application was considered as an example. The objective of the pursuit control system was for the pursuer object to *catch* one or more evader objects in the system. This system can be seen in Figure 50. The pursuer object was guided towards the evader using information provided by a multi-hop wireless sensor network. In this application, if the pursuer agents gained perfect information about the entire network instantaneously, designing the control strategy became simple. However, imposing such a requirement on the wireless network resulted in a lot of contention and therefore ended up decreasing the overall system performance. Therefore, the application needed to identify weaker network requirements that still resulted in provable convergence properties. These conditions imposed a specification for the network layer in terms of network abstractions and these abstractions had to be implemented using appropriate middleware services.

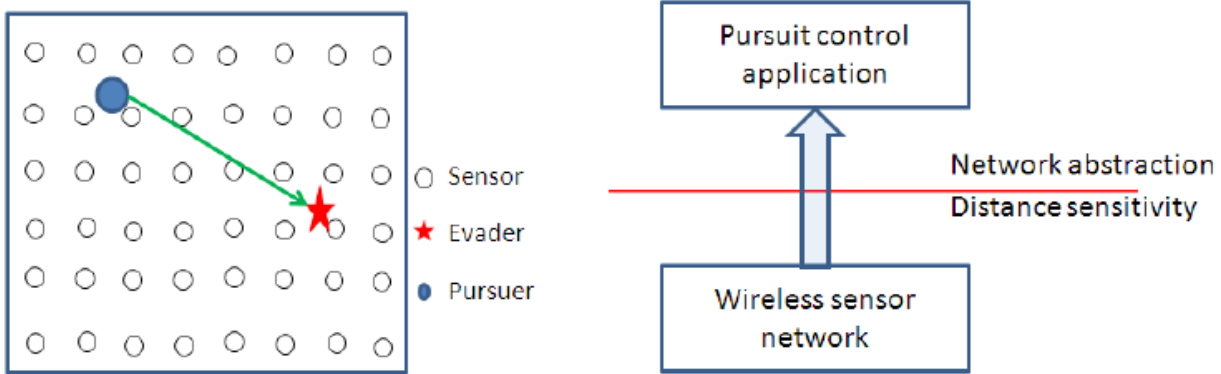


Figure 50. Exploiting distance-sensitivity for pursuer-evader tracking.

Regarding the pursuit control application, we showed that *eventual catch* was satisfied if the error in the estimate of distance to the evader decreased linearly with distance between pursuer and the evader, if the rate at which this information was supplied to the evader decreased linearly with distance and if the staleness in the information supplied decreased linearly with distance, where the constants of proportionality depended on the relative speeds of the pursuer and the evader. These conditions were represented by a network abstraction, namely *distance sensitivity*. In order to implement these abstractions, we designed a middleware service that periodically delivers information while meeting the required *distance sensitivity* properties.

#### 4.2.4 Exploitation of Distance Sensitivity

A decomposition technique for solving coupled convex optimization problems over a wireless network using local message exchange was developed. To do so, *distance sensitivity* properties inherent in many spatially distributed control systems were exploited, i.e., the influence of an actuator on sensors decays with distance and likewise a controller tends to be less impacted by sensors that are farther away. The distance sensitivity in actuator influence was modeled using an influence matrix whose coefficients decayed away from the diagonal at different rates. Distance decaying property was used to decouple the optimization problem in such a way that individual actuators decided their control inputs based on information exchange within a bounded locality that depended on the nature of the influence matrix. In contrast, existing techniques used a network wide exchange of messages to achieve convergence, which imposed high control latency.

#### 4.2.5 Exploiting Distance-sensitivity for Spatially Distributed Control Systems

For many spatially distributed control systems the influence of an actuator on sensors decayed as a non-decreasing function of distance and likewise an actuator tended to be less impacted by sensors that were farther away. This property was exploited to identify conditions under which local feedback was sufficient for satisfying a global objective. This was useful for control systems that operate over wireless networks because communication can be restricted to local areas only. The idea was based upon an observation that the inverse of a diagonally decaying matrix (with exponential decay) can be approximated by a tri-diagonal matrix – which in turn pointed to local feedback being sufficient for maintaining optimality in control.

#### 4.2.6 VCAST Traffic Information Services

VCAST, an algorithm for obtaining individual vehicle location as well as aggregate traffic information over an infrastructure-less multi-hop wireless vehicular network was designed. VCAST can be used to improve safety against collisions, inform about approaching emergency vehicles and lane merging vehicles (that may even be beyond a single hop communication range) and to enable dynamic routing and navigation techniques by providing aggregate traffic information in an extended neighborhood. To ensure scalability in forwarding information over multiple hops, we exploited a notion of *distance sensitivity in information propagation*, by which traffic information is propagated at a rate that decreased linearly with distance from the source. By doing so, traffic information was obtained with a staleness, which is a measure of error in the traffic information, that was bounded by  $O(d^2)$  where  $d$  is the communication hop distance from the source of the information. At the same time, the required communication rate per unit time at each node only depended on the radius of the region in terms of communication hops, and not on the vehicular density or the number of vehicles in the region. VCAST did not require any special hardware or modification to vehicular transmission standards; instead it could simply piggyback on basic *Here I am* communication for vehicular networks. The results were presented at the IEEE Vehicular Technology Conference 2012. Figure 51 depicts VCAST's range and accuracy when used to disseminate traffic information.

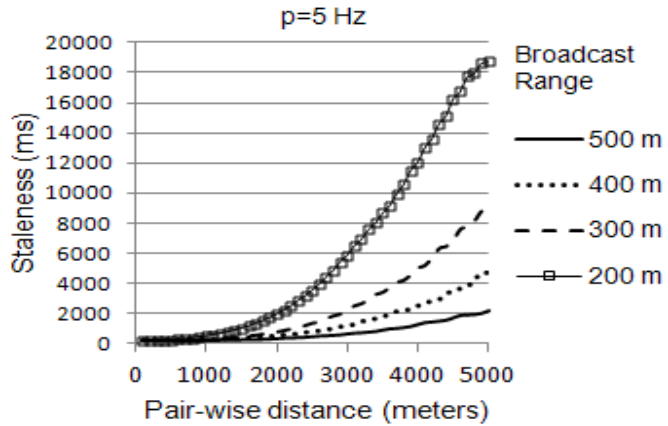


Figure 51. The figure shows the impact of the communication range on information staleness at different inter-vehicular distances when VCAST is used to disseminate traffic information. The source broadcast rate is 5Hz.

The results which were submitted to IEEE Vehicular Technology Conference 2012 dealt with:

1. Simulations were carried out in ns-3 using an IEEE 802.11p (DSRC) transmission model to quantify the impact of channel fading, vehicular density, vehicular mobility and time-varying inter-vehicular separations on the achievable staleness.
2. The average communication cost incurred by each vehicle was quantified.
3. An analytical comparison of the communication cost with schemes that do not incorporate distance-sensitivity was provided.
4. Complete proofs were developed for all Lemmas and Theorems. The extended results were submitted to the international Journal of Vehicular Technology.

A basic vehicular mobility simulator was developed that allows the team to test reactive vehicular systems based on information obtained from VCAST. Note that the concept of

VCAST can even be applied in military settings to provide distance-sensitive location tracking of personnel and targets. Efforts were also directed at extending the protocol along these lines.

#### 4.2.7 Simultaneous Coverage and Tracking:

A network of PTZ cameras used for monitoring a large region was considered and a local algorithm was described that could track targets at a high resolution while maximizing the coverage resolution at all non-target points. The algorithm was local, converged quickly to a final state and could remain stable in a configuration for longer periods in the presence of a mobile target. The performance of the algorithm was evaluated in simulations, the impact of network density was analyzed, and the size of the area over which the reconfiguration was performed on the achievable coverage resolution. It was observed that by progressively increasing the size of the locality over which the reconfiguration was performed, the improvement in coverage resolution started decreasing significantly, thus highlighting the merits of a localized approach. As a result, targets could be tracked at a high resolution, the entire space could be observed at an acceptable resolution, and the observing cameras could be kept stable for long periods of time by only performing the reconfiguration in a local area around the target.

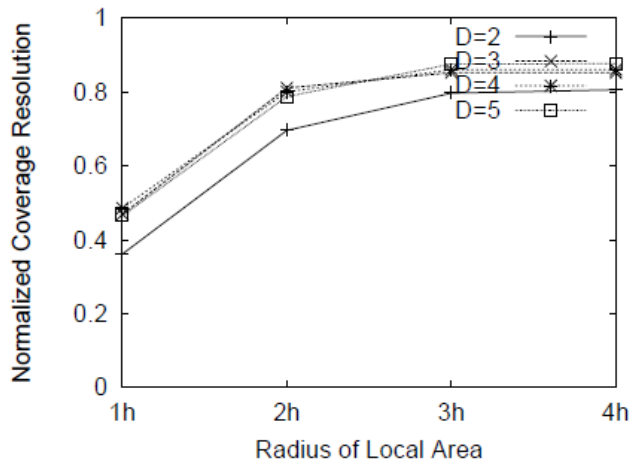


Figure 52. Impact of the locality of reconfiguration on the normalized coverage resolution of a monitored area.

Figure 52 depicts the impact of the locality of reconfiguration on the normalized coverage resolution of an area that is being monitored. As the locality increased, impact on coverage resolution progressively started to decrease, highlighting merits of a localized approach.

#### 4.2.8 Face Recognition

The use of a wireless camera network was demonstrated to perform near real-time face recognition that yields high accuracy and robustness. A portable camera network was assembled using off-the-shelf components in which individual cameras perform background subtraction and face detection, and transmit only relevant face images to a fusion center for recognition. The technique relies on opportunistically acquiring suitable face images as a subject walks through the multi-camera network. By only transferring the face images and further filtering them based on suitability for recognition, it was possible significantly reduce the required network bandwidth. An efficient face recognition algorithm was also designed

using multi-scale Weber operators. The performance of this system was evaluated for face recognition using a dataset of 29 subjects collected using the portable camera network. The networked face recognition system is able to achieve comparable recognition performance to the commercial L1 FaceIt software while reducing the required processing time.

*Trident Systems* demonstrated their UWB system for acquiring video images in real-time, in an outdoor environment. During this demonstration, a few videos were collected with human subjects walking through the area at different distances from the camera. The objective was to test if the images would successfully work with the multi-view face detection system. Figure 53 depicts an individual being photographed from Trident systems. We tested those images for front face detection system and the performance was satisfactory at distances of approximately up to 10-13 feet. A sample detected face image is shown below. The face detection system was developed on a portable Linux platform of about 600 MHz and thus potentially the system could be integrated with the Trident UWB system.

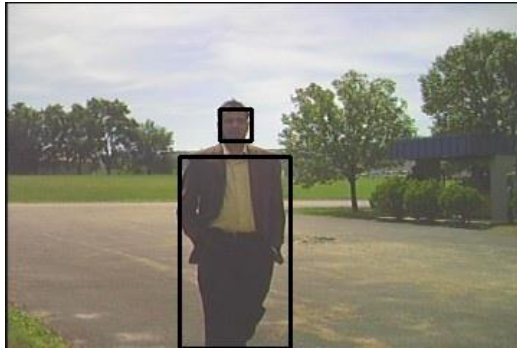


Figure 53. A sample image collected from Trident systems test are. The figure shows the face image and human body silhouette detected by our system on a portable Linux platform.

#### 4.2.9 Control Serializability

It was identified that ensuring consistency and serializability in the presence of concurrent executions was a fundamental problem in a distributed sensor actuator network based control system. The camera coverage control system described above was a specific instance of such a system. It was shown using a prototype implementation on a network of Telos motes that this was expected to significantly decrease the amount of contention and the latency of each control action. It was also shown that there are several design parameters that impose an inherent tradeoff between the likelihood of inconsistency and achievable control latency. The result was to use these parameters to implement a service that can be tuned for optimal performance (in terms of control latency) based on deployment density and communication range.

#### 4.2.10 Fusion Techniques for Networked Biometric Systems

Recent terror attacks, security threats and intrusion attempts have necessitated a transition to modern biometric systems that can identify humans in real-time under unconstrained environments. Specifically, the following were three critical transitions that were needed and which formed the focus of the research:

1. In contrast to operation in an offline mode using previously acquired photographs and videos obtained under controlled environments, it was required that identification be performed in a real-time dynamic mode using images that were continuously streamed in, each from a potentially different view (front, profile, partial profile) and with different quality (pose and resolution).
2. While different multi-modal fusion techniques were developed to improve system accuracy, these techniques mainly focused on combining the face biometrics with modalities such as iris and fingerprints that were more reliable but require user cooperation for acquisition. In contrast, the challenge in a real-time networked biometric system was that of combining opportunistically captured multi-view facial images along with soft biometric traits such as height, gait, attire and color that did not require user cooperation.
3. Typical operation was expected to be in an open-set mode where the number of subjects that enrolled in the system was much smaller than the number of probe subjects; yet the system was required to generate high accuracy.

To address these challenges and to make a successful transition to real-time human identification systems, following contributions were made:

1. A score-based multi-modal, multi-sample fusion technique was designed to combine face images acquired by a multi-camera network and the effectiveness of opportunistically acquired multi-view face images using a camera network in improving the identification performance is characterized;
2. The multi-view face acquisition system was complemented by a network of Microsoft Kinects for extracting human anthropometric features (specifically height, shoulder width and arm length). The score-fusion technique was augmented to utilize human anthropometric data and the effectiveness of this data was characterized.
3. The performance of the system was demonstrated using a database of 51 subjects collected using the networked biometric data acquisition system.

The results showed improved recognition accuracy when face information from multiple views was utilized for recognition and also indicated that a given level of accuracy could be attained with fewer probe images (less time) when compared with a uni-modal biometric system. Furthermore, it was observed that when the required false acceptance rate was very low (<1%), human anthropometric data plays a critical role.

#### **4.2.11 Demonstration of Real-time Face Recognition at DHS Center of Excellence Meeting**

The previously designed collaborative multi-view face acquisition system was integrated with PittPatt face recognition software, and the combined system was used to perform real-time face recognition in an unconstrained setting. The combined prototype system was demonstrated at the DHS center of excellence performance review meeting held at Phoenix, AZ on August 15, 2011. Only the front face images were used for recognition. The system was tested with a suspect database of 3 subjects and showed high accuracy (<5% False positives and almost 0% False rejection rate).

#### 4.2.12 EzTrack: Indoor Positioning

Radio frequency (RF) based techniques, being low cost and not requiring line of sight, were ideally suited for indoor tracking of humans and objects in various enterprises such as hospitals, office spaces, assisted living centers and child care centers. However, RF based tracking was also challenging because radio signals are prone to time-varying multipath interference in indoor environments. To counter this challenge, most existing techniques for RF based indoor tracking relied on building a RF signature model of the indoor environment using offline calibration, which can be a time consuming and expensive process and still cannot be exhaustive. Requirements of prior site survey and calibration severely limited the portability of RF-based solutions and have inhibited the widespread deployments of RF-based indoor tracking systems. Here, *EzTrack* was presented; an adaptive and self-configuring RF-based tracking system, which utilized wireless sensor networks, which eliminated the need for prior calibration. EzTrack was able to achieve 75<sup>th</sup> percentile accuracies of about 4.5-7.5 feet (1.5-2.5m) in indoor environments. The performance of EzTrack was validated using experiments in different indoor environments with networks of IEEE 802.15.4 based TelosB motes. Figure 54 depicts error tracking.

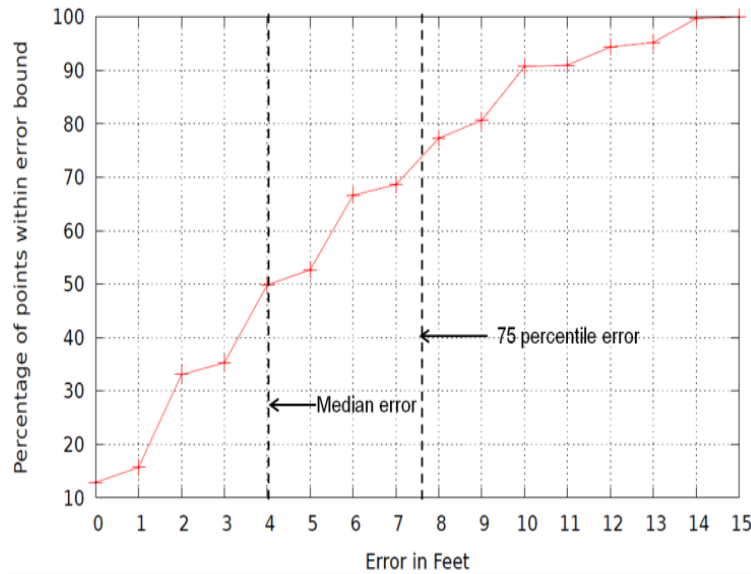


Figure 54. Tracking error in EzTrack - anchor nodes at 14 feet separation.

### 4.3 Subtask 3.3 Decentralized Control Algorithm for Self-Healing/Self Forming Network of Mobile Agents

A mobile wireless sensor network (MWSN) consists of  $n$  mobile sensors (or agents), which are connected through wireless communication links along which information flows. These sensors act cooperatively to provide distributed, real-time information from the physical world. Mobile robots or vehicles are exploited so that the sensors can dynamically reposition themselves to maximize the collective information gained by the network. A wide spectrum of applications of this structure of MWSN have been reported in the articles which include target tracking, formation and coverage control, environmental monitoring and several others. For these cooperative sensing applications, it was desirable to maintain a connected communication graph, even as communication links were established or lost as the agents moved. For this reason, consensus algorithms were used to maintain the connectivity of the

graph. Moreover, communications within the WSNs suffered from unpredictable delay, loss, and energy constraints. These constraints also included actuators and energy (battery, fuel) limitations, which produced forces, which led to agent movements. So the controller which was applied to maintain the connectivity graph should technically consider these constraints and uncertainties too.

#### 4.3.1 Distributed Model Predictive Control

Many control laws were proposed for controlling a network of dynamic agents with different models and communication topologies. Most of them did not exploit optimal control ideas and did not account for input constraints, which in many cases had to be included in the problem formulation due to actuator limitations and energy efficiency concerns. Distributed model predictive control (DPMC) algorithms for consensus problems of mobile agents considering delay and uncertainty resulting from wireless communication networks along with minimization and equalization of energy consumption of each agent in presence of practical constraints on actuators was proposed.

In multi-agent MPC, each MPC was associated with a different node and computed the local control inputs based only on the states of the node and of its neighbors. In this way, actions which an agent takes were influenced by both the evolution of the agent itself and the evolution of the neighbor agents connected to it through communication links. Since the agents in a multi-agent control structure usually have no global overview and can only access a relatively small number of sensors and actuators, predicting the evolution of a sub network over a horizon involved even more uncertainty than when a single agent was employed. The control structure for this system can be seen below in Figure 55.

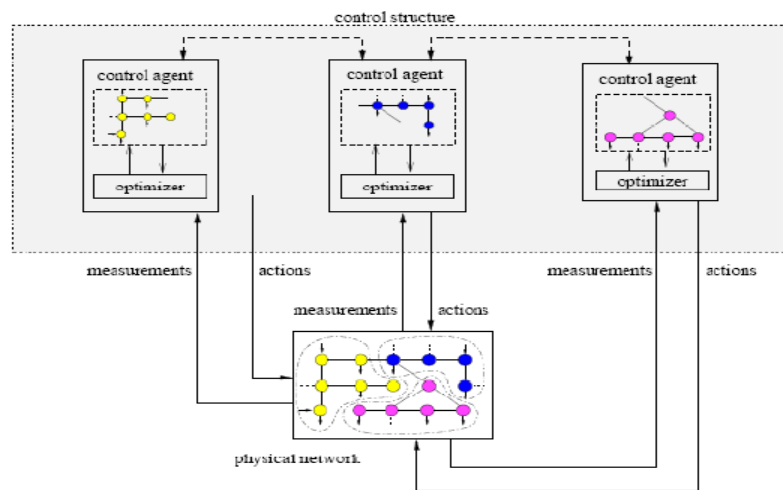


Figure 55. Distributed multi agent Model Predictive Control Structure.

The multi-agent model predictive control scheme was defined to achieve the fire tracking mission where each robot needed to know its current states, its neighbors' current states and models and constraints of its neighbors. Based on such information, each robot computed its optimal inputs and its neighbors' optimal inputs assuming a constant set of neighbors over the horizon. The input to the neighbors was only used to predict their trajectories and then discarded, while the first component of the optimal input of problem

was implemented on each robot. The solution of each sub-problem yielded a control policy for each robot. The objective was defined as:

1. Tracking control and area coverage- the main goal of cooperative robot agents was to scan an area to collect data. For this reason, they should have track a pre-specified path which was calculated by path planning algorithms. The algorithm worked based on the data gathered from sensors and the planned path was defined so that maximum data was gathered from the environment.
2. Energy minimization- energy minimization was met by minimizing the work that was the amount of consumed energy by each agent during prediction horizon.
3. Equal velocity and graph connectivity- mobile agents should have the same velocity so that the overall flocking has monolithic movement leading to mobile agents did not deviate and become isolated from the connected graph.
4. Collision Avoidance- collision avoidance between robots during maneuvers was defined as a cubic protection zone for each of the robots so that these zones did not interfere during maneuvers as seen in Figure 56. Infinite norm was used to describe the collision avoidance constraint since it can be converted to Mixed Integer Linear Programming (MILP) form for which several algorithms exist, as opposed to Euclidian norm (2-norm) that led to nonlinear non-convex optimization problems which were difficult to solve.

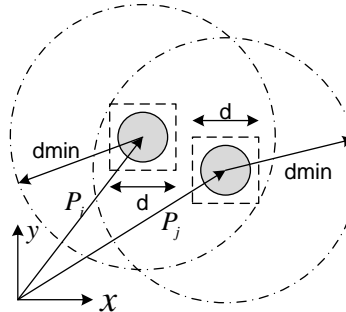


Figure 56. Protection zone of the robots and their position.

A fire monitoring mission using MWSN utilizing thermal or visual sensors to detect the fire was considered as the simulation scenario. Location of the fire was determined by flocking of the mobile robots in an area. On the detection of fire by agents, the fire-detection message containing the relative direction of the fire location was communicated through wireless links to the neighboring agents. Assuming that MWSN formed a connected-graph, the message was received by all mobile agents and hence the direction of flocking of the robots changed to move to the fire location. Figure 57 (left) a shows the evolution of position of two mobile agents in time with corresponding control signal. As seen from the left portion of Figure 56, the two mobile agents maneuvered to meet the collision avoidance while fulfilling the mission. It noted from the snapshots of the maneuver in x-y plane in Figure 56 (right) that the two robots did not collide into each other during their maneuvering.

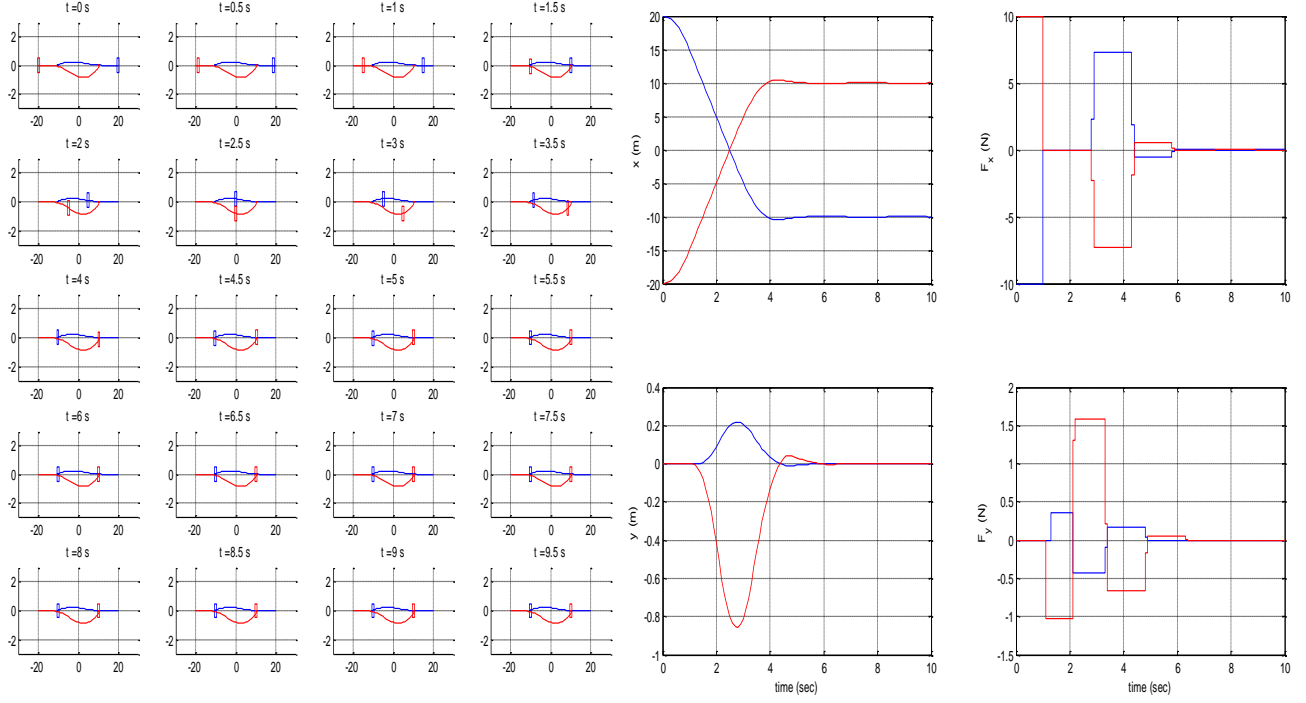


Figure 57. Left, evolution of the robots position in xy plane over a period of time with collision avoidance. Right, collision avoidance between two mobile robots; robot 1 (blue) and robot 2 (red).

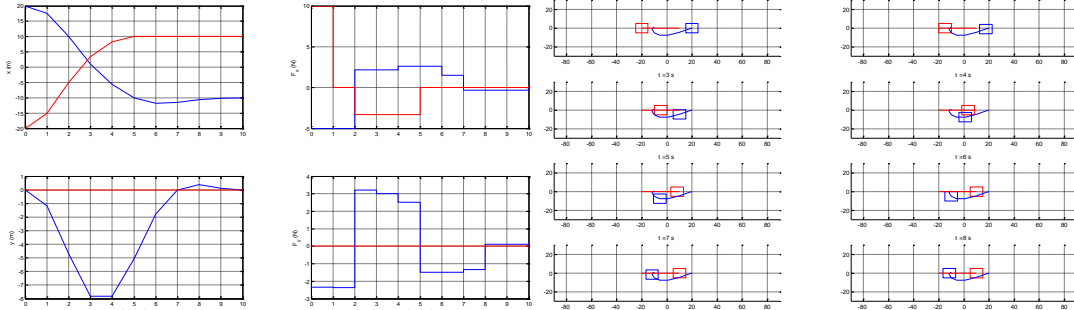


Figure 58. Uncertainty condition in one time stamp: Left, evolution of the robots position in xy plane over a period of time with collision avoidance. Right, collision avoidance between two mobile robots; robot 1 (blue) and robot 2 (red).

Figure 58 depicts the uncertainty condition of the robots in a onetime stamp scenario. The left portion of this figure shows how the robots positioned themselves in the XY plane over a period of time without coming into contact with one another. The right portion of Figure 58 highlights the areas of collision avoidance between the two robots. Alternatively, Figure 59 depicts the uncertainty condition of the robot in a multiple time stamp scenario.

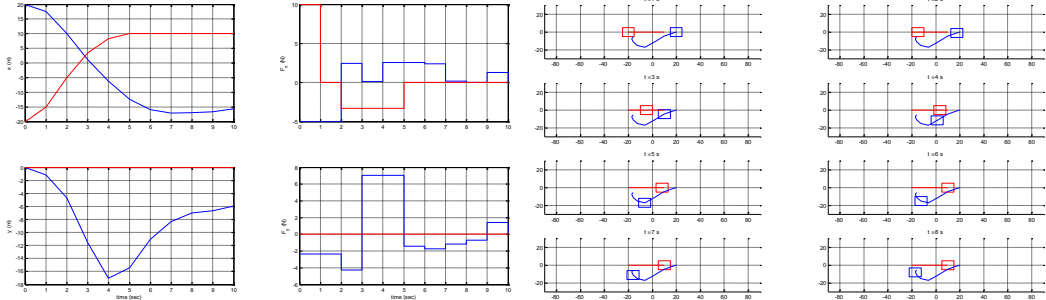


Figure 59. Uncertainty condition in multiple time stamp: a) Left, evolution of the robots position in xy plane over a peridod of time with collision avoidance. Right, collision avoidance between two mobile robots; robot 1 (blue) and robot 2 (red).

#### 4.3.2 Autonomous Robots

Autonomous robots are robots that can perform desired tasks in unstructured environments without continuous human guidance. In recent times, autonomous robots have been used everywhere, but their main usage is for military purposes like information gathering, mapping, and even as weapons. Information gathering is a task done by robots and autonomous vehicles to build up a map within an unknown environment, or to update a map within a known environment, while at the same time keeping track of their current location. This is important in military applications as important data can be collected without risking human lives. Our research focused on the formulation of a strategy for the trajectory planning problems for autonomous robots in the information tasks where the positions of information points are uncertain. This automatically led to model predictive control strategy, which used the updated knowledge about the model to solve a finite horizon optimal control problem at each time step and only executed the first control strategy. Then this strategy was applied to an autonomous robot, collecting information within a finite region with randomly changing information points and their main objective function was to collect the maximum information in the minimum amount of time.

#### 4.3.3 Decentralized Model Prediction Control

Multi-Parametric toolbox was explored to realize the Decentralized Model Prediction Control (DMPC). Multi-Parametric toolbox was developed by the Swiss Federal Institute of Technology and allowed for the derivation of real-time controller parameters. Tractable state feedback controller was obtained with different schemes of infinite time optimal control, finite time optimal control, minimum time control and low complexity controller. Finite time optimal control was modeled and implemented for tracking control.

The global model for tracking control was decentralized to obtain a decomposition model of two mobile agents. These agents, aside from interacting with the external environment, interacted with one another based on predictive control for the tracking mission. Note that the decentralized models began to overlap as they shared common states and inputs. The optimal input vector was calculated from the predictive horizons for future time instants and for each agent only the first component was actually applied. The different simulation outcomes were investigated for two control actions, which were:

1. fast and slow trajectory information sharing, and
2. fast trajectory information sharing.

Fast and slow trajectory information sharing allowed predictive control for slow mobile agents with future time instant information from fast mobile agents. The performance index increased as slow mobile agent trajectories were controlled utilizing future and current information. Figure 60 shows the proposed control where the red indicated faster predictive information gathering and blue indicated control based on local and predictive information.

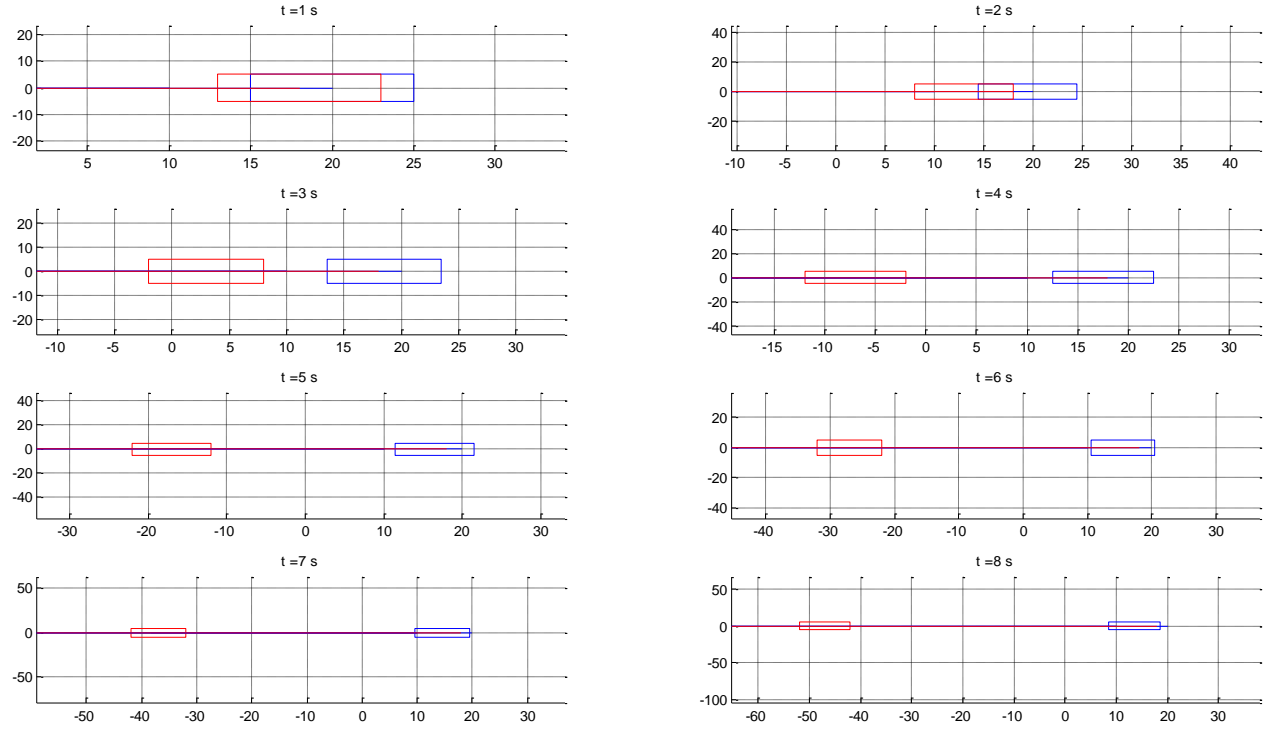


Figure 60. Demonstration of Faster and Slower Movement; robot 1 (blue) and robot 2 (red).

DMPC was based on iterative, finite horizon optimization of a plant model. At time,  $t$ , the current mobile agent was sampled and a cost minimizing control strategy was computed (via a numerical minimization algorithm) for a relatively short time horizon in the future:  $[t, t+T]$ .

In DMPC, only the first step of the control strategy was implemented, then the plant state was sampled again and the calculations were repeated starting from the new state, yielding a new control and new predicted state path. The prediction horizon shifted forward and for this reason DMPC was also called *receding horizon control*.

Distributed Model Predictive Control can best summarized as a multivariable control algorithm that uses:

- an internal dynamic model of the process
- a history of past control moves and
- an optimization cost function  $J$  over the receding prediction horizon

And, DMPC's optimum control moves possessed:

- DMPC methods to reduce the complexity of the mathematical model.
- DMPC methods could be easily implemented for real time applications.
- DMPC allowed the agents to make decisions onboard without the involvement of the operator.

#### 4.3.4 Summation of the Functioning of MPC on Any Plant/System

MPC is an established control technique because of its prominent advantages in solving problems with physical constraints as well as multivariable problems in nature. Subject to a set of constraints, the objective of MPC is to minimize an appropriate cost function in an online fashion by determining the optimal input sequence over the control horizon. The cost function usually consists of two components: (i) one is the tracking error between the predicted process output and the reference trajectory (also known as set points) over the prediction horizon; (ii) the other component is the incremental control moves over the control horizon.

#### 4.3.5 Extended Kalman Filtering SLAM using MPC with Dynamic Features

Here, the case considered was when the information gathering task was formulated by estimating a state vector containing features of interest in the environment. The estimation was performed by Extended Kalman Filter (EKF). It was showed that the planning problem in this scenario could be regarded as an optimal control problem for a nonlinear system with a gradually identified model. Then, the MPC strategy was proposed, which was suitable for online decision making, changing models and dynamic constraints. Two scenarios, SLAM with single robot and with two robots were used as case studies.

In order to implement the Kalman Filter in the SLAM process, it was necessary to describe the system. Therefore, it was assumed that the robot moved in a linear fashion, and that the system could be described by the following equations:

*Equation 3*

$$x_{k+1} = F_k x_k + G_k u_k + v_k$$

*Equation 4*

$$y_k = H_k x_k + w_k$$

Equation 3 was the state equation and indicated the robot state at the next time step is a linear function of the current state,  $x_k$ , the input vector,  $u_k$ , and an error term,  $v_k$ . Equation 4 was the output equation and indicated that the measurement vector taken from the sensors was a linear function of the robot state,  $x_k$ , and an error term,  $w_k$  [17, 18].

The constraints of the robot's motion were to be incorporated into the planning process. The control constraints and state constraints can be expressed by

*Equation 5*

$$u_k \in U_k, \quad x(t) \in X_{(k+1)}, \quad \forall t \in [k, k+1],$$

where  $U_k$  is the set of admissible controls for robot at time  $k$  and  $X_{(k+1)}$  describes the safe region for robot during time  $k$  to time  $k+1$ .

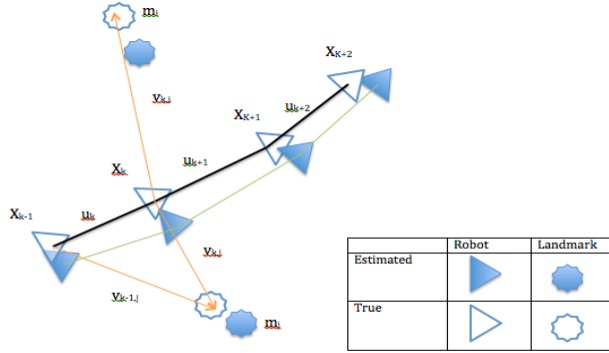


Figure. The essential SLAM problem. A simultaneous estimate of both robot and landmark location is required.

Figure 61 below is the simulation results for the SLAM using Kalman Filter for a single robot, the first figure on left shows the trajectory followed by a robot having limited sensor range and the second figure on right shows the trajectory followed by a single robot having wide sensor range.

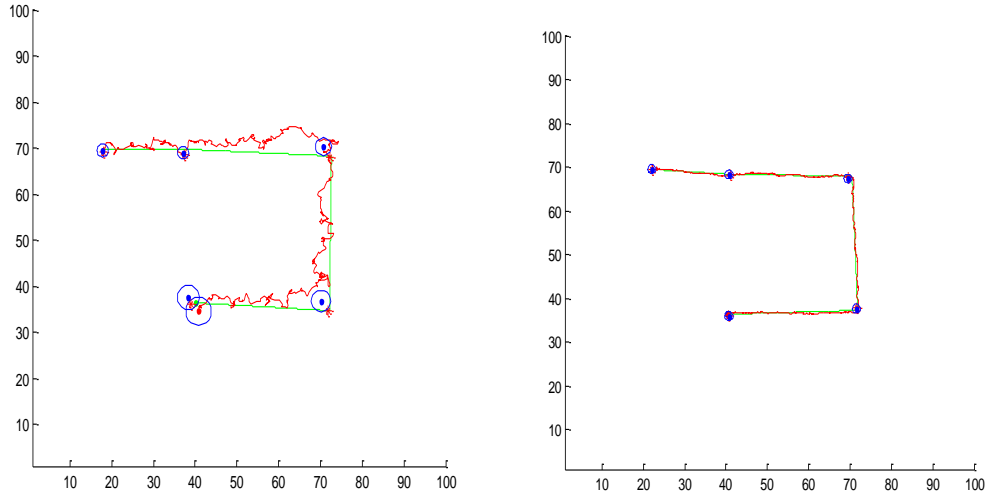


Figure 61. SLAM with EKF and without MPC (left) and b) SLAM with EKF and MPC (right)

#### 4.3.6 Kalman Filter Derivation

The robot was never aware of its state with absolute certainty due to measurement and process errors. Therefore, the robot state was tracked as the mean of a normal distribution. Now, since the robot state was a vector containing multiple variables, the mean of the joint distribution of these variables had to be tracked [19].

The Kalman Filter worked by predicting the robot state at the next time step based on known information, and then corrected this prediction at the following time step based upon measured data at that time. Therefore, we had to find an equation for the prediction of the robot state.

The robot state was predicted by plugging the current robot state into the state equation. We

also know that the process noise has mean 0, so we predicted  $v_k$  to be 0 and found:

$$\hat{x}_{k+1} = F_k \hat{x}_k + G_k u_k$$

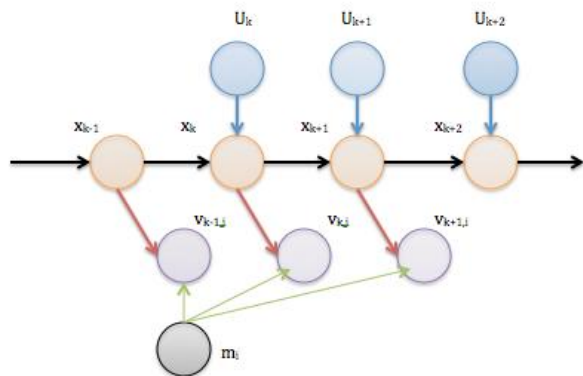


Figure 62. Graphical model of EKF SLAM algorithm.

Figure 62. Graphical model of EKF SLAM algorithm.

Note here that the hat on  $x$  denoted that it was an estimate rather than the actual state, and that the subscript denoted that it was an estimate of the state at time step  $k + 1$ . It should also be noted that we used superscript  $-$  (e.g.  $\hat{x}^-_k$ ) to denote that the estimate was performed with information up to time  $k - 1$ . This made both the notation  $\hat{x}^-_k$  and  $\hat{x}_{k+1}$  predictions since they were estimates of a certain time step with information up to the previous time step.

#### 4.3.7 Research Issues on Mobile Wireless Sensor Networks

Two main research issues were *communication issues* and *data management issues*. Communication issues included topology control, coverage, target tracking as well as localization. Data management issues were data gathering and data replication [18]. Topology control was the problem of assigning transmission powers to every node in order to maintain connectivity while minimizing the energy consumption of the whole network.

- One of the basic and significant factors in the design and application of MWSNs was sensor coverage measured by the overall area that a WSN currently monitored. Sensor coverage was closely related to the quality of service that the network could provide, and it decreased due to undesirable sensor deployment and sensor failures. There were two ways to maintain sensor coverage in these cases: self-deployment and relocation.
- Self-deployment meant that mobile sensors should have the ability to autonomously adjust their positions to improve the coverage after their initial deployment.
- Sensor relocation refers to deploying a moderate number of redundant sensors and strategically relocating them as needed to fill the position of failed nodes.
- Target tracking was the need for sensors to be aware of the position of nodes in order to make sense of data and perform further navigational tasks. Because of mobility which increased the uncertainty of nodes, localization in MWSNs was more difficult.

#### 4.3.8 Data Replication Issue

In MWSNs, due to the free moving of sensors and harsh environments, disconnection occurred frequently which resulted in network divisions. In such situations, sensors in one of the divided network could not access data in other divided networks. One to solve the network division problem for improving data accessibility was to replicate data items from other sensors.

#### 4.3.9 Model Predictive Control of a SISO

The main objective was to hold a single *output*,  $y(\bar{y})$ , at a *reference value* (or *set-point*),  $r$ , by adjusting a single *manipulated variable* (or *actuator*)  $u$ . The SISO plant actually had multiple inputs, as shown in the following figure. In addition to the manipulated variable input,  $u$ , there was a possible measured disturbance,  $v$ , and an unmeasured disturbance,  $d$ . Model Predictive Control Toolbox design always provided *feedback* compensation for unmeasured disturbances and *feed-forward* compensation for any measured disturbance. Model Predictive Control required a *model* of the impact that  $v$  and  $u$  have on. It used this *plant model* to calculate the  $u$  adjustments needed to keep  $y(\bar{y})$  at its set-point. This calculation considered the effect of any known constraints on the adjustments (typically an actuator upper or lower bound, or a constraint on how rapidly  $u$  can vary). One may also specify bounds on  $y(\bar{y})$ . These constraint specifications were a distinguishing feature of Model Predictive Control.

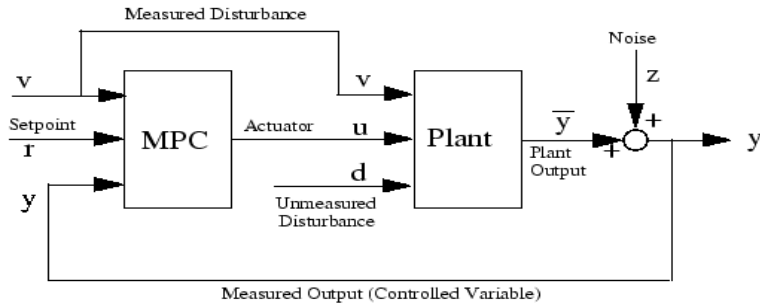


Figure 63. Simple SISO system model with plant and MPC control.

Typical Sampling Instant-Model Predictive Control Toolbox design generated a *discrete-time* controller—one that acquired action at regularly spaced, discrete time instants. The *sampling instants* were the times at which the controller acted. The interval separating successive sampling instants was the *sampling period*,  $\Delta t$  (also called the *control interval*).

Figure 64 shows the state of a SISO model predictive control system. This system operated for many sampling instants. Integer  $k$  represented the current instant. The latest measured output,  $y_k$ , and previous measurements,  $y_{k-1}, y_{k-2}, \dots$ , are known and are the filled circles in the figure. Figure 64 also shows the controller's previous moves,  $u_{k-41}, \dots, u_{k-1}$ , as filled circles. To calculate its next move,  $u_k$  the controller operated in two phases:

- *Estimation.* In order to make an intelligent move, the controller needed to know the current state. To accomplish this, the controller used all past and current measurements and the models.
- *Optimization.* Values of set-points, measured disturbances, and constraints were specified over a finite *horizon* of future sampling instants,  $k+1, k+2, \dots, k+P$ , where  $P$  (a finite integer  $\geq 1$ ) is the *prediction*. The controller computes  $M$  moves  $u_k, u_{k+1}, \dots$

...  $uk+M-1$ , where  $M$  ( $\geq 1, \leq P$ ) is the *control horizon*. In the above example shown in the figure,  $P = 9$  and  $M = 4$ . The moves are the solution of a *constrained* optimization problem.

When it finished calculating, the controller sent move  $u_k$  to the plant. The plant operated with this *constant* input until the next sampling instant,  $\Delta t$  time units later. The controller then obtained new measurements and *calculates new control input*. This cycle repeats indefinitely.

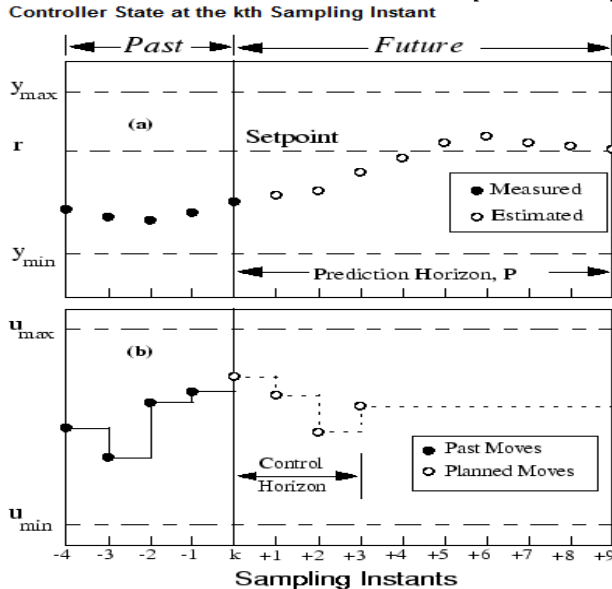


Figure 64. Illustration of MPC.

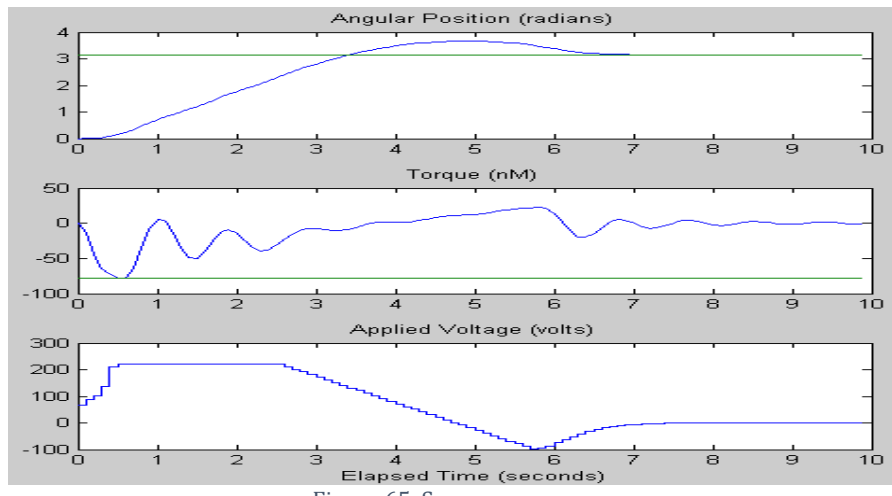


Figure 65. Servo responses.

The servo response shown in Figure 65 settles within 5 seconds with no overshoot. It also displays the torque's lower bound, which became active after about 0.9 seconds but wasn't exceeded. The applied voltage saturates between about 0.5 and 2.8 seconds, but the controller performs well despite this.

#### 4.3.10 Multi-rate Fast Output Feedback Sampling Controller

In a discrete time system with input  $u_k$ , states  $x_k$  and output  $y_k$  at time  $t = k\tau$ .

$$x_{k+1} = \Phi_\tau x_k + \Gamma_\tau u_k$$

$$y_{k+1} = C_0 x_k + D_0 u_k, \quad (1)$$

where

$$C_0 = \begin{pmatrix} C \\ C\Phi \\ \vdots \\ \vdots \\ C\Phi^{N-1} \end{pmatrix}, \quad D_0 = \begin{pmatrix} 0 \\ C\Gamma \\ \vdots \\ \vdots \\ C \sum_{r=0}^{N-1} \Phi^r \Gamma \end{pmatrix}$$

Assuming that a state feedback gain  $F$  has been designed such that  $(\Phi_\tau + \Gamma_\tau F)$  has no eigenvalues at the origin. For this state feedback, one can define the fictitious measurement matrix  $C(F, N) = (C_0 + D_0 F) (\Phi_\tau + \Gamma_\tau F)^{-1}$ , which satisfies the fictitious measurement equation  $y_k = C x_k$  then the static output feedback for the system (1) will be  $u_k = L y_k$ . For  $L$  to realize the effect of  $F$ , it must satisfy

$$x_{k+1} = (\Phi_\tau + \Gamma_\tau F) x_k = (\Phi_\tau + \Gamma_\tau L C) x_k \text{ i.e. } L C = F.$$

Let ' $\gamma$ ' denote the observability index of  $(\Phi, \Gamma)$ . It can be shown that for  $N \geq \gamma$ , generically  $C$  has full column rank, so that any state feedback gain can be realized by a fast output sampling gain  $L$ .

In particular, there are many systems in which faster output sampling periods cannot be taken, even though the input actuating period can be taken at relatively high speeds. Generally in such systems, feedback controllers are designed according to a single rate based on the measured output at slow sampling rate. In these cases, the control performance within the slow sampling period was not always ensured. However, if the input can be updated at a faster rate, one can expect an improvement in the control performance. With this in mind, multi-rate control approaches with a lifting technique in which the control input can be updated at fast rate have widely researched. By using the lifting technique, one can design a controller with the fast-rate updating rate.

## 5 Task 4: Design and demonstrate massively parallel simulation of large-scale sensor networks

### 5.1 Ad-hoc Network

In consultation with ARL fellow Dr. Don Torrieri, a very general system model was developed for the frequency-hopping ad-hoc network. The channel was designed to undergo Nakagami or Rayleigh fading. The effects of adjacent channel interference (due to the spectral splatter effect) were taken into account. The modulation and coding were taken into account by using the concept of *modulation-constrained capacity*, which predicted the performance of a capacity-approaching code combined with an actual modulation. Given a fixed network geometry and set of shadowing coefficients, the outage probability was found in closed form for Rayleigh fading, and more generally, Nakagami fading.

An example is shown in Figure 65. The network consists of 10 interferers located on a disk of radius 30 and a source transmitter at unit distance from a receiver at the center of the disk (distance is normalized so that one “unit” of distance corresponds to the source-receiver distance). The particular network geometry was realized by independently drawing each node's location from a uniform distribution. Once the network was drawn, it was fixed for the remainder of the analysis. The network geometry for this example was shown in the inset of the figure. In the example, the path loss coefficient was equal to 3 and the number hopping frequencies was equal to 1000. An *outage* was declared whenever the instantaneous signal-to-interference and noise ratio (SINR) dropped below the threshold  $\beta$ . The *outage probability* was denoted by the variable  $\varepsilon$ . The figure showed the outage probability in unshadowed Rayleigh fading for three values of SINR threshold  $\beta$  as a function of the SNR  $\Gamma$ . For each value of  $\beta$ , an analytical curve is shown, which was determined by using the exact expression derived during this phase of the research. Also shown is a curve generated by simulation, which involved randomly generating the exponentially-distributed power gains associated with the channel between each transmitter and the receiver. As can be seen in Figure 66, the analytical and simulation results coincide, which was expected because the analysis was exact. Any discrepancy between the curves is attributed to the finite number of Monte Carlo trials (one million trials were executed per SNR point).

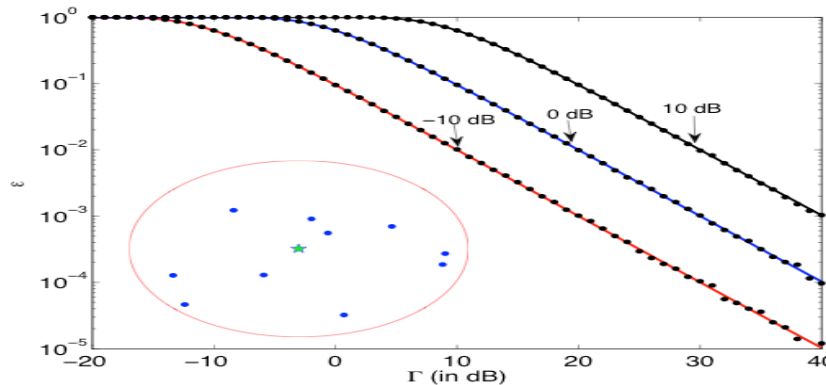


Figure 66. Outage probability  $\varepsilon$  as a function of SNR for SINR thresholds  $\beta = \{-10, 0, 10\}$  dB. Analytical curves are solid, while dots represent simulated values. The network geometry is shown in the inset.

Figure 66, above, depicts outage probability  $\epsilon$  as a function of SNR for SINR thresholds  $\beta = \{-10, 0, 10\}$  dB. Analytical curves are solid, while dots represent simulated values. The network geometry is shown in the inset. The star at the center of the radius-30 circle represents the receiver, while the ten interferers are shown as dots. The desired transmitter is not shown, but lies at unit distance away from the receiver.

A similar analysis was developed for the more general case of Nakagami fading and log-normal shadowing. The general outage probability was a function of the particular network geometry and set of shadowing coefficients. In addition, the average outage probability was derived for unshadowed Rayleigh fading when the nodes are distributed according to an independent and uniform spatial distribution.

The approach for modeling and analyzing ad hoc networks that were discussed above have been generalized to account for a variety of channel models, physical-layer waveforms, and MAC-layer protocols. The basic approach was to place a reference receiver at the center of the network, and then compute the *probability of outage* at that receiver, where an *outage* was defined to be the event that the signal-to-interference and noise ratio (SINR) falls below a threshold value. The threshold value was determined from information theory and represented that *capacity* of the underlying modulation format. The analytical challenge was to derive closed-form expressions for the cumulative distribution function (CDF) of a random variable which represented the difference between the received signal power and the total interference power. By rigorously applying classical probability theory, a closed form expression was derived which could determine the outage probability conditioned on a particular network topology.

### 5.1.1 Guard Zones

The analytical approach enabled the influence of system-wide parameter settings to be investigated. Performance was computed for a variety of code rates, modulation parameters, spread-spectrum settings, and MAC protocols. Particular emphasis was placed on determining the impact of the *guard zone* on system performance. A guard zone is a circular area placed around a transceiver over which no interferers may transmit. Guard zones were implemented in practice by using collision avoidance protocols such as carrier-sense multiple access with collision avoidance (CSMA/CA). Figure 67 shows an ad hoc network with guard zones. The reference receiver is represented by a star, while transmitters are represented by circles. The desired transmitter is red, while interferers are blue. Because the nodes represented by green circles are inside the guard zones of the blue interferers or red transmitter, they are not allowed to transmit and therefore do not produce interference (note that in the absence of a guard zone, the green nodes would transmit and create interference).

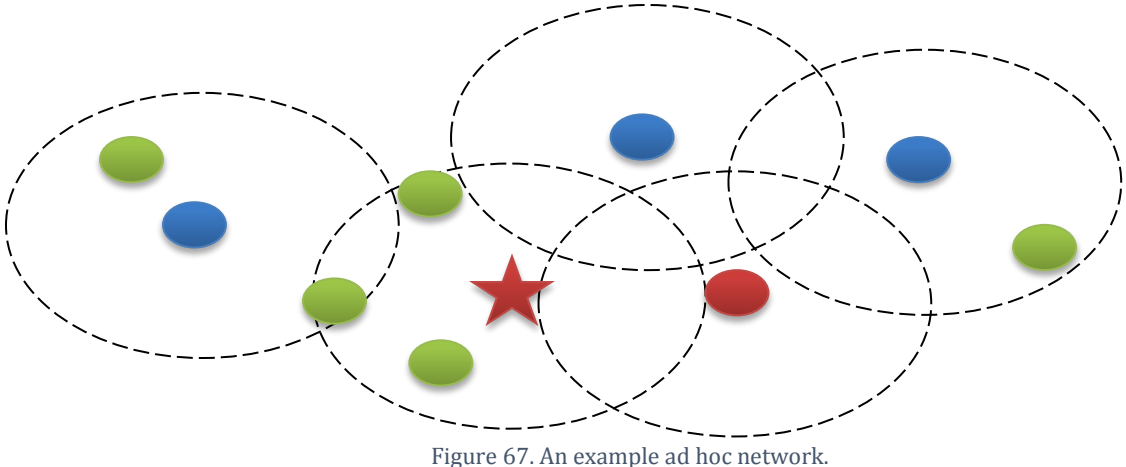


Figure 67. An example ad hoc network.

An example ad hoc network is shown in Figure 67. The reference receiver is the red star, and the corresponding reference transmitter is the red circle to its right. Blue circles represent interferers. Each transmitter has a circular guard zone surrounding it. Green circles are nodes whose transmissions are suppressed due to being in a guard zone.

A natural question we asked when using guard zones was “what was the optimal guard zone radius?” Answer, “there was a tradeoff.” If the guard zone radius was too small, then there were nearby interferers that degraded performance, yet if the guard zone was too large then not very many nodes were permitted to transmit, reducing the total amount of data supported by the network. Using our analytical approach, the optimal guard zone radius could be found.

### 5.1.2 The Analytical Approach

First, a network topology was drawn at random according to a representative spatial model. The outage probability was determined for the drawn network. Initially, no guard zones were used, and the corresponding outage was found. Then nodes were deactivated one at a time by imposing guard zones of increasingly larger radii. The corresponding outage of the thinned network was computed, and the number of nodes and guard zone radius were noted.

Outage alone was not a good measure of performance. This was due to the fact that outage was minimized by using a guard zone of infinite radius, which suppresses all interferers. However, an infinite guard zone was not efficient because only a single transmission was supported by the network at a time, which was a poor use of spectrum. Instead of using outage, the transmission capacity as a measure of performance was used. The transmission capacity was the throughput of the single reference link multiplied by the *density* of the network, measured in the number of nodes per unit area. Transmission capacity was interpreted as the *area spectral efficiency* of the network and takes on units of bits-per-second per Hertz per square-meter, or  $\text{bps}/\text{Hz}/\text{m}^2$ .

Figure 68 shows the outage probability and transmission capacity of a representative sampling of networks. Both metrics are shown as a function of the guard zone radius  $r_{\min}$  and

the number of active nodes  $M$ . From the figure, it can be seen that setting  $r_{\min} = 1.2$  maximizes the transmission capacity, and resulted in a network with 22 active nodes.

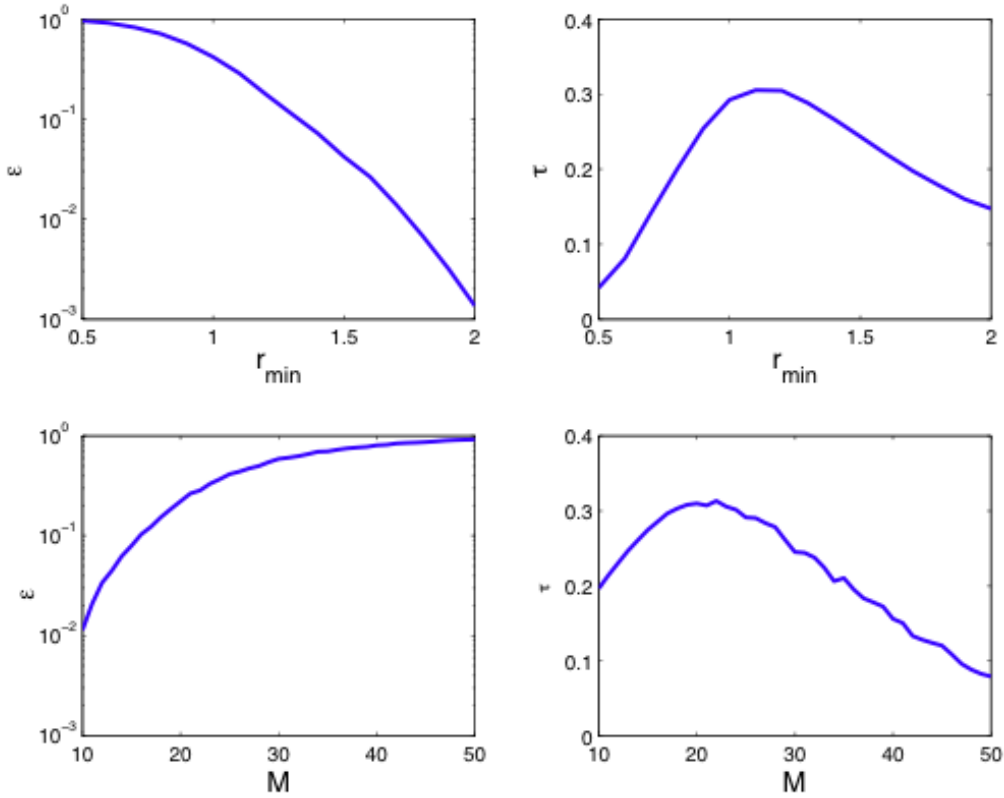


Figure 68. Influence of guard zone radius  $r_{\min}$  on network performance.

Influence of guard zone radius  $r_{\min}$  on network performance. The network initially has  $M=100$  interferers and is contained in a circular region of radius 4. A guard zone of radius  $r_{\min}$  is imposed. The value of  $r_{\min}$  is gradually increased, and the corresponding number of active nodes  $M$  is noted, along with the outage probability  $\epsilon$  and transmission capacity  $\tau$ . From these curves, the optimal value of  $r_{\min} = 1.2$ , for which  $M=22$  nodes are active.

### 5.1.3 Guard Zones in Sensor Networks

Interference is a major limiting factor in any ad hoc or sensor network, and the goal of medium-access control protocols (MACs) was to control interference. New methodology was applied for analyzing ad hoc networks to study critical aspects of interference-avoidance protocols. This work was done jointly with ARL fellow Dr. Don Torrieri, and was submitted to *Infocom-2012*.

In this example provided by Figure 69, a reference receiver was located at the center of the network and a transmitter was placed one unit away (to the Thirty (30) interfering transmitters are placed in the arena surrounding the reference receiver. These interferers were placed at random, but in such a way that they were never too close together. The minimum distance between interferers was called an *exclusion zone*, and is meant to model the natural spacing that occurs when wireless networks were deployed.

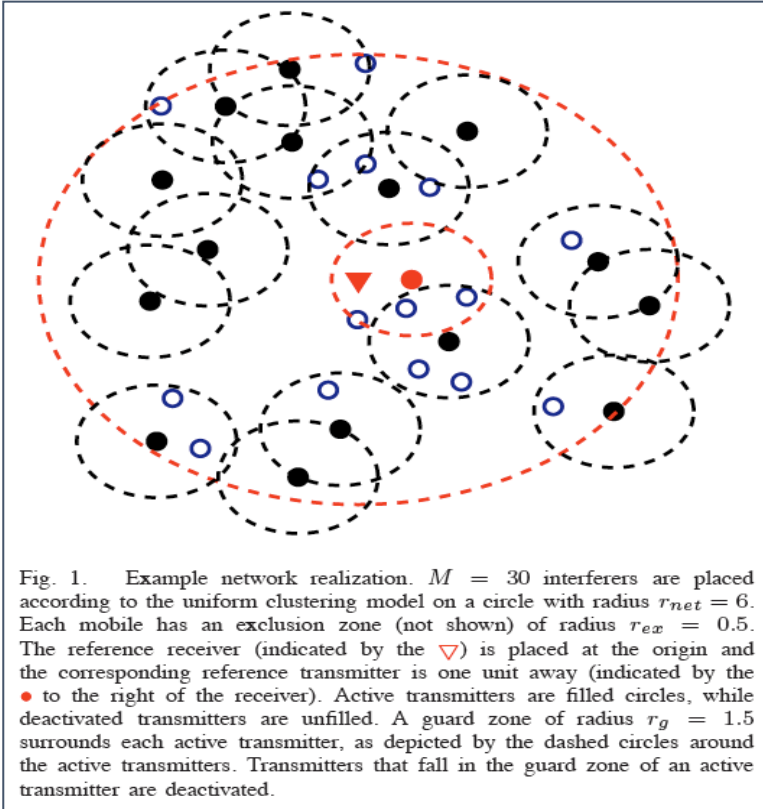


Figure 69. Example of network realization.

#### 5.1.4 CSMA Guard Zone

In addition to the exclusion zone, another zone can be seen in the figure called a *CSMA guard zone*. The CSMA guard zone was a circular area surrounding active transmitters. Any other transmitter inside an active transmitter's CDMA guard zone was not permitted to transmit. In the figure, there are 15 active interfering transmitters (represented by filled black circles) and 15 transmitters whose transmissions are suppressed because they are in the CSMA guard zone of an active transmitter. Figure 69 represented a snapshot in time. During a different time slot, a different set of nodes may have become active, while others may have become suppressed that are in the new active transmitters' guard zones.

In considering such a network, the radii of the two guard zones was critical. For instance, if the CSMA guard zone was too large then too many transmissions will be suppressed, but if the guard zone was too large, the interference level may be too high. Using the previously developed analytical approach and our cluster-computing resources, we determined optimal guard zone radii under a wide range of channel and network conditions. The optimization was performed with respect to the *transmission capacity*, which is the area spectral efficiency in units of bits per second per Hertz per square-meter (bps/Hz/m<sup>2</sup>).

### 5.1.5 Improvement of Cyberinfrastructure

A significant effort was directed towards testing and improving the high-performance cyber infrastructure in place to support the optimization and simulation jobs required to enable the team's research progress. Previously, the cyberinfrastructure was configured to execute specific functions related to network optimization, a refactoring of the software now allows the computing infrastructure to be able to handle a much wider range of computing tasks. As a case study to demonstrate the flexibility of the infrastructure, the computing cluster was configured to support the semester course project in the Spring semester 2012 Coding Theory course (EE 567). Students would upload the LDPC-code parity-check matrix that they designed to a web app, and the code would be simulated in parallel on the cluster. Jobs completed in about 15 minutes, in contrast to the 7-8 hours required to run locally. CML Matlab Toolbox was utilized. CML is a Matlab toolbox designed by the Wireless Communications Research Laboratory (WCRL) for supporting various link-level simulations. Initially, the program could only be run on a single computer, but WVU now fully runs it parallel on the cluster.

Capabilities for running parallel Monte Carlo simulations and numerically-intensive analytical jobs on the cluster computer were also improved. Focus was on efficient scheduling algorithms. The approach to scheduling is documented in the thesis of Aruna Bommagani, a M.S. student funded by this project who successfully defended. The previous capability to run parallel Monte Carlo simulations on a cluster computer was also generalized, so that they could now run on a very general class of scientific computing applications written in Matlab on our cluster.

## 6 Conclusion

Four tasks were addressed in the course of the Advanced Communication for Wireless Sensor Networks projects supported by the Army Research Laboratory. These tasks included:

- Task 1: Design, test and demonstrate cooperative and multi-antenna communications systems.
- Task 2: Design, test, and demonstrate low-power analog and compressive sensing subsystems.
- Task 3: Design, test and demonstrate real-time fault-tolerant protocols for data aggregation, inference, location tracking, and connectivity maintenance in a mobile heterogeneous sensor network.
- Task 4: Design and demonstrate massively parallel simulation of large-scale sensor networks.

To address Task 1, two subtasks were undertaken, rapid prototyping of MIMO systems and investigation of cooperative communication systems. Task 2 was addressed with the assistance of three subtasks, nano-derived micro sensors for remote threat detection, reliable and energy efficient sensing using analog signal processing, and low-power collective sensing. Research focused on task 3 was comprised of three subtasks, distributed coding and data exchange in heterogeneous sensor networks, distributed target tracking and connectivity maintenance in a mobile network, decentralized control algorithm for self healing/self forming network of mobile agents. Finally, task 4 did not have any defined subtasks, however focus was placed on ad hoc networks, guard zones, and the improvement of cyber infrastructure.

## 7 References

- [1] Y. Wong, S. Chen, S. Mau, C. Sanderson and B. Lovell, "Patch-based Probabilistic Image Quality Assessment for Face Selection and Improved Video-based Face Recognition," in *IEEE Biometrics Workshop, Computer Vision and Pattern Recognition (CVPR) Workshops*, 2011.
- [2] S. Krishna, "Open CV Viola-Jones Face Detection in Matlab," [Online]. Available: <http://www.mathworks.com/matlabcentral/fileexchange/19912-open-cv-viola-jones-face-detection-in-matlab>. [Accessed 27 June 2016].
- [3] Mathworks, Inc, "Matlab Software," Natick, 2016.
- [4] A. Sheikh and V. Mathe, "Dielectric, ferroelectric, magnetic and magnetoelectric properties of PMN-PT based ME composites," *Journal of Physics and Chemistry of Solids*, vol. 72, pp. 1423-1429, 2011.
- [5] Y. Hu, W. Pearlman and X. Li, "Progressive Significance Map and Its Application to Error Resilient Image Transmission," *IEEE Trans. on Image Processing*, vol. 21, no. 7, pp. 3229-3238, 2012.
- [6] X. Li, "Collective sensing: a fixed-point approach in the metric space," in *SPIE Conference on VCIP*, 2010.
- [7] X. Li, "Image Recovery via Hybrid Sparse Representations: a Deterministic Annealing Approach," *IEEE Journal of Selected Topics in Signal Processing, special issue on adaptive sparse representations*, vol. 5, no. 5, pp. 953-962, 2011.
- [8] W. Dong, G. Shi and X. Li, "Image Denoising via Low-Rank Approximation Simultaneous Sparse Coding," in *CVPR*, 2012.
- [9] W. Dong, G. Shi and X. Li, "Nonlocal Sparsity Regularized Image Restoration: A Low-Rank Approach," *IEEE Transactions on Image Processing*, 2012.
- [10] G. Freedman and R. Fattal, "Image and Video Upscaling from Local Self-Examples," *ACM Trans. Graph.*, vol. 12, pp. 30-32, 2011.
- [11] D. Varodayan, D. Chen and B. Girod, "Network Image Coding for Multicast," in *IEEE 10th Workshop on Multimedia Signal Processing*, 2008.
- [12] W. Dong, L. Zhang, G. Shi and X. Li, "Doubly Centralized Sparse Representation for Image Restoration," *IEEE Transactions on Image Processing*, 2012.
- [13] K. Nguyen, T. Nguyen and S. Cheung, "Peer-to-Peer Streaming with Hierarchical Network Coding," in *IEEE International Conference on Multimedia and Expo*, 2007.
- [14] W. Dong, G. Shi and X. Li, "Image Reconstruction with Locally Adaptive Sparsity and Nonlocal Robust Regularization," *Signal Processing: Image Communication*, 2012.
- [15] J. Xiao, A. Ribeiro, Z. Luo and G. Giannakis, "Distributed Compression-Estimation using Wireless Sensor Networks," *IEEE Signal Processing Magazine*, pp. 27-41, July 2006.
- [16] M. Gaspar, M. Vetterli and P. Dragotti, "Sensing Reality and Communicating Bits: a Dangerous Liaison," *IEEE Signal Processing Magazine*, pp. 70-83, July 2006.
- [17] M. Gamini Dissanayake, P. Newman, S. Clark, H. Durran-Whyte and M. Csorba, "A solution to the Simultaneous Localization and Map Building (SLAM) Problem," *IEEE Transactions on Robotics and Automation*, vol. 17, no. 3, pp. 229-241, 2001.

- [18] H. Durrant-Whyte and T. Bailey, "Simultaneous Localization and Mapping: Part I," *IEEE Robotics & Automation Magazine*, pp. 99-108, June 2006.
- [19] A. Norton and A. McCook, "Implementation of a Simultaneous Localization and Mapping Algorithm in an Autonomous Robot," Trinity College, Hartford, 2012.